Theses and Dissertations--Electrical and Computer Engineering

Electrical and Computer Engineering

2024

Gas assisted electron beam patterning processes

Deepak Kumar

University of Kentucky, 89krdeepak@gmail.com

Author ORCID Identifier:

https://orcid.org/0000-0001-9801-8820

Digital Object Identifier: https://doi.org/10.13023/etd.2024.66

Right click to open a feedback form in a new tab to let us know how this document benefits you.

Recommended Citation

STUDENT AGREEMENT:

I represent that my thesis or dissertation and abstract are my original work. Proper attribution has been given to all outside sources. I understand that I am solely responsible for obtaining any needed copyright permissions. I have obtained needed written permission statement(s) from the owner(s) of each third-party copyrighted matter to be included in my work, allowing electronic distribution (if such use is not permitted by the fair use doctrine) which will be submitted to UKnowledge as Additional File.

I hereby grant to The University of Kentucky and its agents the irrevocable, non-exclusive, and royalty-free license to archive and make accessible my work in whole or in part in all forms of media, now or hereafter known. I agree that the document mentioned above may be made available immediately for worldwide access unless an embargo applies.

I retain all other ownership rights to the copyright of my work. I also retain the right to use in future works (such as articles or books) all or part of my work. I understand that I am free to register the copyright to my work.

REVIEW, APPROVAL AND ACCEPTANCE

The document mentioned above has been reviewed and accepted by the student's advisor, on behalf of the advisory committee, and by the Director of Graduate Studies (DGS), on behalf of the program; we verify that this is the final, approved version of the student's thesis including all changes required by the advisory committee. The undersigned agree to abide by the statements above.

<div align="right">

Deepak Kumar, Student

Todd Hastings, Major Professor

Daniel Lau, Director of Graduate Studies

</div>

University of Kentucky

UKnowledge

2024

Gas assisted electron beam patterning processes

Deepak Kumar

STUDENT AGREEMENT:

I represent that my thesis or dissertation and abstract are my original work. Proper attribution has been given to all outside sources. I understand that I am solely responsible for obtaining any needed copyright permissions. I have obtained needed written permission statement(s) from the owner(s) of each third-party copyrighted matter to be included in my work, allowing electronic distribution (if such use is not permitted by the fair use doctrine) which will be submitted to UKnowledge as Additional File.

I hereby grant to The University of Kentucky and its agents the irrevocable, non-exclusive, and royalty-free license to archive and make accessible my work in whole or in part in all forms of media, now or hereafter known. I agree that the document mentioned above may be made available immediately for worldwide access unless an embargo applies.

I retain all other ownership rights to the copyright of my work. I also retain the right to use in future works (such as articles or books) all or part of my work. I understand that I am free to register the copyright to my work.

REVIEW, APPROVAL AND ACCEPTANCE

The document mentioned above has been reviewed and accepted by the student's advisor, on behalf of the advisory committee, and by the Director of Graduate Studies (DGS), on behalf of the program; we verify that this is the final, approved version of the student's thesis including all changes required by the advisory committee. The undersigned agree to abide by the statements above.

Deepak Kumar, Student

Todd Hastings, Major Professor

Daniel Lau, Director of Graduate Studies

Gas assisted electron beam patterning processes

DISSERTATION

A dissertation submitted in partial
fulfillment of the requirements for
the degree of Doctor of Philosophy
in the College of Engineering at the
University of Kentucky

By
Deepak Kumar
Lexington, Kentucky

Director: Dr. Todd Hastings,
Professor of Electrical and Computer Engineering
Lexington, Kentucky
2024

ABSTRACT OF DISSERTATION

Gas assisted electron beam patterning processes

Radiolysis is a complex phenomenon in which molecules subjected to ionizing radiation form new chemical species. Electron-beam irradiation has proven to be a versatile approach for significantly altering materials' properties and forms the basis for electron-beam lithography using both organic and inorganic resists. Electron-beam exposure is normally carried out under high vacuum conditions to reduce contamination and allow for unhindered interaction between the electrons and the resist material. Exposure under an ambient gas at sub-atmospheric pressures has been found to provide a distinct mechanism which can be exploited to circumvent some of the challenges associated with material processing and significantly alter or enhance material's properties. This dissertation discusses the modifications in standard electron beam resist characteristics during gas assisted electron beam pattering.

We studied the effect of water vapor pressure on positive and negative tone electron-beam patterning of poly methyl methacrylate (PMMA). For both positive and negative-tone patterning, it was found that increasing the water vapor pressure considerably improved the contrast of PMMA. As expected from electron scattering in a gas, the clearing dosage for positive tone patterning gradually increased with vapor pressure. Also, electron scattering in water vapor yielded a substantially larger clear region around the negative-tone patterns. This effect could be useful for increasing the range of the developed region around cross-linked PMMA far beyond the backscattered electron range. As a result, VP-EBL for PMMA offers a new means of tuning clearing/onset dose and contrast while enabling more control over the size of the cleared region around negative-tone patterns.

We provide a novel way to simultaneously tune the emission wavelength and enhance the fluorescence intensity of fluorophores formed by irradiating polystyrene with a focused electron beam under various gaseous environments. We studied the effect of electron dose and gas pressure on the emission spectra and photon yield of irradiated polystyrene film on a variety of substrates. Up to 10x enhancement in fluorescence yield was achieved using water vapor and the peak emission wavelength tuned over a wide wavelength range. Thus, localized electron-beam synthesis of fluorophores in polystyrene can be controlled by both dose and by ambient water-vapor pressure. This technique could enable innovative approaches to photonics where

fluorophores with tunable emission properties can be locally introduced by electron-beam patterning.

We also studied the effect of ambient gases on contrast and resolution of PMMA on conducting and insulating substrates. E-beam exposures were conducted under vacuum conditions and 1 mbar of water vapor, helium, nitrogen and argon to study their effect on contrast and resolution of PMMA on silicon, fused silica and soda lime glass substrates. On silicon, exposure under water vapor yielded contrast values significantly higher than vacuum exposure, consistent with our previous work. However, exposure under helium yielded slightly improved contrast compared to vacuum exposure. On insulating substrates exposure under helium environment yielded contrast values significantly higher compared to vacuum exposure. The clearing dose was found to increase with the gases' molecular weight and proton number, consistent with the increase in scattering cross-section. The improved contrast and sensitivity (dose to clear) of PMMA under helium motivated us to study the resolution under various gases. Resolution testing indicated that despite the lower clearing dose, helium still exhibited the best resolution with 25-nm half-pitch dense lines and spaces clearly resolved on soda lime glass. Thus, VP-EBL of PMMA under helium yields higher sensitivity and contrast on insulating substrates without sacrificing resolution.

KEYWORDS: Micro and nano fabrication, variable pressure e-beam lithography, large area positive-tone writing, tunable emission, enhanced fluorescence

$\overline{\hspace{2cm}\text{Deepak Kumar}\hspace{1cm}}$

$\overline{\hspace{2cm}\text{April 1, 2024}\hspace{1cm}}$

Gas assisted electron beam patterning processes

By
Deepak Kumar

<div style="text-align:right">

_____
Dr. Todd Hastings
Director of Dissertation

_____
Dr. Daniel Lau
Director of Graduate Studies

_____
April 1, 2024
Date

</div>

Dedicated to my Parents and Teachers

"anādyavidyā yuktasya puruṣhasyātma vedanam
svato na sambhavād anyas tattva-jño jñāna-do bhavet"
(Bhagavad Gita: Chapter 4, Verse 34)

ACKNOWLEDGMENTS

I sincerely express my deepest gratitude to my advisor, Dr. Jeffrey Todd Hastings, for his strong encouragement, incessant support, and invaluable guidance. His endless support and motivation have been of utmost importance during the entirety of my PhD journey. It could not have been possible for me to undertake this journey without his support.

I extend my sincerest gratitude to my esteemed committee members, Dr. Joseph Brill, Dr. Ishan Thakkar and Dr. Dan M. Ionel for their insightful suggestions and guidance. I am deeply grateful to Dr. Joseph Brill for his unwavering support, discussions and help with the infrared spectroscopy experiments that is of significant importance in this research. I also express my gratitude to Dr. Gabriel Dadi for his invaluable role as the dissertation's external examiner.

I express my sincere appreciation to my colleagues Dr. Mansoor Sultan, Dr. Sarah Lami, Patrick Montgomery, Cooper Meyers, RJ Smith and Alex Thuringer, without whose assistance and guidance this work would have been far more challenging.

I genuinely appreciate the technical support provided by the staff of the Center for Nanoscale Science and Engineering (CeNSE) and the Electron Microscopy Center (EMC) at the University of Kentucky, Brain Wajdyk, Nicolas J. Briot, Dali Qian, Jillian Cramer and Michael Detisch.

I am forever grateful to my parents for instilling in me the values of leadership, patience, and selflessness in carrying out one's responsibilities, no words can ever be enough to express the unconditional love of the parents. I also express my profound gratitude to my family and well-wishers for their unceasing support and encouragement.

TABLE OF CONTENTS

LIST OF FIGURES

LIST OF TABLES

Chapter 1 Introduction

1.1   Background

Over the past 80 years, a great deal of research has been done on studying the effects of high-energy irradiation on polymer materials. Exposure of polymer materials to high-energy radiation generally results in modification of polymer properties. Electron beam is the most widely used radiation source for polymer modification processes. Polymers undergo chain scission (degradation) or cross linking (gelation) under the influence of high energy irradiation, in the process polymer properties are modified which in turn depends on the reaction mechanism resulting from the radiation conditions used. There are numerous applications that uses electron beam to directly write patterns on polymers. Generally, a thin layer of polymer (called resist) is deposited onto a substrate and subsequently irradiated by an electron beam. Bombardment of electrons on the resist induces a wide range of interactions between the incident electrons and the resist. As the incident electrons travel through the resist it undergoes a series of elastic and inelastic scattering events in the resist and the substrate.
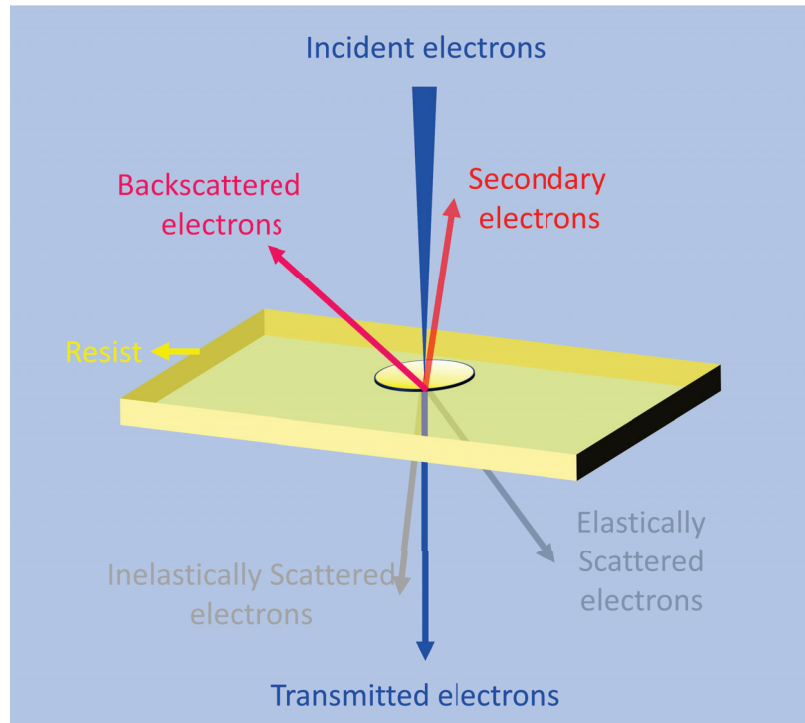
Figure 1.1: Electron resist interaction.

Figure 1.1 shows the electron-resist interaction in it's simplest form. The incident electrons undergo elastic and inelastic scattering in the resist and substrate, producing a series of secondary and backscattered electrons. In inelastic scattering,

the electrons continuously loose energy ionizing the resist and substrate producing a cascade of low voltage (<50 eV) secondary electrons, these electrons are called forward scattered electrons. These forward scattered electrons are responsible for most of modifications brought about in the resist upon radiation. In elastic scattering events, the electrons collide with the much heavier nucleus deflecting by a large angle while retaining most of it's energy, these electrons are called backscattered electrons. These backscattered electrons can further ionize the resist and substrate to produce more secondary electrons. The backscattered electrons can travel to far away points from the initial electrons' point of interaction, hence, the backscattering contribution is significantly more severe than the forward scattering contribution.

Material property modification by electrons can be classified by (i) transport processes via energy transport and charge transport, and (ii) localization processes via energy localization and charge localization. Electron trajectory in the resist and substrate, from Monte Carlo simulation using CASINO [1], at incident beam energy of (a) 2 keV and (b) 30 keV is shown in Figure 1.2. The interaction volume of the incident electrons with the resist decreases with increasing beam energy, therefore the interaction volume with the resist can be modulated by varying the beam energy of the incident electrons for the desired application. Exposure to electron radiation is usually carried out under vacuum conditions to minimize electron scattering as well as to eliminate any possibility of contamination. However, the interaction of electrons in environment other than vacuum conditions can be different in turn resulting in a different outcome than for exposure under vacuum conditions.

Electron-resist interaction under vacuum condition is much more simpler compared to the presence an ambient gas during exposure. Under vacuum conditions the interaction can be broadly classified in three categories (i) incident electrons – resist interaction, (ii) resist – signal interaction (signal here includes the secondary and backscattered electrons as well as X-rays, Auger electrons, etc. that are produced), and (iii) incident beam – signal interaction. The presence of an ambient gas makes the exposure process complicated as the number of interactions during the process increases twofold as apart from the above mentioned interactions the following also need to be taken into account: (i) incident electrons – gas interaction, (ii) signal – gas interaction, and (iii) gas – resist interaction.

The reactivity of excited polymer chains with water to produce CO and H_2 has been postulated as a mechanism for the e-beam driven etching of hydrocarbon polymer (AZ-resist) under water vapor [2]. Teflon AF's, an amorphous fluoropolymer, radiation chemistry is influenced by the irradiation conditions as well as the presence or absence of a gas. Teflon (PTFE) can undergo both chain scission and cross linking, former is more frequently seen in the presence of oxygen at room temperature while the latter is more frequently observed under vacuum at higher temperatures [3, 4]. These results were the motivation behind the work presented in this dissertation. Next section briefly discusses the methods employed as a part of experimental research done in this work.
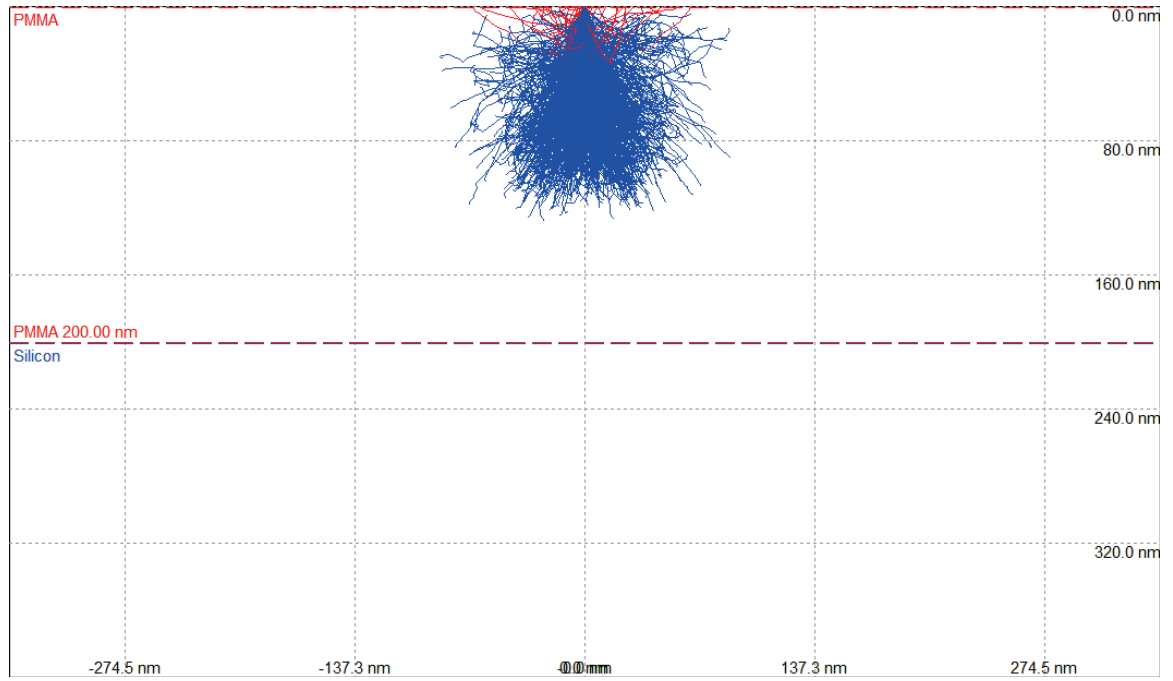
(a)
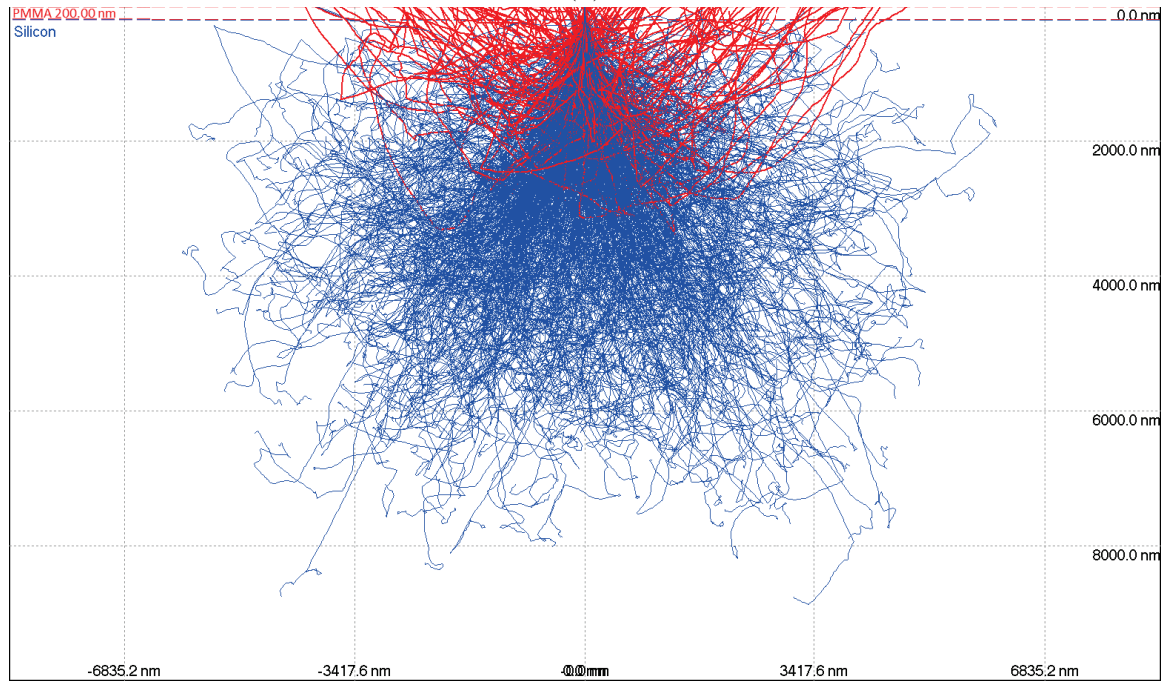
(b)

Figure 1.2: Electron trajectory in resist (PMMA) and substrate (Silicon) at a beam energy of (a) 2 keV and (b) 30 keV; using CASINO Monte Carlo simulator [1].

1.2 Methods

1.2.1 Spin Coating

Spin coating is an effective technique used to deposit uniform and homogeneous coatings of thin film onto a flat substrate. A typical spin coating process consists of dispensing a solution of the desired material in a solvent onto the substrate. Then the substrate is spun at low rotation speed for a few seconds to get a uniform spread of the solution over the substrate. The substrate is then brought to its final rotation speed; due to high centrifugal forces the solution tends to spread and thin out across the substrate while the solution simultaneously evaporates. Rotation is continued to achieve the desired film thickness. Once the spin coating is complete, the substrate is placed onto a hot plate or in a vacuum oven at a high temperature to remove any residual solvent.

The concentration, viscosity, and spinning speed of the solvent and solution all affect the films' thickness [5]. The film thickness decreases as the reciprocal of the square root of spin speed [6].

$$h \propto \frac{1}{\sqrt{\omega}} \tag{1.1}$$

where h is the final film thickness and ω is the spin speed.

1.2.2 Scanning electron microscopy (SEM)

Scanning electron microscopy (SEM) uses a focused beam of electrons, instead of light, to scan a sample and generate high-resolution images. When the electron beam hits the sample, interaction between the electrons and atoms in the sample produces a variety of signals; signal here includes the secondary electrons, backscattered electrons, diffracted backscattered electrons, X-rays, Auger electrons, etc. that are produced. The signal is then collected by a detector, usually a secondary electron detector or a backscattered electron detector, to produce high-resolution image that contains information about the surface topography and composition of the sample. SEM can also be used for determining (i) chemical composition of the sample using energy dispersive X-ray spectroscopy (EDS) detectors and, (ii) crystal structures and orientations of materials making up the sample using an electron backscatter diffraction (EBSD) detectors.

1.2.3 Variable Pressure Electron Beam Lithography (VP-eBL)

Variable-pressure electron-beam lithography (VP-EBL) employs an ambient gas at subatmospheric pressures to reduce charging during electron-beam lithography. Utilizing the charge-balancing mechanism of the variable pressure scanning electron microscope (VPSEM) and the high-resolution patterning capability of electron beam lithography, VP-eBL minimizes the charging effects during pattern exposure [7]. Using VP-eBL, pattern distortion artifacts from high vacuum eBL patterning on insulating substrates is eliminated, without the need conductive coatings.

1.2.4   Fourier transform infrared (FTIR) spectroscopy

The infrared spectrum of absorption, emission, and photoconductivity of solid, liquid, and gas can be obtained using the Fourier transform infrared spectroscopy (FTIR) technique [8]. FTIR analysis uses infrared light to scan the samples in order to identify organic, inorganic, and polymeric materials. Deviations from the typical absorption band pattern points to a change in the composition of the material. .

1.2.5   X-ray photoelectron spectroscopy (XPS)

X-ray photoelectron spectroscopy (XPS) which is based on the photoelectric effect is a quantitative spectroscopic technique frequently used by exposing the samples with X-rays for determining the surface chemistry of a material, typically probing to a depth of less than 10 nm. XPS is a surface-sensitive, non-destructive method that can measure a material's elemental composition in addition to the chemical and electronic states of its atoms. XPS measures the number and kinetic energy of the electrons emitted from the sample surface, thereby generating a photoelectron spectrum allowing the identification of the surface elements based on the energy and intensity of the photoelectron peaks. XPS can also be used to obtain the elemental composition across the sample surface by XPS depth profiling, where photoelectron spectrum are iteratively recorded by removing the material from the sample surface using ion-beam etching.

1.2.6   Confocal microscopy

Confocal microscopy is a powerful optical imaging technique that employs a modified fluorescence microscope and is used in various scientific fields, including biology, medicine, and materials science. It allows for obtaining high-resolution, three-dimensional images of specimens by using a focused laser beam to illuminate a single plane at a time. The light emitted from the specimen is then collected by a detector through a pinhole aperture, which blocks out-of-focus light from reaching the detector. Thus, providing improved optical resolution, resulting in clearer and more detailed images compared to traditional microscopy techniques.

1.2.7   Transmission electron microscopy (TEM)

Transmission electron microscopy (TEM) is an analytical microscopy technique that uses a beam of energetic electrons for ultra high-resolution imaging revealing the chemical and structural morphology of an ultra-thin section of the sample. As the accelerated electron beam passes through the sample, the interaction of the electrons with the sample produces a variety of signals; the transmitted and forward scattered electrons recombine to form an image that contains information about the crystal structure of the sample. Secondary signals can be used for obtaining compositional information of the sample.

1.2.8 Energy dispersive X-ray Spectroscopy (EDS)

Energy-dispersive X-ray spectroscopy (EDS) is an analytical technique that is used to extract information about the elemental composition or for performing chemical characterization of a sample. When a beam of electrons or X-ray interact with the sample it loses some of the absorbed energy to eject a core-shell electron from an atom leaving behind a hole. The vacancy created by the ejected core-shell electron is filled by a higher energy outer-shell electron, the energy difference between the outer-shell and the core-shell is released to produces characteristic X-rays. An energy-dispersive spectrometer records the number and energy of the characteristic X-rays emitted that is then used to determine the elemental composition of the sample.

1.2.9 Resist development

Typically, high molecular weight polymers dissolved in a liquid solvent make up the electron beam resists. Electron radiation of the resist causes the polymer to alter structurally. Electron beam resists can be either positive or negative. The scission of main- and side-chains following electron exposure weakens the positive resists, making the exposed resists more soluble in the developing solution. After exposure, the resist is typically immersed in a liquid developer. During development, the solvent penetrates into the polymer matrix and starts to surround the fragments. The resist film forms a positive tone pattern as a result of the solvent developer's selective removal of the weaker or lower molecular-weight resist. On the other hand, a radiation-induced cross-linking reaction strengthens the negative resists during exposure, making them less soluble in the developer. Temperature and duration become important parameters here as the hotter/longer the development, the farther along the continuum of solubility the dissolution extends [9].

1.3 Original contribution

The following contributions have been made while working on gas assisted electron beam patterning processes:

Contribution 1: Effect of water vapor pressure on positive and negative tone electron-beam patterning of poly(methyl methacrylate). In this work, VP-EBL was conducted on conductive substrates to study the effect of water vapor on PMMA patterning separately from the effects of charge dissipation. In addition, both positive and negative-tone processes were studied to determine the effect of water vapor on both chain scission and cross-linking. The contrast of PMMA was found to improve significantly with increasing water vapor pressure for both positive and negative-tone patterning. The clearing dose for positive-tone patterning increases moderately with vapor pressure as would be expected for electron scattering in a gas. However, the onset set dose for negative-tone patterning increased dramatically with pressure revealing a more significant change in the exposure mechanism. X-ray photoelectron spectra and infrared transmission spectra indicate that water vapor only slightly alters the composition of exposed PMMA. Also, electron scattering in water vapor yielded a much larger clear region around negative-tone patterns. This effect could be useful for increasing the range of the developed region around cross-linked PMMA beyond the backscattered electron range. Thus, VP-EBL for PMMA introduces a new means of tuning clearing/onset dose and contrast, while allowing additional control over the size of the cleared region around negative-tone patterns.

Contribution 2: Enhanced fluorescence from Polystyrene using gas assisted electron-beam patterning. This work presents a novel method for tuning and enhancing fluorescence properties from polystyrene (PS) through electron-beam (e-beam) irradiation under gaseous environments. We describe the effect of electron dose and ambient gas on the photoluminescence (PL) spectra and yield of electron irradiated PS films on insulating and conductive substrates. PS films were exposed in an environmental scanning electron microscope using a 20 keV electron-beam, ambient gas pressure ranging from $< 10^{-5}$ mbar (high vacuum) – 3 mbar, and the electron dose ranged from $1.8 - 45$ mC cm^{-2}. Irradiated PS films were characterized using confocal microscopy, Transmission electron microscopy (TEM), Energy dispersive X-ray Spectroscopy (EDS) and Fourier transform infrared (FTIR) spectroscopy. From emission spectra collected using confocal microscopy we found that the emission wavelength and photon yield of the irradiated film can be tuned by both dose and gas pressure, significant enhancements in the PL intensity – up to about 18 times on Sapphire substrate under helium environment compared to high-vacuum exposure – are observed. Overall, the highest PL yield is observed on soda lime glass substrate under argon environment. Also, the photon-yield on conductive substrates is significantly smaller than that yield from insulating substrates. The peak emission wavelength blue-shifts with increasing gas pressure and could be tuned in the $451 - 544$ nm range by varying dose and gas pressure. TEM images revealed e-beam irradiated PS are amorphous in nature and elemental mapping EDS revealed no signs of film oxidation. FTIR spectroscopy revealed that under gaseous environment the

decay of aromatic and aliphatic C–H stretches is reduced compared to the high vacuum exposure; in all cases, features associated with the phenyl rings are preserved. Localized e-beam synthesis of fluorophores in PS can be controlled by both dose and by ambient gas pressure. This technique could enable new approaches to photonics where fluorophores with tunable emission properties can be locally introduced by e-beam patterning.

Contribution 3: Enhanced contrast and high-resolution patterning of PMMA on insulating substrates under ambient gases. In this work, VP-EBL was conducted to study the effect of ambient gases on contrast and resolution of PMMA on conducting and insulating substrates. To our knowledge, these are the first studies of molecules other than water for EBL in gaseous environments. E-beam exposures were conducted under various gases to study their effect of on contrast of PMMA on conducting and insulating substrates, the contrast curves for PMMA on fused silica exposed under 1 mbar of helium, water, nitrogen and argon yielded contrast values of 13.6, 8.6, 7.7 and 9.7, respectively. The clearing dose increases with the gases' molecular weight and proton number, consistent with the increase in scattering cross-section. Our results for PMMA on silicon exposed under 1 mbar water vapor pressure yielded a contrast of 12.6, however, the contrast degrades on insulating substrates under water vapor and yields distinct values on fused silica and soda lime glass. The difference in contrast values on fused silica and soda lime glass could be correlated to differences in charge dissipation. Helium exhibits improved contrast in all cases. The improved contrast and sensitivity of PMMA exposed under helium motivated us to study the resolution under various gases. Resolution testing indicated that despite the lower clearing dose, helium still exhibited the best resolution with 25-nm half-pitch dense lines and spaces clearly resolved on soda lime glass. To our knowledge, this is the highest resolution demonstrated to date for EBL in a gaseous environment. Thus, VP-EBL of PMMA under helium yields higher sensitivity and contrast on insulating substrates without sacrificing resolution.

1.4   Outline of the Dissertation

This work provides a detailed description on the modifications in electron beam resist properties upon focused electron beam irradiation in gaseous environment on a variety of substrates. For each polymer, studies were coded based on the polymer, the gas, and the substrate as shown in Figure 1.3. Sensitivity, contrast, resolution and fluorescence are the material properties that have been investigated. PMMA, polystyrene, ZEP and HSQ are the most widely used positive (PMMA and ZEP) and negative resist (polystyrene and HSQ) making them the perfect choice for this work. The choice of gases to include helium, argon, water and nitrogen were based on reactivity to cover inert and reactive gases. Nitrogen was included as an ambient gas because it is often considered inert, but is reactive under ionizing radiation, hence can have interact differently than reactive and noble gases. Since material modification by electrons can be classified based on charge transport, substrates with different electrically conductivity's were incorporated.
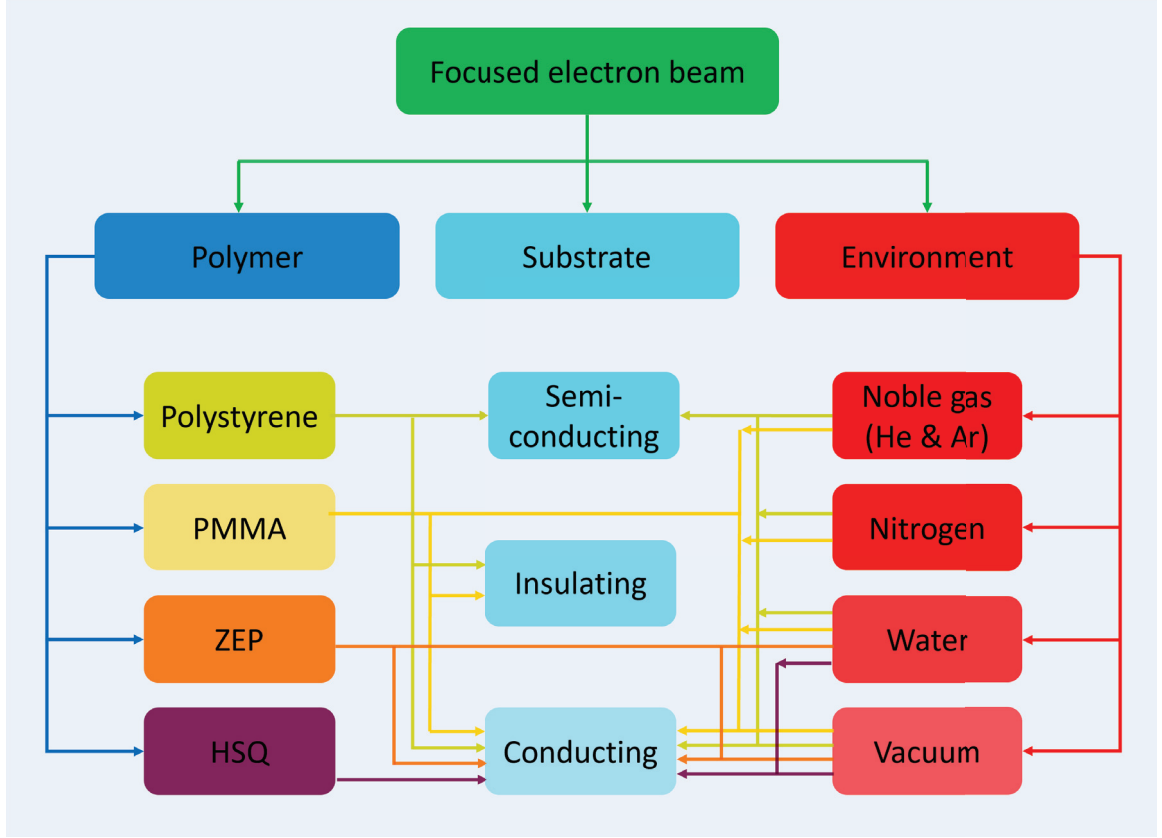
Figure 1.3: Experimental outline.

This dissertation is organized as follows: chapter 2 provides the details of the effects of water vapor on contrast and sensitivity during electron beam patterning of PMMA on a conductive substrate. Chapter 3 presents the enhanced fluorescence from Polystyrene using gas assisted electron-beam patterning. Chapter 4 presents the enhanced contrast and high-resolution patterning of PMMA on insulating substrates under ambient gases. Chapter 5 provides a future outlook for the application and improvement of the research introduced in the previous chapters. The results which did not provide a significant enhancement in material properties upon using gaseous environment over exposure under vacuum conditions are included in the appendix section of this dissertation.

Chapter 2 Effect of water vapor pressure on positive and negative tone electron-beam patterning of poly(methyl methacrylate)

2.1 Introduction

Electron-beam irradiation is a versatile method of modifying materials and forms the bases for electron-beam lithography of both organic and inorganic resists [10–27]. Poly(methyl methacrylate), PMMA, is the most widely used electron-beam resist due to its high resolution and stability [28]. It is well known that upon electron-beam irradiation at lower exposure doses, PMMA acts as a positive resist due to the chain scission of the polymer. At higher exposure doses, both cross-linking and compositional changes in PMMA show negative-tone resist behavior [29–33].

Variable-pressure electron-beam lithography (VP-EBL) employs an ambient gas at subatmospheric pressures to reduce charging during electron-beam lithography. Previous work demonstrated that VP-EBL can eliminate distortion and improve resolution when patterning PMMA on insulating substrates [7]. However, it remains unknown how water vapor pressure affects the contrast and clearing dose nor has anyone studied the effects of water vapor pressure on the negative-tone behavior of PMMA. In addition, water vapor has recently been shown to alter the radiation chemistry of the VP-EBL process for Teflon AF, an amorphous fluorinated polymer that can function as a positive or negative resist [34]. Such changes in radiation chemistry have not been explored for the VP-EBL of PMMA.

In this work, through systematically studying the effect of water vapor pressure on both the positive-tone behavior and negative-tone behavior of PMMA, we show that water vapor alters both the sensitivity and contrast of PMMA for both positive- and negative-tone processes. We find that water vapor only slightly changes the composition of exposed PMMA and, thus, hypothesize that changes in sensitivity and contrast are associated with changes in the distributions of molecular weight. We also show that the skirting effect of the forward scattering of electrons in water vapor [35] can control the size of the cleared region around negativetone patterns providing an alternative to large area positive-tone writing.

2.2 Experimental details

2.2.1 PMMA spin coating

PMMA (950 K molecular weight, MicroChem Corp.) was diluted using anisole (MicroChem Corp.) to make 4 wt. % solution. The PMMA solution thus prepared was spin coated onto a n-type ⟨100⟩ silicon substrate at 500 rpm for 5 s to give a uniform layer and then spun at 4000 rpm for 1 min to set the desired thickness. Next, the spin-coated Si substrate was heated on a hot plate at 180°C for 120 s to remove any residual solvent. Ellipsometry (M-2000, J. A. Woollam Co. Inc.) was used to measure the film thickness of the spin-coated PMMA film.

2.2.2 Variable-pressure electron-beam lithography process

An ELPHY Plus pattern generator (Raith GmbH) coupled with a FEI environmental scanning electron microscope (Quantum FEG 250) with a fast beam blanker was used for the VP-EBL process. An analytical working distance of 10 mm and a beam energy of 30 keV were used for all lithographic processes. A faraday cup and a pico-ammeter (Keathley 6487) were used for the beam current measurements under high vacuum conditions prior to each ithographic exposure. Gold nanoparticles deposited onto PMMA were used for focusing and as the marker during patterning.

For the positive-tone process, $20 \times 100~\mu m^2$ rectangular structures were exposed under high vacuum and water vapor (0.1, 1, 3, and 10 mbar) with areal exposure dose ranging from $10 - 300~\mu C~cm^{-2}$ with a step size of 12.8 nm and a beam current of 93 pA. The areal exposure dose, D, typically expressed in micro-Coulombs per square centimeter is determined from the following equation [36]:

$$D = \frac{T * I}{A} \tag{2.1}$$

where T is the time to expose the pattern (can be divided into exposure time/step size), I is the beam current and A is the exposed area. An electron-beam energy of 30 keV was chosen to reduce beam scattering in both water vapor and the resist, as well as to distribute backscattering to the largest range possible [37]. Each adjacent rectangle was given a $20~\mu m$ spacing to minimize proximity effects from backscattering. The exposed film was developed in 1:3 MiBK: IPA for 60 s at 18 °C followed by 30 s IPA rinse. Thickness measurements of the resulting resist surface were conducted using a Dektak 6 M (Veeco, Inc.) surface profiler.

For the negative-tone process, first, an array of single-pixel dots were exposed from 60 fC to 9 pC under high vacuum and water vapor (0.1, 1, 3, and 10 mbar) to estimate the onset areal dose. Then, an array of 20 rectangles ($5 \times 50~\mu m^2$) were exposed under the same conditions with an areal exposure dose from $1 - 40$ mC cm^{-2} with a 12.8 nm step size and a beam current of 414 pA. The film was developed in 1:2 MiBK: IPA for 60 s at 18 °C followed by 30 s IPA rinse. 1:2 MiBK: IPA is typically used in the negative-tone process to provide a slightly larger cleared area [30]. Additional features, numbers with arrow signs exposed at 20 mC cm^{-2}, were included close to the desired pattern and were used as markers for atomic force microscopy (AFM) measurements. For thickness measurements, AFM was performed using JPK NanoWizard 4 equipped with standard silicon cantilevers with pyramidal tips.

For the positive–tone process, samples for Fourier-transform infrared (FTIR) spectroscopy were prepared by exposing $200 \times 200~\mu m^2$ rectangular structures under high vacuum and water vapor (0.1, 1, 3, and 10 mbar) with areal exposure doses of 100 and 175 $\mu C~cm^{-2}$ using a step size of 12.8 nm and a beam current of 110 pA. Two different doses were chosen to accommodate the clearing dose for all vapor pressures. For the negative–tone process, samples were prepared for FTIR spectroscopy by exposing $250 \times 250~\mu m^2$ structures under high vacuum and 1 mbar water vapor with areal exposure doses of 15 and 40 mC cm^{-2} using a step size of 12.8 nm and a beam

Table 2.1: Experimental Conditions

	Chamber pressure	Beam current	Exposure Dose	Pattern size	Developer
Positive tone	Vacuum and 0.1–10 mbar water vapor	93 pA	10 – 300 μCcm^{-2}	20 × 100 μm^2	1:3 MiBK:IPA
Negative tone	Vacuum and 0.1–10 mbar water vapor	414 pA	1 – 40 mCcm^{-2}	5 × 50 μm^2	1:2 MiBK:IPA
FTIR positive tone	Vacuum and 0.1–10 mbar water vapor	110 pA	10 and 175 μC cm^{-2}	200 × 200 μm^2	undeveloped
XPS and FTIR negative tone	Vacuum and 1 mbar water vapor	5.9 nA	15 and 40 mC cm^{-2}	250 × 250 μm^2	1:2 MiBK:IPA

current of 5.9 nA. The beam current and structure size varied between experiments to keep exposure times to a reasonable duration. The difference in beam current used for FTIR samples for the positive-tone patterns arises from small changes in beam current over the course of the study. The experimental conditions are tabulated in Table 2.1.

2.2.3 X-ray photoelectron spectroscopy

A Thermo Scientific K-Alpha X-ray Photoelectron Spectrometer was used for surface analysis. X-ray photoelectron spectroscopy (XPS) was performed on as-coated PMMA samples and samples exposed at high doses under high vacuum and under 1 mbar water vapor. An areal exposure dose of 40 mC cm^{-2} was used for patterning XPS samples. In both cases, we sputter the surface of the PMMA with argon ions to remove any adventitious carbon. Preliminary peak fitting was conducted in Thermo Advantage software. Final fitting was completed using custom Python code based on the lmfit module [38], which allowed detailed error analysis. Details of the peak fitting strategies for the various samples are provided in Section 2.3.2.

2.2.4 Fourier-transform infrared spectroscopy

A Thermo Fisher Scientific Nicolet 6700 FTIR spectrometer coupled to an infrared microscope was used to acquire the infrared transmission spectra. For the positive-tone process, measurements were taken for undeveloped samples. For negative-tone FTIR spectroscopy, measurements were taken both before and after sample development. Larger patterns were exposed for samples prepared for FTIR measurements to meet the minimum spot size requirement of the instrument. During measurements, the illuminated region was well within the exposed region. Transmission spectra were acquired for as-coated PMMA and exposed patterns.

2.3 Results and discussions

PMMA films were spin coated onto silicon substrates and exposed at varying electron-beam currents, areal doses (charge/ area), and water vapor pressures. This work was conducted to study the effect o f w ater v apor p ressure o n b oth t he positive- and negative-tone behavior of PMMA. Contrast curves were obtained to observe changes in the contrast and sensitivity under water vapor. SEM (scanning electron microscopy), XPS analysis, and Fourier-transform infrared spectroscopy analysis were performed on the exposed patterns before and after development to measure changes in surface and chemical composition as a function of exposure conditions.

2.3.1 Effect of water vapor on e-beam patterning of PMMA in the positive-tone process

The increased solubility of the exposed areas in a developer caused by the degradation of PMMA by electron beam makes it a suitable candidate as a positive e-beam resist. Main chain scission in PMMA can result from the cleavage of the methyl ester side group to form a polymer radical [path (i) in Figure 2.1] and has been found to be the major initiator of polymer degradation. The cleaved methyl ester side group then either undergoes further decomposition, leading to the release of CO, CO_2, CH_4, CH_3OH, etc., or combines with other radicals. This is followed by the competitive processes of main chain scission or hydrogen abstraction [paths (ii) and (iv)]. Hydrogen abstraction results in a double bond formation in the main chain or side group. Main chain scission can also result from the direct action of a primary or secondary electron on a C–C bond shown by path (iii) but not been found to be the major initiator of polymer degradation.

Positive-tone contrast curves

To study the effect of water vapor pressure on positive-tone behavior, the contrast values of the exposed and developed pattern were measured. The positive-tone contrast curves, normalized residual resist thickness (NRT) versus areal exposure dose, D,are plotted for different water vapor pressures in Figure 2.2. No significant relief pattern before development was observed under either high vacuum or water vapor, indicating that no direct etching of the PMMA is occurring in this dose range.

The dose to clear, D_C, and contrast, γ,in Figure 2.3 were obtained by fitting the data in to an empirical model of the form [42],

$$NRT = C_0 - e^{S(D-D_C)} \qquad (2.2)$$

where C_0, S, and D_C are the fitting parameters. For most cases, $C_0 \approx 1$. S is determines how sharply the curve changes with dose, and D_C is the dose to clear. The contrast, γ, can be obtained from [42],

$$\gamma = ln(10)SD_C \qquad (2.3)$$
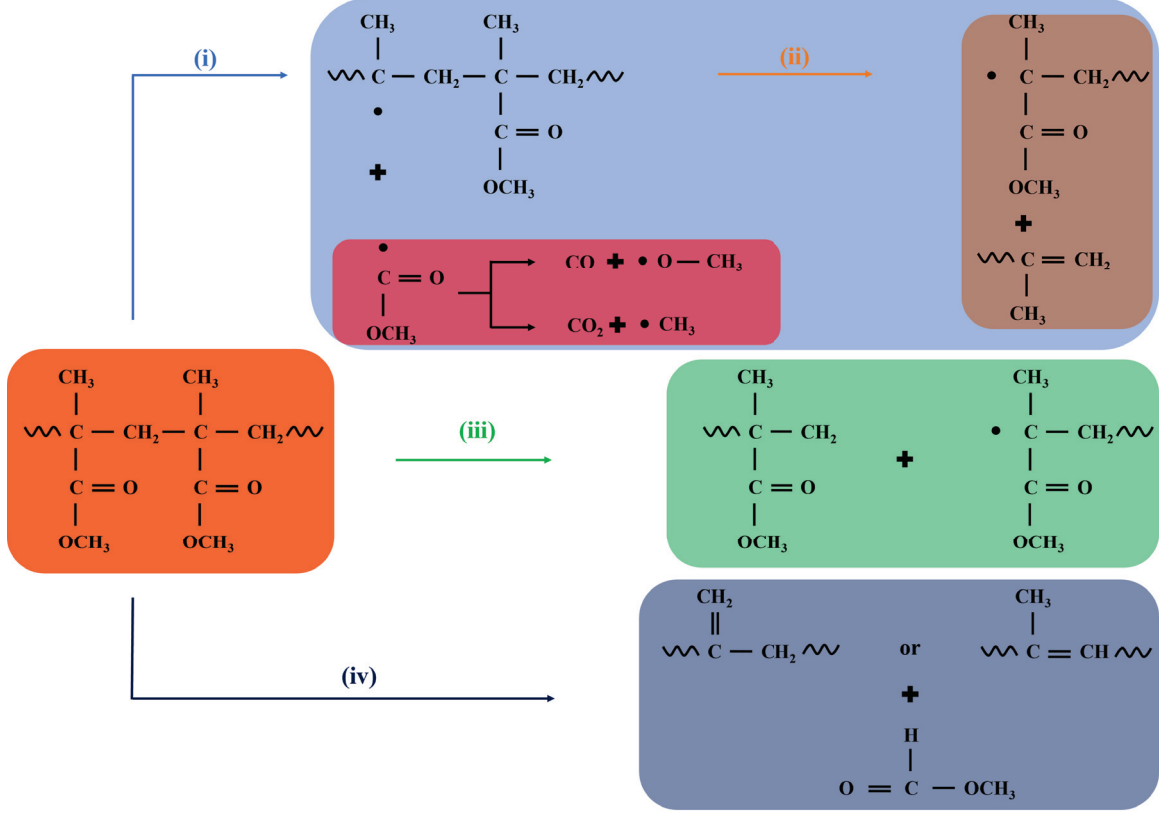
Figure 2.1: Schematics showing possible reaction paths for radiation damage in PMMA, as described in Refs. [39–41]. Cleavage of the methyl ester group (i) by a primary or secondary electron leads to subsequent main chain scission (ii) or C=C bond formation by hydrogen abstraction (iv). Direct action of an electron can also lead to main chain scission (iii).

Table 2.2: Contrast (γ) and dose to clear (D_C) as a function of vapor pressure for the positive-tone exposure of PMMA.

Chamber pressure	High vacuum	0.1 mbar H_2O	1 mbar H_2O	3 mbar H_2O	10 mbar H_2O
Contrast	7.1 ± 0.6	5.9 ± 0.9	6.8 ± 0.6	7.6 ± 0.6	8.1 ± 0.4
Dose to clear ($\mu C\ cm^{-2}$)	109 ± 1	111 ± 2	110 ± 1	115 ± 1	162 ± 1

The experimental data and fitted curves for each water vapor pressure are shown in Figure 2.3. Data points not well modeled by 2.2, i.e., those with small or zero residual resist thickness, were excluded from the fitting process and are marked by an " x ". Standard errors of the fitting parameters were calculated from the diagonal entries of the covariance matrix. Table 2.2 summarizes the contrast and dose to clear for exposure under high vacuum and each water vapor pressure. Figure 2.4 plots these parameters versus water vapor pressure.
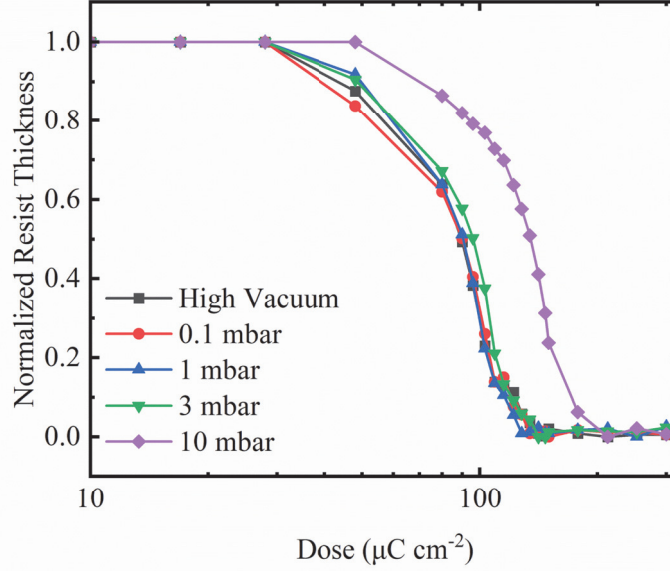
Figure 2.2: Normalized residual resist thickness vs exposure dose (experimental values) for PMMA exposed under high vacuum and water vapor pressures ranging from 0.1 to 10 mbar.

We note that the absolute values for contrast and clearing dose could be affected by proximity effects. The spacing of the features (20 μm) is sufficient that exposure by backscattered electrons will have a small effect at 30 keV. However, forward scattering in water vapor, especially at higher pressures, may have a more significant effect. Danilatos [43] showed that the beam skirt radius from plural scattering in a gas can be approximated by

$$R_s = 364 \left(\frac{Z}{E}\right) \left(\frac{P}{T}\right)^{1/2} L^{3/2},\tag{2.4}$$

where a circle of radius R_s, in meters, encompasses 90% of the scattered electrons, Z is the effective atomic number (7.42 for water vapor) [35] of the scatterer, E is the primary electron energy in eV, P is the pressure in pascals, T is the temperature in Kelvin, and L is the gas path length in meters. For the conditions considered here, the skirt radius ranges from 16 μm at 0.1 mbar to 160 μm at 10 mbar. Clearly, proximity effects arising from gas scattering will alter the measured dose to clear for all but the high vacuum and 1 mbar data.

Upon introducing water vapor, the contrast decreases and then increases steadily with increasing water vapor pressure. An empirical line fit of the form

$$\gamma = \alpha + \beta \cdot ln \left(\frac{PH_2O}{1mbar}\right)\tag{2.5}$$

with $\alpha = 6.9 \pm 0.06$ and $\beta = 0.50 \pm 0.03$ indicates that there is a statistically significant increase in contrast to water vapor pressure as shown in Figure 2.4(a). Thus,

15

Table 2.3: Vibrational mode assignments for PMMA from FTIR transmission data.

Wavenumber (cm^{-1})	Modes (Refs. [45, 46])	
3000	C—H	Asymmetric stretching
	O—CH$_3$	Asymmetric stretching
2952	O—CH$_3$	Symmetric stretching
	CH$_2$	Asymmetric stretching
	C—CH$_3$	Symmetric stretching
1730	C=O	Stretching
1483	CH$_2$	Bending
1450	C—H	Asymmetric bending
1435 and 1388	C—H	Symmetric bending
1272, 1242, 1193 and 1149	C—O—C	Stretching
989	O—CH$_3$	Rocking
842	CH$_2$	Rocking
750	C—C	Stretching

the transition of the exposed region from insoluble to soluble in a developer solution is found to be sharper with increasing water vapor pressure. This change in the differential solubility of the exposed PMMA could arise from changes in the chemical composition or from changes in the molecular weight distribution as discussed in the next section. The increase in dose to clear with water vapor pressure is shown in Figure 2.4(b). The dose to clear increases sharply beyond 3 mbar. This reduction in sensitivity could simply be the result of electron scattering in water vapor [44] or could be related to changes in the composition or the molecular weight in the exposed PMMA.

Infrared spectroscopy of positive-tone PMMA

Infrared transmission spectra of PMMA exposed under high vacuum and water vapor, as well as unexposed PMMA, were obtained to observe any changes in the chemical signature after exposure. Measurements were taken of undeveloped patterns exposed at 100 and 175 μC cm^{-2}. The peaks present in unexposed PMMA and their respective mode assignments from infrared transmission data are summarized in Table III.

The infrared transmission spectra of PMMA irradiated at 175 μC cm^{-2} under high vacuum and water vapor (0.1, 1, 3, and 10 mbar) are compared in Figure 2.5(a). Figure 2.5(b) shows the infrared transmission spectra of unexposed PMMA and PMMA irradiated at 100 μC cm^{-2} under high vacuum and water vapor (0.1, 1, 3, and 10 mbar). In both cases, the chemical signature of the irradiated patterns is not significantly altered for the dose range used for positive-tone patterning. Furthermore, the presence of water vapor does not change the IR-active bonding. In the absence of chemical changes, the alteration of the molecular weight distribution of PMMA is the most likely explanation for the effect of water vapor on contrast.
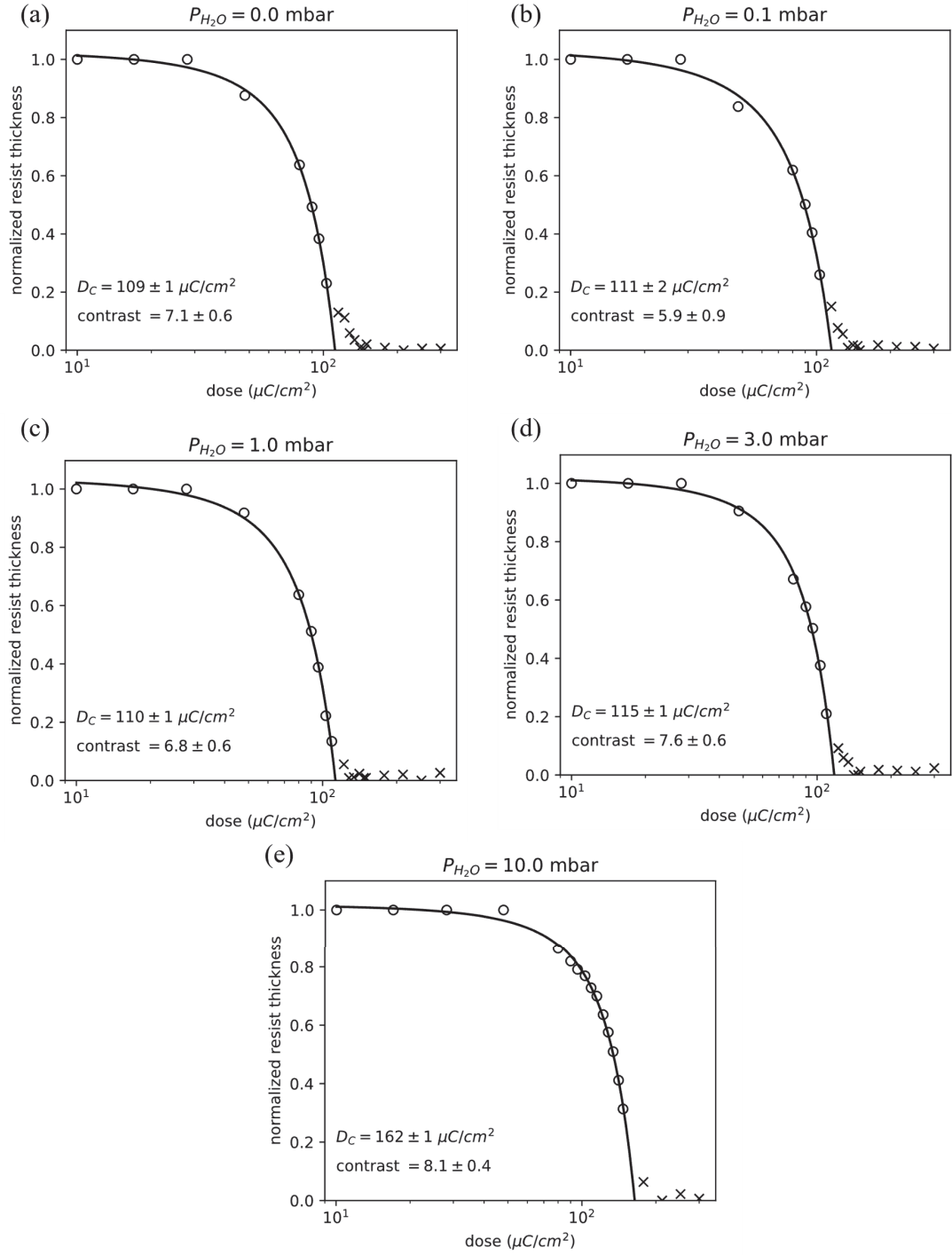
Figure 2.3: Fitted normalized resist thickness vs exposure dose (PMMA) for each water vapor pressure used during resist exposure. (a) High vacuum; (b) 0.1; (c) 1; (d) 3; and (e) 10 mbar. Data points used for the fit are indicated by a ∘, while data points excluded from the fit are indicated by an ×. Dose to clear, D_C, and contrast for each data set are shown in the inset. Uncertainties represent the standard error of the fitted parameter.
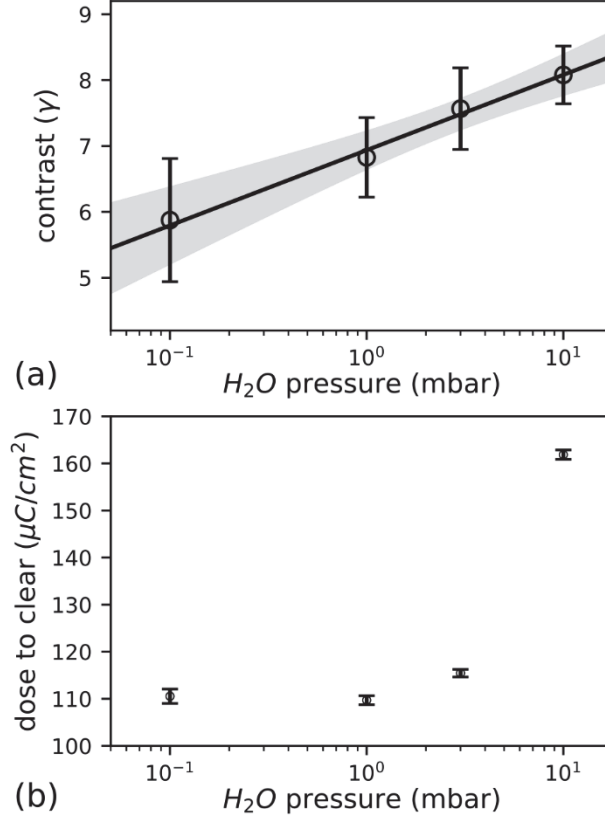
Figure 2.4: (a) Contrast as a function of water vapor pressure. The fitted line and corresponding 95% confidence bands (gray fill) show the statistically significant increase in contrast to vapor pressure. (b) Dose to clear as a function of water vapor pressure. The dose to clear increases sharply beyond 3 mbar. Error bars correspond to the standard error of the fitted parameters.

Detailed studies of molecular weight distributions are beyond the scope of this work; however, one can readily identify radiation-chemical mechanisms associated with water radiolysis that would alter these distributions. Water radiolysis in environmental SEM, and subsequent beam damage to organic materials, is well established [47–49]. Likewise, enhanced etching of carbonaceous materials in water vapor has been observed for both electron beam [50] and ion beam [51–53] based processes. Consider, for example, H· and ·OH radicals generated by water radiolysis. These radicals can abstract hydrogen from unexposed PMMA chains, leading to unstable polymer radicals and subsequent main chain scission through mechanism (ii) in Figure 2.1. Alternatively, these radicals can abstract hydrogen from polymer radicals previously generated by methyl ester cleavage. In this case, hydrogen abstraction would stabilize the polymer chain by mechanism (iv). Thus, depending on the relative abundance of polymer radicals and radiolysis products, the process could accelerate or slow main chain scission. Although atomic oxygen is not efficiently generated in hydrated samples [47], it is expected in the vapor phase particularly in the presence of low-energy secondary electrons [54–56] Atomic oxygen can directly react with PMMA
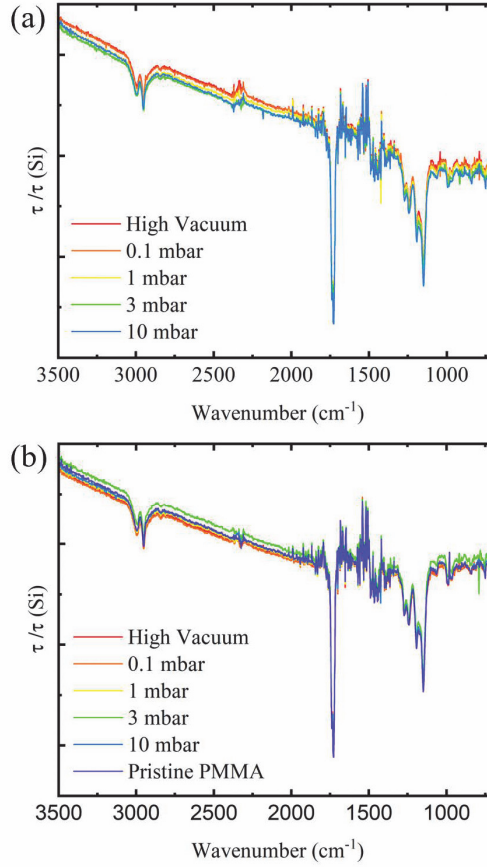
Figure 2.5: Infrared transmission spectra of (a) PMMA irradiated at 175 μC cm^{-2} under high vacuum and water vapor (0.1, 1, 3, and 10 mbar); (b) unexposed (pristine) PMMA and PMMA irradiated at 100 μC cm^{-2} under high vacuum and water vapor (0.1, 1, 3, and 10 mbar).

chains to form volatile products, e.g., CO_2, which would reduce the molecule weight. Complicating matters further, it is also possible that the local water concentration is depleted by radiolysis, especially at higher doses. The details of how these processes compete to reduce contrast at lower vapor pressures and increase contrast at higher pressures are not currently understood. Establishing the details of the process will require extensive experiments and simulations to ascertain the reaction pathways along with the reaction rates among polymer chains, polymer radicals, and radiolysis products. However, simpler experiments that vary beam current, and thus, dose rate, along with dwell and refresh times to study water depletion, may increase the understanding of the underlying mechanism.

2.3.2 Effect of water vapor on negative-tone patterning of PMMA

The decreased solubility of the exposed region in a developer caused by the cross-linking of PMMA at higher exposure doses makes it function as a negative e-beam resist. Cross-linking among polymer chains leads to the increased molecular weight of the resist. The widely accepted reaction mechanism suggests that scission and cross-linking are not independent processes. Cross-linking occurs at sites that have previously undergone chain scission via path (i) of Figure 2.1. The C=C bonding occurs at scissioned end groups, leading to cross-linking (Figure 6) [57]. The XPS results discussed below also suggest that additional linkages may form through C–O bonding.
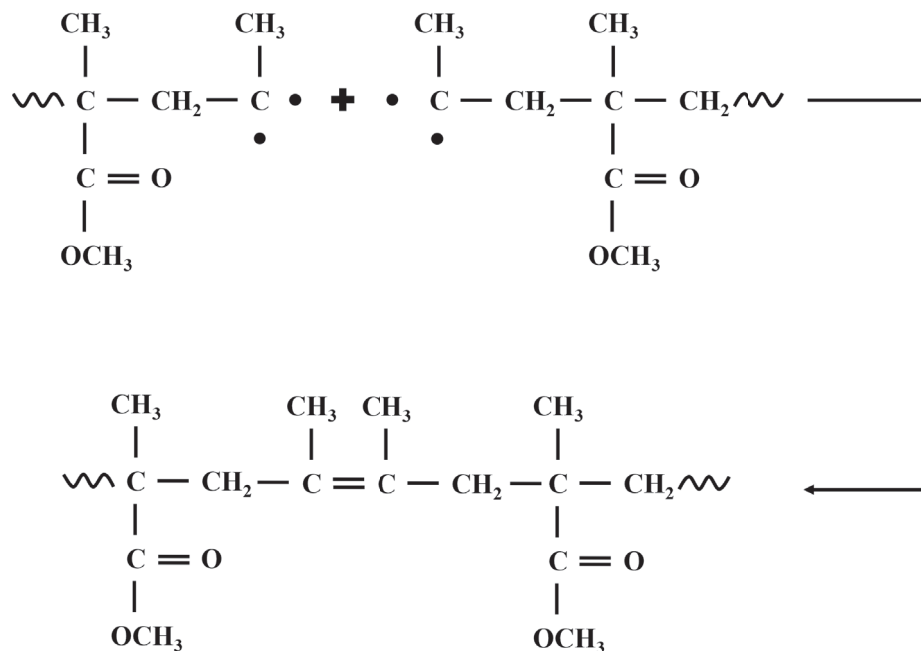
Figure 2.6: Reaction mechanism for main chain recombination resulting in the cross-linking of the end groups (Ref. [57]). Reproduced with permission from Lehockey et al., J. Vac. Sci. Technol. A 6, 2221 (1988). Copyright 1988 American Vacuum Society.

Negative-tone contrast curves

Figure 2.7 shows the contrast curve for high-dose exposure of PMMA. The onset dose increases with increasing water vapor pressure. The final cross-linked resist thickness decreases with increasing water vapor pressure. This indicates that the water-assisted e-beam induced etching of PMMA may significantly contribute to the process at these doses and pressures. The dose range used for these experiments was not sufficient to saturate the final resist thickness for 10 mbar water vapor exposure. Therefore, the normalized resist thickness and subsequent curve fitting has not been performed on 10 mbar water vapor data.
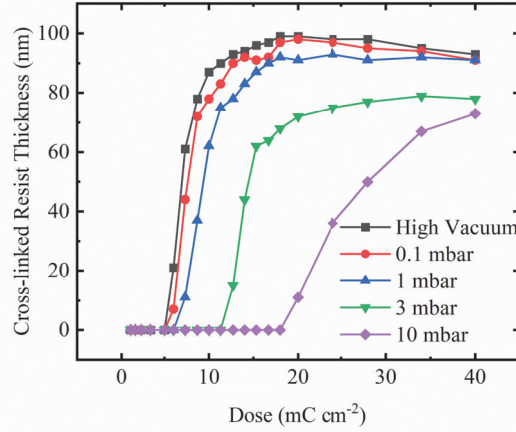
Figure 2.7: Contrast curves for higher exposure dose of array of 20 rectangles ($5 \times 50~\mu m^2$). The exposure dose varied in the range of 1–40 mC cm^{-2}.

For negative-tone patterning, the normalized remaining resist thickness was fitted with an empirical model of the form,

$$NRT = C_0 - e^{S(D_0 - D)} \tag{2.6}$$

where the parameters are the same as the model in Eq. 2.2 except that D_0 represents the onset dose for negative-tone behavior. The fitted contrast curve for each water vapor pressure is shown in Figure 2.8, and Table 2.4 lists the contrast for each pressure. A drop in contrast, like that observed in the positive-tone process, at 0.1 mbar water vapor was seen when compared to high vacuum exposure. The contrast increases at higher pressures as observed for positive-tone behavior.

The cross-linking onset dose increases approximately linearly with water vapor pressure as shown in Figure 2.9. The onset dose for cross-linking increases by a factor of 4 at 10 mbar water vapor as compared to high vacuum exposure. This large, approximately linear shift in onset dose is in stark contrast to the relatively small ($\sim$50%) and abrupt increase observed for dose to clear in positive-tone patterning. Such a dramatic difference between positive- and negative-tone behaviors cannot be explained by the simple scattering of electrons in water vapor. In the absence of compositional changes in the exposed materials, discussed below, these results again suggest that water vapor leads to the modification of the molecular weight, and molecular weight distribution, of exposed PMMA.

Table 2.4: Contrast (γ) as a function of vapor pressure for the negative-tone behavior.

Chamber pressure	High vacuum	0.1 mbar H$_2$O	1 mbar H$_2$O	3 mbar H$_2$O
Contrast (γ)	6.5 ± 0.4	5.5 ± 0.8	6.6 ± 0.5	8.2 ± 1.2
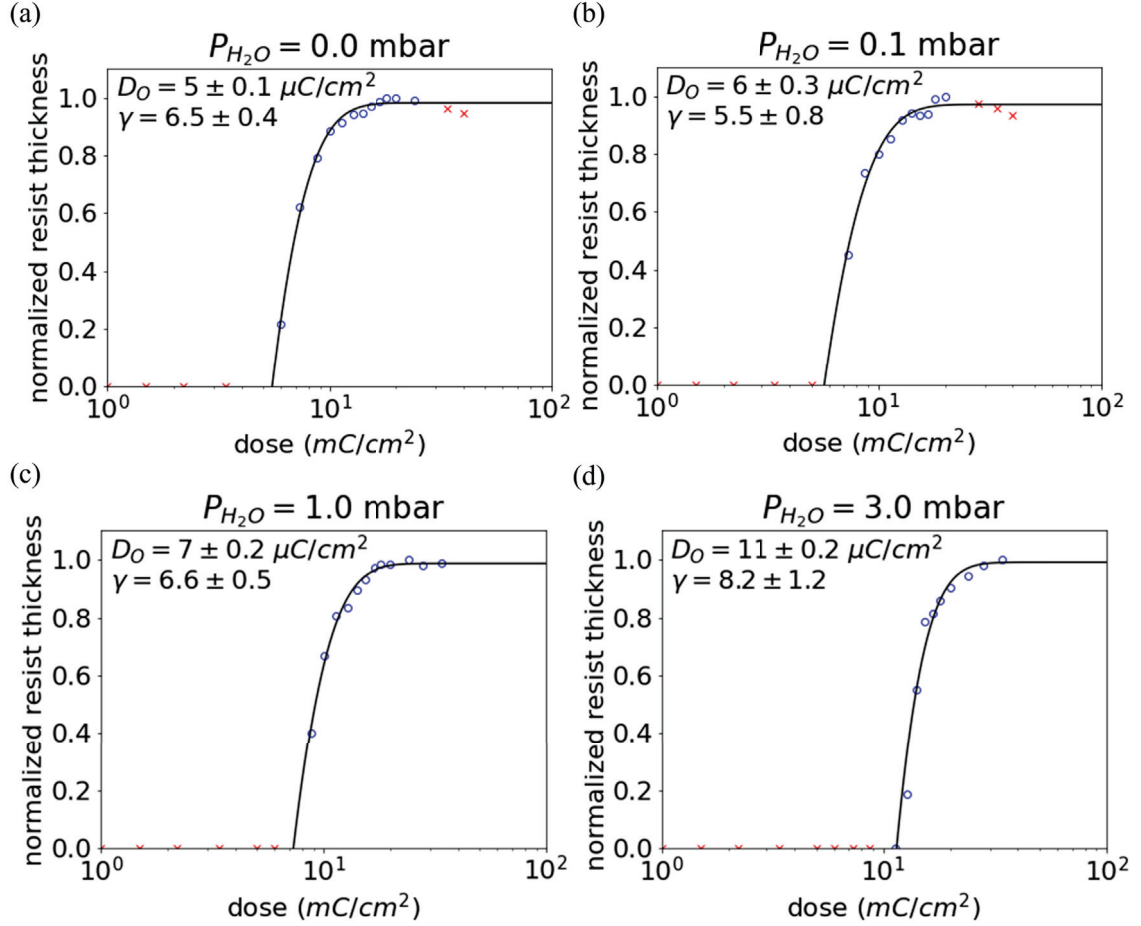
Figure 2.8: Normalized resist thickness (experimental and fitted) vs exposure dose as a function of water vapor pressure: (a) high vacuum; (b) 0.1; (c) 1; and (d) 3 mbar. Onset dose, D_0, and contrast, γ, from the fitted model are shown for each water vapor pressure. Data points not well modeled by a standard contrast curve are excluded from the fit and indicated by an $\times$.

Under vacuum and under water vapor, the thickness of cross-linked PMMA reaches a maximum just beyond the threshold for the negative-tone behavior. The resist thickness decreases with increasing dose beyond threshold for high vacuum and 0.1 mbar water vapor pressure. The reduction in the final resist thickness with increasing dose, even in the absence of water vapor, suggests that compaction may be occurring at higher doses. In contrast to the positive-tone process, a reduction in the resist thickness was also noted before development at the doses required for negative-tone behavior. Specifically, at 15 mC cm^{-2} during the negative-tone process under high vacuum and 1 mbar water vapor, the PMMA thickness was reduced by 40% before development. Topography changes in PMMA before development upon irradiation have been widely reported in the literature [17, 58–64]. The film thickness decrease in the original material depends on the exposure method used.
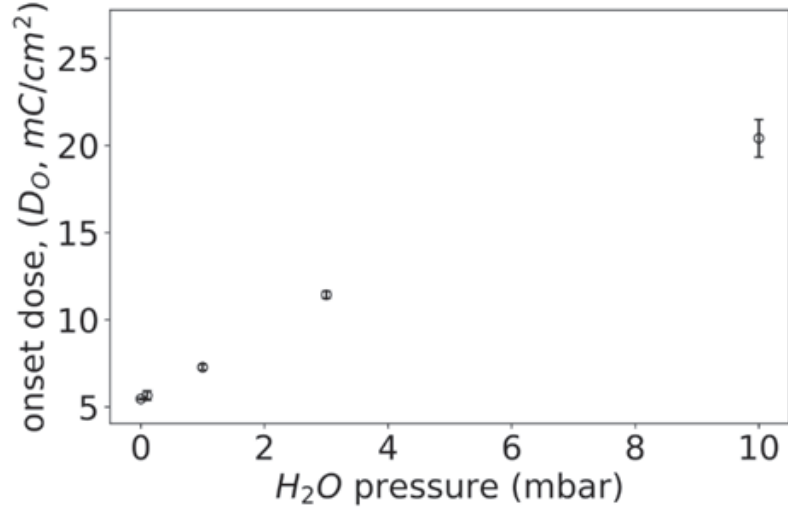
Figure 2.9: Onset dose for cross-linking as a function of water vapor pressure. Error bars represent the standard error of the fit for the contrast curves.

VP-SEM as an alternative to large area positive-tone writing
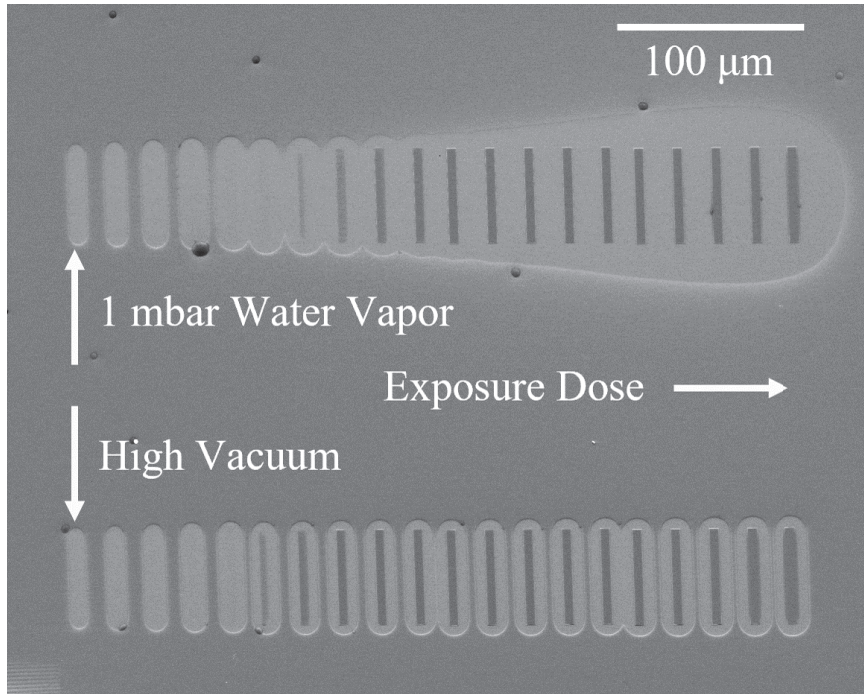
Figure 2.10: SEM image of 5×50 μm^2 rectangular array structures exposed in the dose range of 1–40 mC cm^{-2} under vacuum (lower pattern) and 1 mbar water vapor (upper pattern).

Figure 2.10 shows the scanning electron microscopy (SEM) image of structures exposed in the dose range of 1–40 mC cm^{-2} under vacuum (lower pattern) and under 1 mbar water vapor (upper pattern). The exposure dose increases from left to right. It was observed that below the threshold of ∼8 mC cm^{-2}, PMMA retains the positive-tone behavior, where chain scission remains dominant mechanism, causing the first five rectangles of the pattern to completely clear under vacuum conditions. At exposure doses beyond 28 mC cm^{-2}, an increase in the lateral dimensions of the developed pattern was observed. This is the result of the dose from backscattered electrons reaching the threshold for cross-linking near the patterned structure.
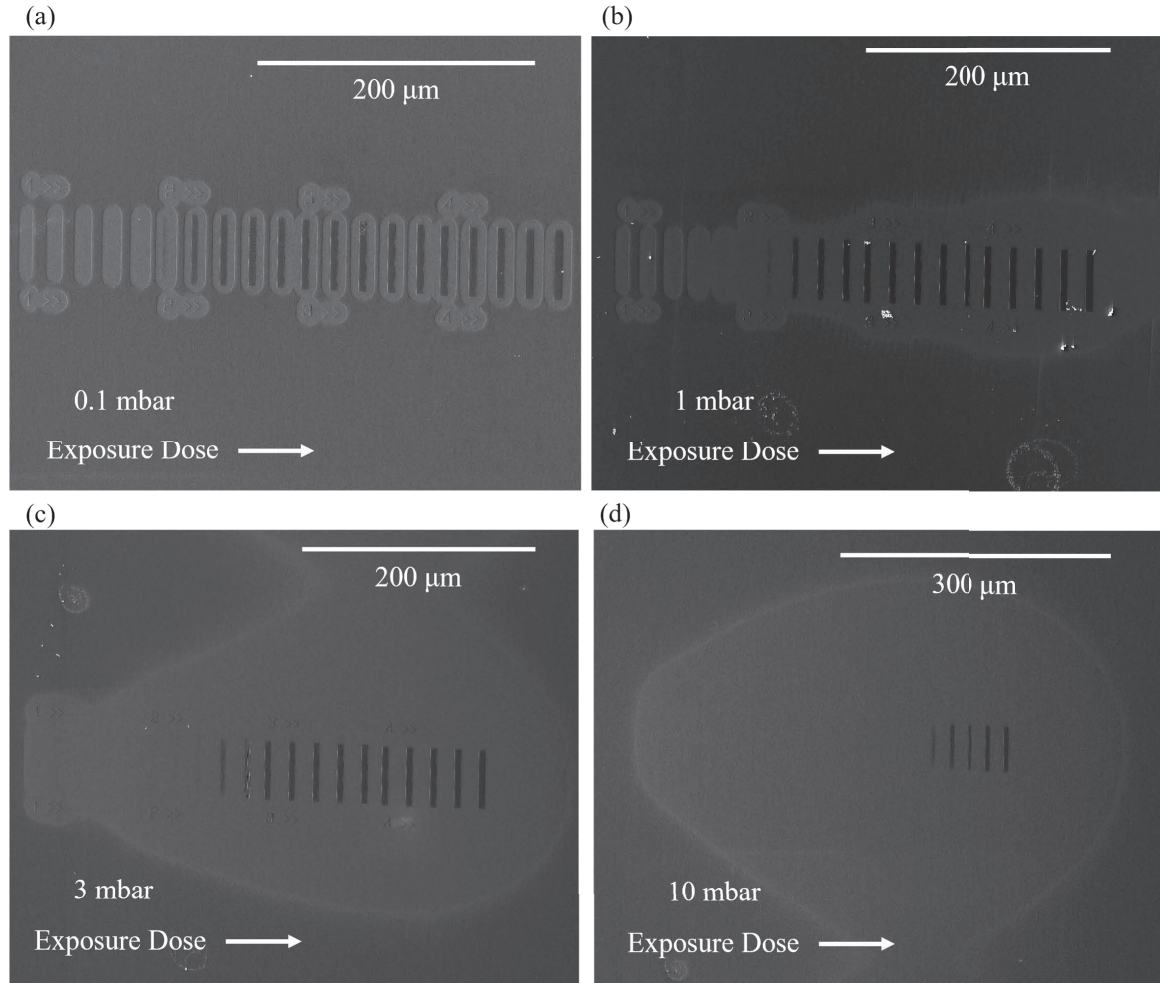
Figure 2.11: SEM images of patterns exposed in the dose range of 1–40 mC cm^{-2} under (a) 0.1; (b) 1; (c) 3; and (d) 10 mbar water vapor. Exposure dose increases from left to right.

The threshold for cross-linking increases with increasing water vapor pressure, as is evident from the SEM images in Figure 2.11. Figure 2.11 shows the SEM images for the same pattern, as shown in Figure 2.10, exposed under identical conditions with increasing vapor pressure from (a) to (d). Additional features, numbers with arrow signs, seen in these SEM images were used as markers for AFM measurements.

Other artifacts seen in the SEM images are gold nanoparticles that dispersed during development. Forward scattering in water vapor yields a much larger clear region around the negative-tone pattern with increasing vapor pressure. At higher water vapor pressures, the elastic scattering probability increases; thus, an increase in the extent of the beam skirt with increasing gas scattering is observed [35, 65].

This effect could be useful for increasing the range of the developed region around cross-linked PMMA far beyond the backscattered electron range. Moreover, the range can be easily tuned by varying the water vapor pressure. Thus, scattering in water vapor can control the size of the cleared region around negative tone pattern. This is advantageous compared to large area positive-tone exposures around the negative-tone pattern or attempting to control the size of the positive-tone region by pre-exposure treatments such as vacuum drying [66].

Infrared spectroscopy of negative-tone PMMA

Infrared transmission spectra were obtained for patterns irradiated at 15 and 40 mC cm^{-2} under high vacuum and 1 mbar water vapor to better understand the exposure mechanism. In a previous study, it was found that exposure to an electron beam degrades the PMMA to produce molecular hydrogen, carbon monoxide, and carbon dioxide [17]. The same study concluded that the methyl ester group in PMMA readily dissociates from the carbon backbone during irradiation. Figure 2.12 shows the comparison of transmission spectra under various conditions. High-dose electron-beam exposure causes the strong PMMA absorption peaks to broaden and weaken in the irradiated samples. Features associated with the carboxyl and methoxy groups are weakened upon e-beam exposure, but the presence of water vapor during exposure does not significantly alter the spectrum.

The methoxy group (C–O–C stretching) peak 1149, 1193, 1242, and 1272 cm^{-1} lines disappear from the irradiated samples. The C=O stretching peak at 1730 cm^{-1} broadens and shifts to lower energies. This is consistent with the conversion of unconjugated C=O bonds to conjugated C=O bonds (which appear at lower wavenumbers) [67] upon irradiation. The C–H stretching absorption peak assigned to wavenumber 2952 cm^{-1} broadens as well, whereas the C–H stretching mode assigned to 3000 cm^{-1} disappears for the irradiated samples. However, there was no significant difference observed for exposure under water vapor.

X-ray photoelectron spectroscopy of negative-tone PMMA

X-ray photoelectron spectroscopy (XPS) allows us to compare the chemical composition of unexposed PMMA with negative-tone (cross-linked) PMMA exposed under high vacuum and water vapor. Here, we use unexposed PMMA as a point of comparison and as a reference for establishing the binding energies and peak shapes of the relevant carbon–oxygen peaks. Subsequently, we use these parameters as a basis for fitting the XP spectra of exposed PMMA. In this way, we can draw some basic conclusions about the chemical composition of the cross-linked PMMA and the effects of water vapor on the process.
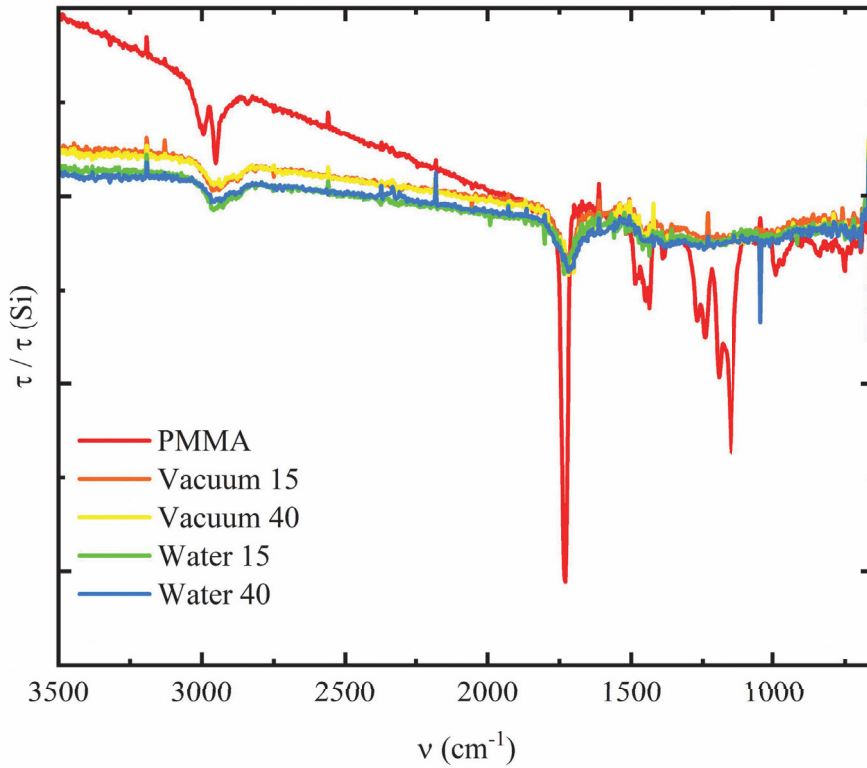
Figure 2.12: Infrared transmission spectra of PMMA unexposed (PMMA), exposed under 1 mbar water vapor, and exposed under high vacuum at 15 mC cm^{-2} (water 15 and vacuum 15) and 40 mC cm^{-2} (water 40 and vacuum 40). Features associated with the carboxyl and methoxy groups are weakened upon e-beam exposure, but the presence of water vapor during exposure does not significantly alter the spectrum.

For the C1s spectrum of unexposed PMMA, we assign four peaks to the five carbon atoms in the PMMA repeat unit as labeled in Figure 2.13(a). This approach was first proposed by Pijpers and Donners [68, 69] and its chemical significance has been confirmed by several additional studies (see, for example, Refs. [70–73]). Peak fitting was performed with the following constraints: (1) a Shirley background was used that did not exceed the data at any point; (2) all peaks were modeled with a Gaussian–Lorentzian sum (pseudoVoight) line shape; (3) a single Gaussian–Lorentzian mixing ratio was fit for all peaks; (4) the relative binding energies were constrained to those given by Naves de Brito et al. for bulk PMMA [70], and a single energy offset was fit to compensate for the small residual, charge-induced shift of the entire spectrum; (5) a single full width at half maximum (FWHM) was fit for all peaks as we do not have sufficient evidence that the intrinsic peak widths vary significantly for PMMA films more than a few nanometers thick [71, 72]; and (6) the initial peak areas were chosen based on the stoichiometric concentrations but were allowed to vary without constraint because PMMA is known to exhibit slightly nonstoichiometric area ratios [71].

26
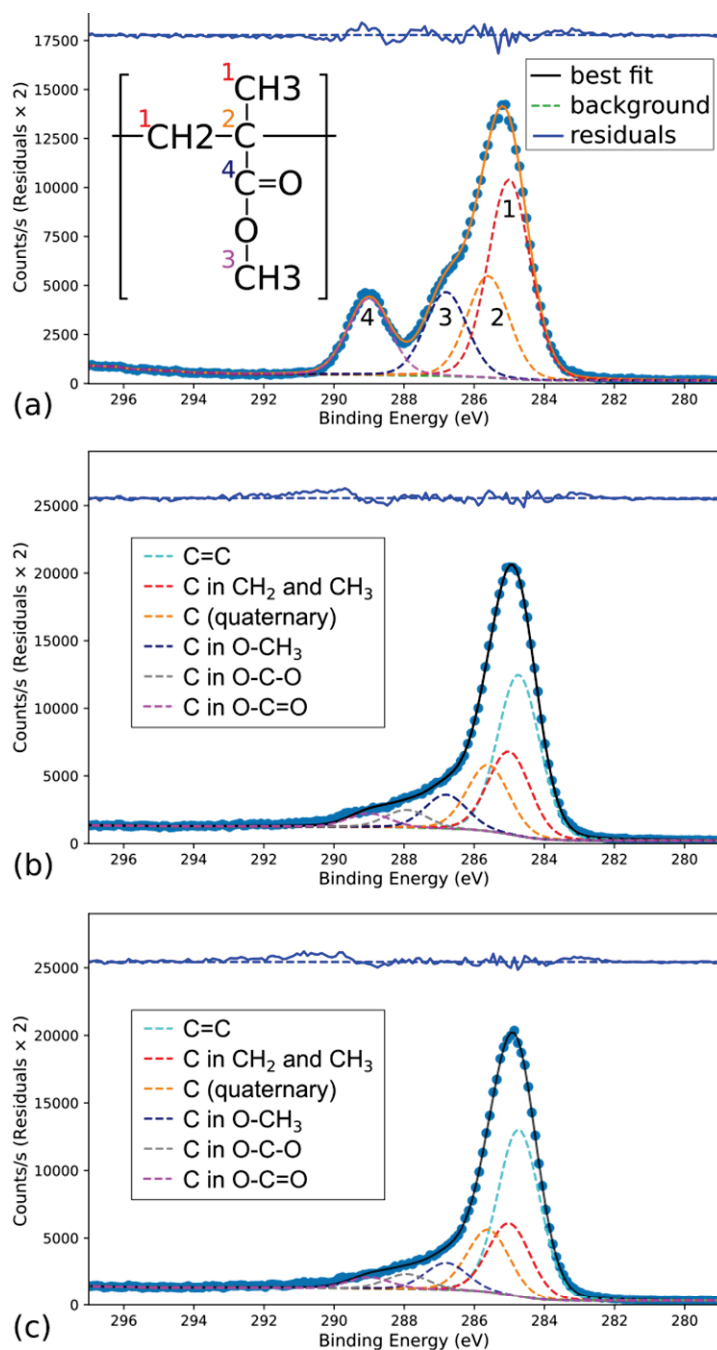
Figure 2.13: C1s x-ray photoelectron spectra for unexposed and negative-tone exposed PMMA. (a) Unexposed PMMA with a polymer structure shown in the inset. The numerical labels on the fitted peaks indicate the associated carbon atom. (b) PMMA exposed under high vacuum. (c) PMMA exposed under 1 mbar water vapor. The exposure dose for (b) and (c) is 40 mC cm^{-2}. For (b) and (c), two additional peaks are included to capture the presence of C=C and O–C–O moieties.

27

Table 2.5: XPS peak assignments and compositional analysis for unexposed PMMA. Uncertainties represent 95% confidence intervals for the fitted parameters. Parameters without uncertainties were fixed during the fit. All peaks: FWHM = 1.41 ± 0.02 eV, Gaussian/Lorentzian mixing ratio = 0.16 ± 0.02

Label	Bonding	Binding energy (eV)	Composition (at.%)
C1	CH_2 and CH_3	285.00 ±0.01	43 ± 1
C2	Quaternary C	285.60	22 ± 1
C3	O–CH_3	286.80	18.2 ± 0.5
C4	O–C=O	289.00	16.5 ± 0.3

The Gaussian–Lorentzian mixing ratio was determined from the pseudo-Voight profile, which is the sum of a Gaussian and Lorentzian. The Gaussian-Lorentzian sum (GLS) function has the following form [74]:

$$GLS(x; F, E, m_s, h) = h(1 - m_s) \exp \left[-4ln2 \frac{(x - E)^2}{F^2} \right] + \frac{hm_s}{\left[1 + 4\frac{(x-E)^2}{F^2} \right]} \qquad (2.7)$$

where x is the variable energy, F is the full width at half maximum (FWHM), E is the energy at the center of the peak, m is the mixing ratio between Gaussian and Lorentzian components, and h is the height of the function.

Figure 2.13(a) shows the XP spectrum for unexposed PMMA, the Shirley background, the four fitted peaks, and the residual error in the fit. Table 2.5 lists the binding energies and compositional analysis results. This peak fitting strategy provided a good fit to the data and showed good agreement with other studies of bulk PMMA (see, for example, Refs. [70] and [72]) including the slight nonstoichiometric compositional results. Perhaps more importantly, these fits allowed us to confirm the binding energies and constrain the FWHM and mixing ratio for the peaks used to fit the XP spectra for exposed PMMA discussed below.

PMMA regions exposed with a dose of 40 mC cm^{-2} under high vacuum and 1 mbar water vapor were also analyzed using XPS. The relative binding energies, FHWM, and mixing ratio from the unexposed PMMA were retained for the exposed PMMA analysis. However, prior studies have shown that cross-linked PMMA contains C=C bonds [57] and should have an additional peak shifted -0.27 eV from the C1 peak. In addition, none of the chemical shifts in unexposed PMMA account for the photoelectron signal near 288 eV in the cross-linked sample. Given the composition of PMMA, the only good candidate for this region is the carbon atom in O–C–O. We have added this peak based on the mean chemical shift (+2.93 eV) given by Gengenbach et al. [75] Naively fitting six peaks to the relatively smooth spectrum of cross-linked PMMA would be quite challenging and would lead to unacceptably large uncertainties for the peak parameters and the composition of the material. However, by retaining the relative binding energies, FWHM, and mixing ratio from unexposed PMMA measured at the same time and on the same substrate, we can sufficiently constrain the fit to draw some meaningful conclusions.

Table 2.6: XPS peak assignments and compositional analysis for PMMA exposed at 40 mC cm^{-2} under high vacuum and 1 mbar water vapor. Uncertainties represent 95% confidence intervals for the fitted parameters. Parameters without uncertainties were fixed during the fit.

Label	Bonding	Binding energy (eV)	Composition for exposure under high vacuum (at.%)	Composition for exposure under 1 mbar water vapor(at.%)
	C=C	284.73	43 ±8	47 ±8
C1	CH$_2$ and CH$_3$	285.00±0.08	22 ±8	20 ±8
C2	Quaternary C	285.60	18 ±1	18 ±1
C3	O–CH$_3$	286.80	9.0 ±0.4	7.6 ±0.4
	O–C–O$_3$	287.93	4.7 ±0.4	4.2 ±0.4
C4	O–C=O	289.00	3.6 ±0.3	3.2 ±0.3

Figures 2.13(b) and 2.13(c) show the XP spectra for PMMA exposed under high vacuum and water vapor, respectively. The Shirley background, the six fitted peaks, and the residual error in the fit are shown as well. Table 2.6 lists the binding energies and compositional analysis results. With regard to composition, it comes as no surprise that the area of the C=C peak is strongly negatively correlated with the area of the adjacent C1 peak associated with CH$_2$ and CH$_3$. This leads to substantial uncertainty in the relative compositions. Nevertheless, the confidence intervals exclude a zero concentration of C=C even at the 99.73% confidence level. Thus, our results reaffirm the conclusion of prior works, sometimes reported without the measures of uncertainty, that the cross-linking of PMMA occurs at least partially through C=C bonds. This result is also consistent with the infrared spectroscopy results of Sec. III B 3, which shows the transformation of unconjugated C=O bonds to conjugated C=O bonds after irradiation at similar doses.

The distinct shoulder and higher energy peak associated with C3 and C4, respectively, are markedly reduced upon irradiation. Neither result is surprising as side-group cleavage accompanies main chain scission in the electron-exposure of PMMA. More interesting is the photoelectron signal that appears to arise from O–C–O bonded carbon. Excluding this moiety significantly reduced the quality of the fit, and the confidence intervals for the area of the O–C–O peak exclude zero concentration even at the 99.73% confidence level. This suggests that cross-linking can also occur through a more complex linkage involving oxygen. Based on the spectra of acetal/ketal linkages, we would expect additional infrared absorption in the 1200–1010 cm^{-1} range. However, it would be difficult to detect the four to five unresolved features expected for such O–C–O linkages [67] in the infrared spectra of Figure 2.12. This is especially true given the low concentration identified by XPS. Thus, this observation should motivate further study to fully characterize the various cross-linking mechanisms for negative-tone PMMA.

These results add additional insight into the cross-linking process for negative-tone PMMA exposure beyond what has been previously presented in the literature.

However, the most important result for this study is that there are only very small chemical differences between negative-tone PMMA exposed under 1 mbar water vapor and PMMA exposed under high vacuum. The carbon–carbon bonded components (C1, C2, and C=C) do not show any statistically significant difference at the 95% confidence level. Among the carbon–oxygen bonded components, only C3 shows a small statistically significant compositional difference (1.4%). As noted above, these results are consistent with our infrared spectra, which also show only very small chemical differences between negative-tone exposure under vacuum and water vapor. This result contrasts with reported changes in the PMMA composition during ion-beam etching using large argon ion clusters with and without water vapor. In the case of ion-beam etching, XPS showed water vapor reduced the loss of C–O and O–C=O bonded carbon compared to irradiation in vacuum [76]. Even so, the argon ion cluster experiments represent a vastly different regime of total dose, dose rate, and localization of energy transfer.

Thus, x-ray photoelectron and infrared spectroscopy both suggest that water vapor does not change the composition of the cross-linked PMMA. Thus, compositional changes are not likely the source of the enhanced contrast and the dramatic change in onset dose observed for exposure under water vapor. Rather, reactions with water radiolysis products, as discussed in Section 2.3.1, may alter the molecular weight and molecular weight distributions.

2.4 Summary and Conclusions

Water vapor has recently been shown to alter the radiation chemistry of the VP-EBL process for Teflon AF [34]. In this work, VP-EBL was conducted to study the effect of water vapor on the positive- and negative-tone electron-beam patterning of PMMA, a conventional e-beam resist. Water vapor did not dramatically affect the sensitivity of PMMA for the positive-tone patterning at vapor pressures up to 3 mbar. However, the contrast of the positive- and the negative-tone process improved in the presence of water vapor. These results suggest that VP-EBL can be applied to positive-tone patterning PMMA without extensive changes to established process parameters. In contrast, water vapor dramatically increased the onset dose for negative-tone patterning and both compaction and direct etching appear to be significant. Improved contrast was also observed for negative-tone patterning at higher water vapor pressures. As a result, significant process modifications will be necessary when implementing VP-EBL for negative-tone PMMA patterning.

X-ray photoelectron spectra and infrared transmission spectra indicate that the presence of water vapor does not dramatically alter the composition of exposed PMMA. This is true for both positive- and negative-tone processes. Instead, changes in molecular weight distributions appear to be responsible for the altered contrast and contribute to the changes in clearing and onset dose. Further investigation is required to establish the radiation-chemical mechanisms, such as hydrogen abstraction by H· and ·OH, that can alter the chain scission and cross-linking processes and, thus, the molecular weight distributions.

Finally, scattering in water vapor can control the size of the cleared region around negative-tone patterns providing an alternative to large area positive-tone writing to achieve the same end. This effect could be useful for increasing the range of the developed region around cross-linked PMMA far beyond the backscattered electron range. Moreover, the range can be easily tuned by varying the water vapor pressure. All of these results emphasize the dramatic expansion of the lithographic parameter space when conducting electron-beam lithography under reactive gases.

Chapter 3 Enhanced fluorescence from Polystyrene using gas assisted electron-beam patterning

3.1 Introduction

Researchers have been drawn to carbon nanostructures for decades because of their abundant precursor materials and superior mechanical, electrical, and optical properties. Carbon dots (CDs), a member of the carbon nanostructure family, have numerous advantages which include ease of fabrication, low toxicity, low-cost, high-water solubility, chemical inertness, high stability, strong biocompatibility, and ease of functionalization. CDs have gained popularity for their excellent luminescent properties. Fluorescent CDs have been made using a variety of techniques, such as chemical oxidation [77], laser ablation [78], electrochemical synthesis [79], ultrasonic synthesis [80, 81], microwave pyrolysis [82], hydrothermal carbonization methods [83–85]. Organic fluorophores can be synthesized with many different emission wavelengths in wide spectral region and are used in wide ranging applications including chemical sensors [86], photovoltaics [87], bioimaging [88], and organic lasers [89].

Polystyrene (PS) consists of long hydrocarbon chains with a phenyl group in the repeating monomer unit (Figure 3.1). PS is a negative e-beam resist [90–97] and does not exhibit luminescence in the visible spectral region [98]. It is known that electron irradiation transforms PS from a non-luminescent polymer into a luminescent material [10, 99–102]. For example, PL from irradiated PS results from formation of polycyclic aromatic hydrocarbons (PAH) or carbon dots, assumed to be composed of PAH. In unrelated work, water vapor has been shown to modify chemical processes during e-beam irradiation of Teflon AF [3, 4, 34] and also alters the sensitivity and contrast of PMMA in e-beam lithography [103]. These prior efforts motivated us to study the effect of ambient gases on the e-beam induced synthesis of fluorophores in PS.

Here we describe the effect of electron dose and gas pressure on the emission spectra and photon yield of PS films irradiated with focused electron beams on a variety of substrates. Under high vacuum exposure, we found that increasing dose red-shifts the emission spectrum and increases the photon yield, which is consistent
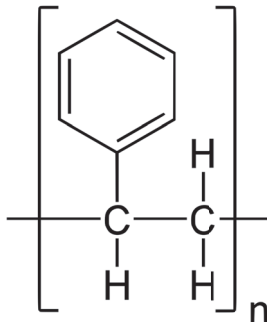
Figure 3.1: Chemical structure of Polystyrene

with prior work on electron irradiated PS. However, under ambient gases, we found that the emission wavelength and photon yield can be tuned by both electron dose and gas pressure and that dramatic enhancements in photoluminescence can be achieved. This technique could enable new approaches to photonics where fluorophores with tunable emission properties can be locally introduced by e-beam patterning.

3.2   Experimental details

3.2.1   Spin coating

Polystyrene (2.5K molecular weight, Scientific Polymer Products) was diluted with anisole (MicroChem Corp.) to make a 20 wt.% solution. The PS solution thus prepared was spin coated on electrically insulating (N-BK7, soda lime glass, fused silica and sapphire) and electrically conductive (silicon and ITO coated soda lime glass) substrates at 500 rpm for 5 seconds to give a uniform layer and then spun for one minute at 2000 rpm to achieve the thickness of ∼600 nm. Next, the spin-coated substrate was heated on a hot plate at 70°C for 1 hour to remove any residual solvent. A low baking temperature was chosen because low molecular weight PS thin films do not have good thermal stability [94]. Ellipsometry (M-2000, J. A. Woollam Co. Inc.) was used to measure the film thickness of the spin-coated PS film.

3.2.2   Variable-pressure electron-beam patterning
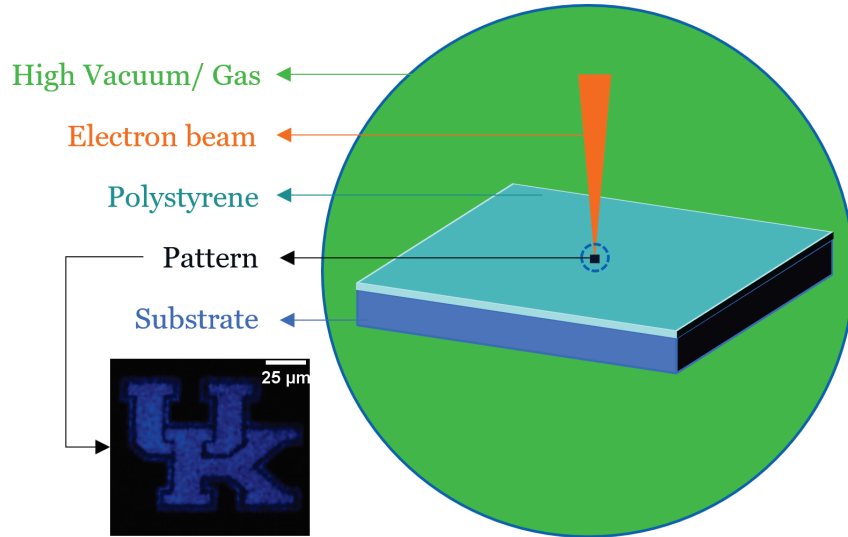
Figure 3.2: Schematic of electron-beam induced synthesis of fluorophores in polystyrene thin films. The PS film is irradiated by a focused electron beam either in high vacuum or under a subatmospheric-pressure gas.

An ELPHY Plus pattern generator (Raith GmbH) coupled with a FEI environmental scanning electron microscope (Quantum FEG 250) with a fast beam blanker was used for variable pressure electron beam patterning process, shown schematically

in Figure 3.2. A working distance of 10 mm and a beam energy of 20 keV were used for all patterning processes. 100 μm square patterns were exposed with a minimum of 100 μm spacing between each neighboring square. Exposures were carried out at beam currents ranging from 0.7 to 1 nA. Prior to each exposure process the beam current was measured under high vacuum conditions using a Faraday cup and a picoammeter (Keathley 6487).

3.2.3 Confocal microscopy

PL measurements from irradiated patterns were carried out at room temperature using a confocal microscope (Zeiss LSM 880 Upright Multi-photon Microscope) at 405 nm laser excitation. Samples were illuminated by a focused beam with a 10x objective lens (numerical aperture 0.5) using water as immersion fluid. PL from the sample was collected by the same objective and detected by a photomultiplier (ZEISS QUASAR photomultiplier detector). Laser power and spectral resolution were constant for all experiments.

3.2.4 Fourier-transform infrared (FTIR) spectroscopy

Infrared reflection spectra were collected using a Thermo Fisher Scientific Nicolet 6700 FTIR spectrometer coupled to an infrared microscope. The irradiated portion of the film was completely within the illuminated region during measurements. Reflection spectra were acquired for as-coated PS and exposed patterns.

3.2.5 Transmission electron microscopy (TEM)

PS exposed at 15 mC cm^{-2} under high vacuum and 1 mbar water vapor were characterized with TEM at an accelerating voltage of 200kV (Thermo Scientific™ Talos™ F200X). Images were acquired using 16M pixel 4k x 4k CMOS camera (Thermo Scientific™ Ceta). Elemental mapping energy dispersive X-ray spectroscopy (EDS) images were collected using Thermo Scientific™ Super-X EDS system at a beam current of approximately 0.8 nA.

3.3 Results and discussions

The effect of ionizing radiation on polymers is readily detected by the changes in molecular weight; molecular weight decreases when chain scisson is prevalent, but it increases when cross-linking is dominant. Presence of a phenyl group within the polymer molecule provides partial protection against these effects of ionizing radiation [104]. There are numerous studies investigating the range of protection offered by the phenyl radical in organic co-polymers against radiation induced cross-linking [104–109]. Significantly higher absorbed energy is required to cross-link PS, more than 2 orders of magnitude higher than many other long chain polymers [105], demonstrating the stabilizing effect of the phenyl group. Radiation studies of p-substituted PS's indicated that the aromatic rings do not participate either in cross-linking or chain scission [107].

Randall et al. [110] proposed that for irradiated solid state polyethylene with absorbed dose less than the gel dose, predominant cross-linking reaction leads to the formation of Y-links. However, Horii et al. [111] reported that H-links were predominantly present when molten state polyethylene is irradiated at higher doses. Also, when phenyl rings are present in the polymer chain, end links can also be formed where one or two chain scissioned reactive chain ends attach to the backbone of the second molecule [112]. All these indicate that the reaction mechanism is significantly affected by the absorbed dose (lower or higher absorbed dose than the gel dose leads to different reaction mechanism) and also by the presence of the phenyl rings in the polymer chain.

PS films show deep blue fluorescence around 410 nm upon electron irradiation [99], as the electron dose varies, the PL intensity and peak wavelength also change. The PL spectrum red-shifts with increasing electron dose. At lower doses, PL intensity increases with electron dose; however, after a critical electron dose, PL intensity falls as electron dose increases. The decrease in PL intensity beyond the critical threshold was attributed to the synthesis of new bonds in the polymer chain and the breakdown of the aromatic ring in pristine PS [100]. Similar trend of decreasing PL above critical threshold is observed upon ion irradiation of polysiloxanes and polycarbosilanes derived composite ceramics [113].

Exposing PS films to electron irradiation results in the formation of sp^2 carbon structures embedded in sp^3 bonds [99]. Irradiation causes an increase in the number of sp^2 carbon clusters, the source of PL emission, below the critical electron dose. A reduction in PL intensity above the critical dose is observed as a result of either damage to the carbon clusters or defect generation in the matrix [100].

[1]1H liquid nuclear magnetic resonance (NMR) and correlation spectroscopy has revealed the the existence of several small multi ring aromatic units in irradiated PS films such as biphenyl, 1-phenylnaphthalene, 1,4-dimethylnaphthalene and p-terphenyl; where as phenanthrene was found at higher electron dose irradiation [100]. However, these small multi ring aromatic units absorb mostly in the mid UV region and are weakly fluorescent in the visible region with only the tail of the emission spectrum extending in the visible region. Also, the NMR spectra were obtained only for PS samples irradiated at a low exposure dose since cross-linked PS is insoluble in solvents. Therefore, these smaller, multi-ring aromatic species are unlikely to be the source of visible PL observed for higher electron doses.

A fluorescence microscopy image of an example experiment is shown in Figure 3.3. We varied the dose and water vapor pressure during e-beam patterning of PS and measured the PL from the irradiated patterns under 405-nm laser excitation. For this set of experiments, the water vapor pressure ranged from 0.33 – 2 mbar, and the dose ranged from 1.8 – 45 mC cm^{-2}. The pressure along rows and the doses along the columns remain the same. We find that the emission color of the patterns can be tuned by varying the electron dose and water-vapor pressure.
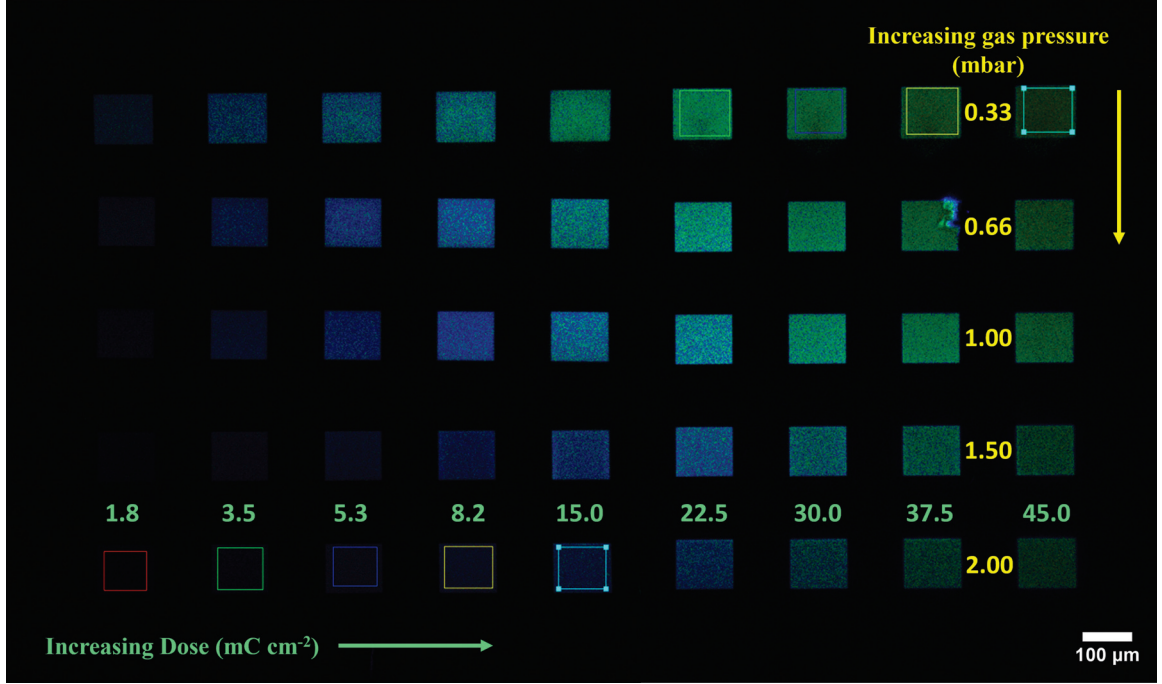
Figure 3.3: Fluorescence microscopy image of irradiated patterns on N-BK7 substrate. Water vapor pressure ranged from 0.33 – 2 mbar, and the dose ranged from 1.8 – 45 mC cm^{-2}. Exposure was done at 810 pA. Fluorescence intensity and wavelength depend on both dose and gas pressures.

3.3.1 PL enhancement by e-beam irradiation of PS on N-BK7 and soda lime glass substrate under water vapor: effect of electron dose and gas pressure

Experiments were conducted to understand the dependence of electron dose and gas pressure on PL intensity. 100 μm square patterns were exposed to a focused electron beam under high vacuum and under 1 mbar water vapor in the electron dose range of 1.8 – 15 mC cm^{-2}. PL spectra of the patterns exposed under high vacuum, shown in Figure 3.4a, indicate a red-shift in the emission wavelength and an increase in the PL intensity as the electron dose increases. These results are consistent with prior work on electron irradiated PS for the dose range considered [10, 102].

Exposure under water vapor led to interesting new findings. The emission wavelength and photon yield can be tuned by both dose and water vapor pressure, as shown in Figure 3.4b and Figure 3.5. The emission peak is found to blue-shift with increasing gas pressure. This could partly result from the reduction in the absorbed dose due to scattering in the gas. However, water vapor significantly *increased* the photon yield, with a maximum occurring at 1 mbar pressure. This result cannot be explained by simple electron scattering in the gas which would tend to reduce the dose with increasing pressure. The peak emission wavelength could be tuned in the 451 – 544 nm range by varying dose and water vapor pressure. The emission spectra from PS exposed under water vapor exhibit at least two peaks that are much sharper
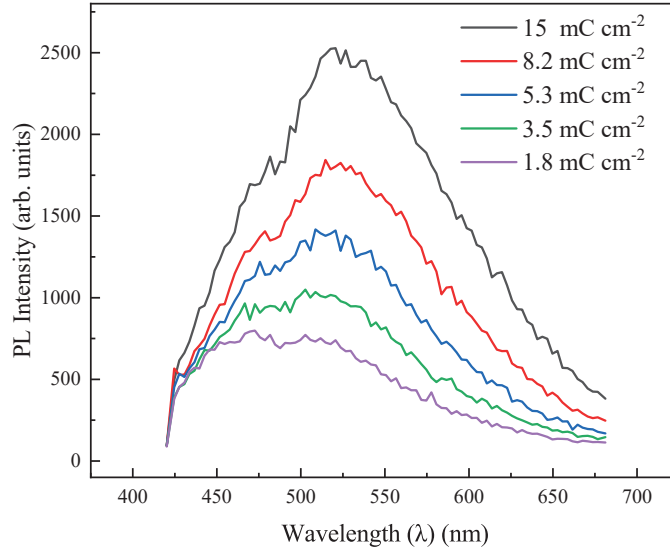
(a) Exposure under high vacuum
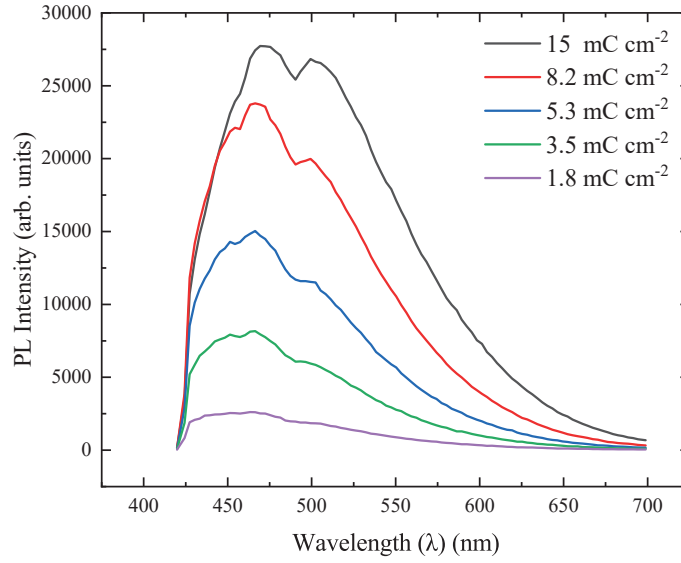
(b) Exposure under 1 mbar water vapor

Figure 3.4: PL intensity from PS films on N-BK7 substrates irradiated under (a) high vacuum and (b) 1 mbar water vapor using a beam current of 692 pA. The peak intensity is enhanced up to $10\times$ under water vapor and the peaks are significantly sharper.
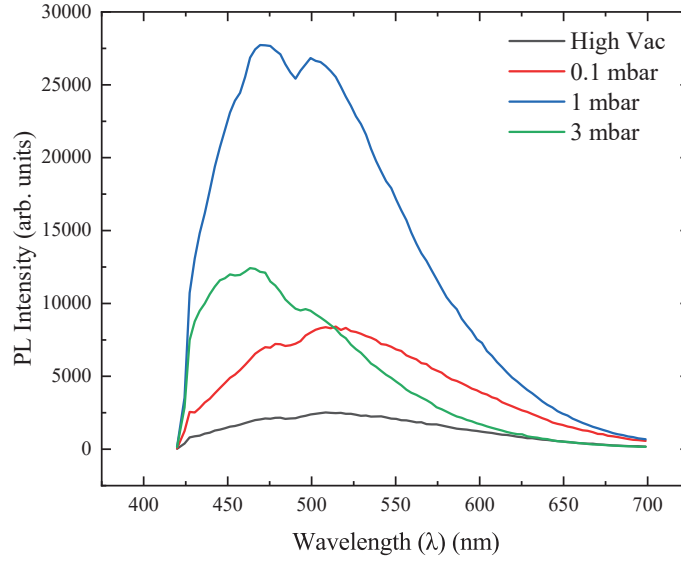
(a) wide range of pressures
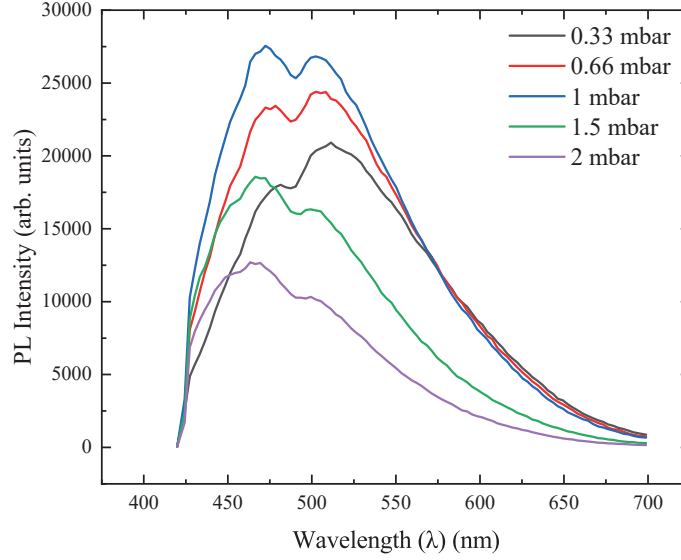
(b) narrow range of pressures

Figure 3.5: PL intensity as a function of water vapor pressure on N-BK7 substrate for 15 mC cm^{-2} electron dose carried out at 810 pA in (a) wide range of pressures and (b) narrow range of pressures.
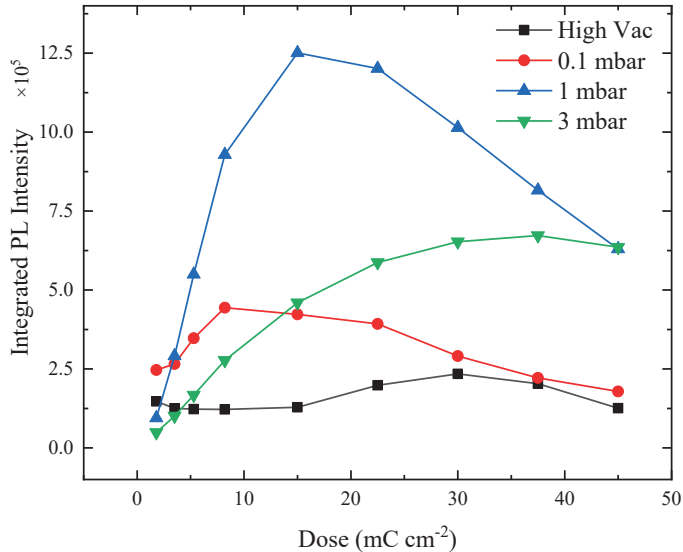
Figure 3.6: Integrated PL intensity as a function of electron dose on N-BK7 substrate carried out at a beam current of 810 pA.

than those observed for high-vacuum exposure. This suggests that the PL in visible region originates from several PAH species in the exposed patterns.

Figure 3.6 shows integrated PL intensity obtained under high vacuum and different water vapor pressures as a function of electron dose. The black line shows the integrated PL intensity under high vacuum and blue line is for 1 mbar water vapor exposure. Water vapor at 1 mbar increased the PL yield up to 10 times compared to the high vacuum exposure, a result which cannot be explained by simple electron scattering in the gas. Also, the dose at which the PL yield is maximum increases with gas pressure. The PL yield peaks around 8 mC cm^{-2} for 0.1 mbar exposure, where as it peaks at 37 mC cm^{-2} for 3 mbar exposure. For 1 mbar water vapor it peaks at 15 mC cm^{-2} exposure dose. With increasing electron dose the PL yield peaks and gradually decreases after a critical threshold electron dose is reached. Thus, water vapor at the right pressure dramatically increases PL yield and electron scattering in gas alone cannot explain the enhanced PL.

Dependence of PL on beam current on N-BK7 substrate:

Fluorophore synthesis could depend on electron-beam current through at least three mechanisms. First, if reactions involve the ambient gas, the gas could be depleted at higher beam currents similar to the effects seen in electron-beam induced deposition and etching[114]. Second, if the gas provides incomplete charge dissipation or screening, higher beam currents could lead to increased substrate charging. Finally, increased beam currents could increase the local temperature of the irradiated region. The fluorescence properties of CDs fabricated by pyrolysis [115], hydrothermal

39

[84, 85] and ultrasonic synthesis [81] have been found to be affected by the reaction temperature, where a decrease in the PL yield with increasing reaction temperature was observed. The decrease in PL yield with increasing reaction temperature was attributed to consumption of the molecular fluorophores by the carbon core. More recently Zhang et. al [116] demonstrated that there is an optimum reaction temperature where the PL yield reaches the threshold value. Below the optimal reaction temperature an increase in PL yield with increasing reaction temperature is observed, which was suggested to result from an increase in the number of fluorescent polymer chains. Beyond the optimal reaction temperature, the growth of the carbon core consumes the fluorescent polymer chains resulting in reduced PL yield.

To investigate the effect of beam current on the PL yield of the fluorophores synthesized by e-beam irradiation, patterns were exposed with increasing beam currents under 1 mbar water vapor pressure at an electron dose of 15 mC cm^{-2}. It is found that the PL intensity decreases with increasing beam current (Figure 3.7a), and this decrease is approximately linear over the range of currents considered (Figure 3.7b). The reduction of PL with beam current is consistent with the effect of temperature on PL yield of CDs synthesized by other methods [81, 84, 85, 115]. However, such a result could also be consistent with sufficient substrate charging to repel electrons and reduce the local dose and with depletion of the gas available for synthesis reactions. Thus, further investigation is required to isolate the underlying mechanism of beam-current dependence.

N-BK7 vs Soda lime glass substrate under 1 mbar water vapor:

To further understand the effect of water vapor on the PL intensity, we compared integrated PL intensity for patterns exposed under high vacuum and 1 mbar of water vapor pressure as a function of electron dose on N-BK7 and soda lime glass substrate as shown in Figure 3.8. One of the primary differences between N-BK7 and Soda lime glass lies in their chemical composition. The presence of mobile Na$^+$ ions in soda lime glass makes it effective for charge dissipation under high electric field. Glasses containing alkali ions upon focused electron irradiation undergo significant structural changes due to the formation of high electric field created by the trapped electrons inside the exposed volume making the migration of ions easier until the ions recombines with a free or trapped electrons [117, 118], thus, providing a charge dissipation pathway.

Another difference between the two substrates is that the thermally conductivity of N-BK7 is slightly hirer than that of soda lime glass, see Table 3.3. The reaction temperature of the exposed region on soda lime glass substrate is also expected to be slightly higher than on the N-BK7 substrate due to the lower thermal conductivity. The integrated PL intensity from irradiated PS on soda lime glass is found to be greater than on N-BK7 for exposure under high vacuum as well as under 1 mbar water vapor. This is consistent with dose reduction by greater charging of N-BK7. It could also be consistent with more efficient indicating that the increase in PL yield with increasing reaction temperature, below the optimum temperature, resulting from an overall increase in the number of fluorescent polymer chains [116].
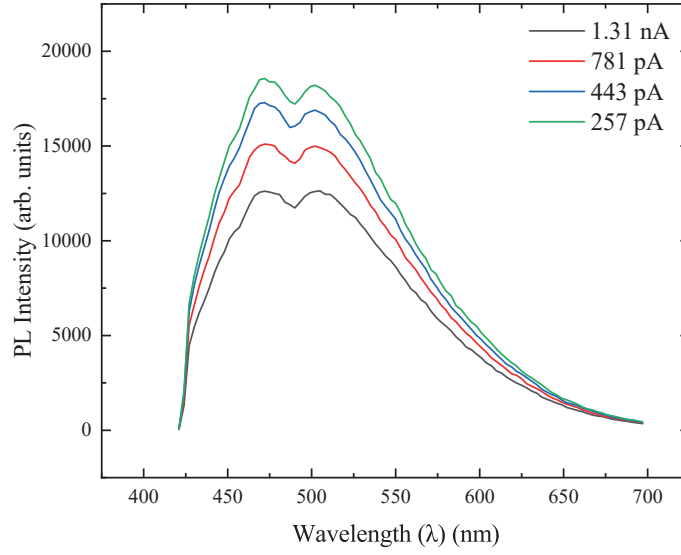
(a) PL Intensity vs beam current
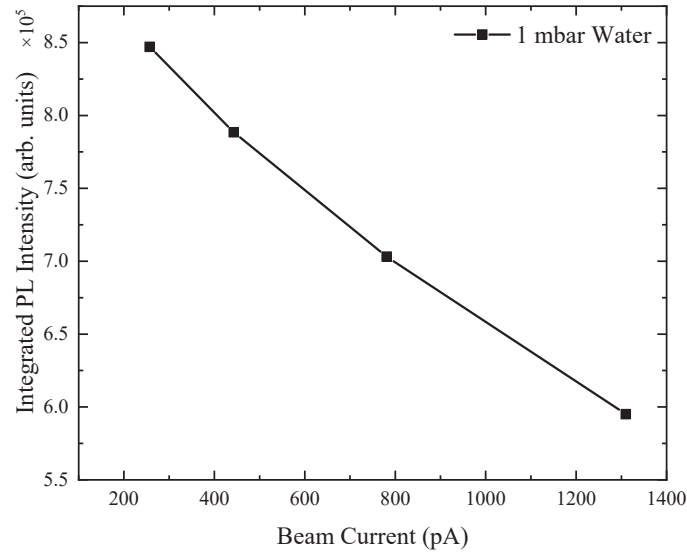
(b) Integrated PL Intensity vs beam current

Figure 3.7: Beam current dependence on PL under 1 mbar water vapor on N-BK7 substrate; (a) PL intensity vs beam current and (b) Integrated PL intensity vs beam current.
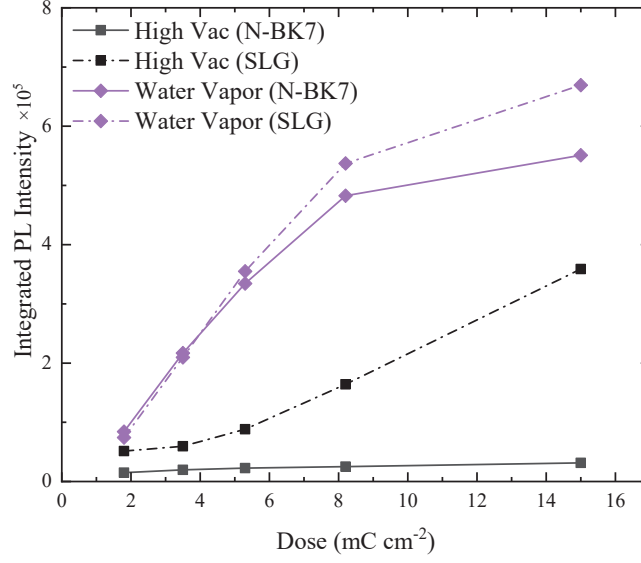
Figure 3.8: N-BK7 vs Soda lime glass: Integrated PL intensity as a function of exposure dose under 1 mbar water vapor. N-BK7 and soda lime glass substrate were exposed at a beam current of 764 pA and 950 pA respectively.

Thus, slight differences in the electrical and thermal properties of the substrates could lead to different reaction mechanisms for fluorophore formation resulting in different PL characteristics for exposures under otherwise identical conditions. We present a detailed analysis of PL enhancement on substrates with different electrical and thermal properties later in section 3.3.3.

Transmission electron microscopy for patterns exposed on soda lime glass substrates:

The nature of the CDs depends on the method of fabrication and varies with the precursor material and the conditions used during synthesis [81, 84, 116, 119–121]. High-resolution TEM image of e-beam irradiated PS (on soda lime glass substrate) under 1 mbar water vapor at an electron dose of 15 mC cm^{-2}, shown in Figure 3.9a, indicates that the irradiated film is amorphous in nature with no obvious lattices. In our experiments we found that even for the high vacuum exposure the irradiated films are amorphous in nature, Figure 3.9b, as opposed to the crystalline nature of CDs obtained by similar e-beam exposure of PS [102].
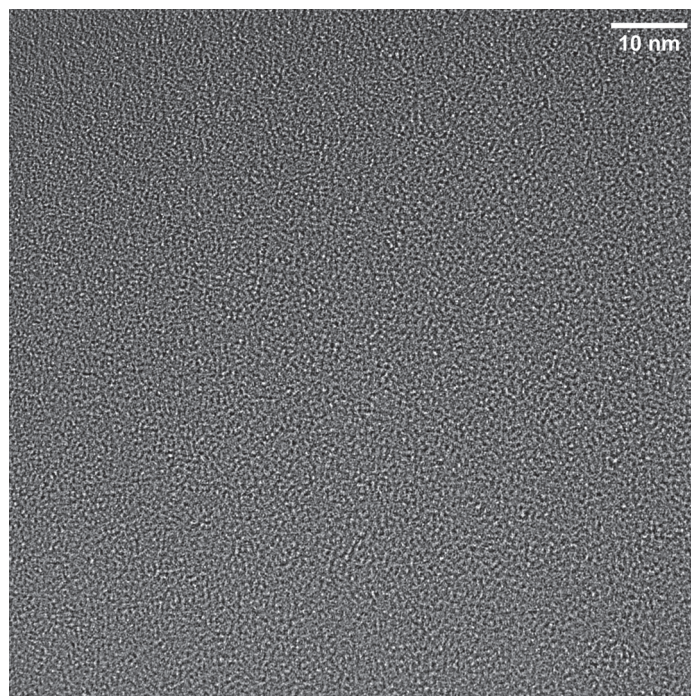
(a) 1 mbar water vapor
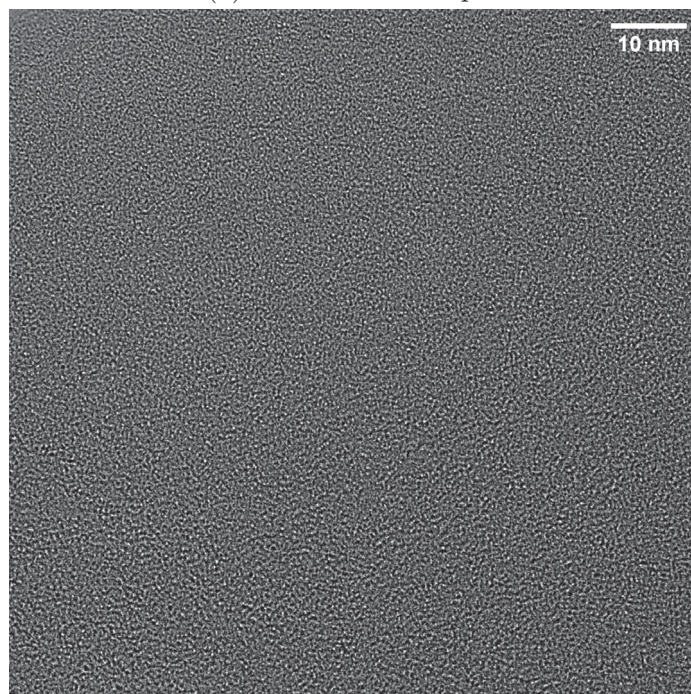
(b) High vacuum

Figure 3.9: TEM image of PS film on soda lime glass substrate irradiated at 15 mC cm^{-2} under (a) 1 mbar water vapor and (b) high vacuum.
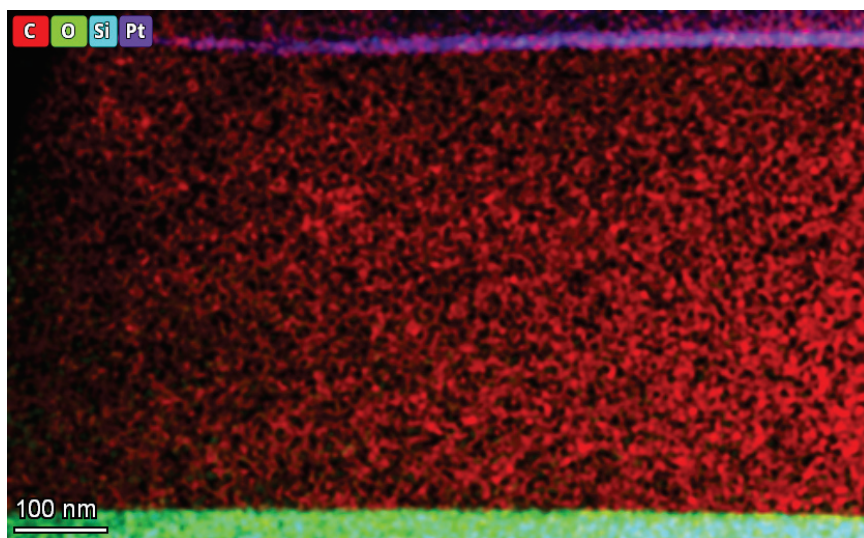
(a) 1 mbar water vapor
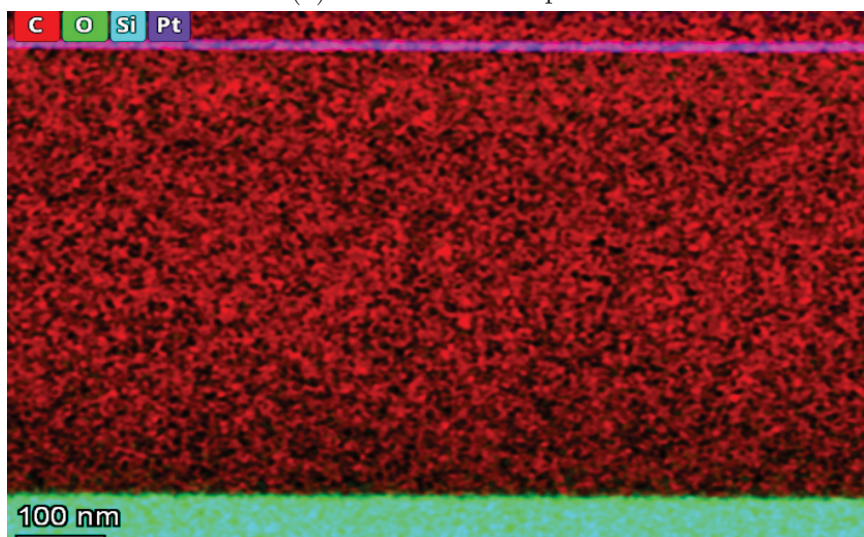
(b) High vacuum

Figure 3.10: Elemental mapping EDS image of PS film on soda lime glass substrate irradiated at 15 mC cm^{-2} under (a) 1 mbar water vapor and (b) high vacuum.

Energy dispersive X-ray Spectroscopy mapping for patterns exposed on soda lime glass substrates:

The nature of CDs' optical characteristics has been the subject of numerous investigations. While some studies have claimed that certain CD subsets gives rise to the optical characteristics [122], others have linked these to states originating from various functional groups [123]. One frequently made hypothesis is that the primary absorption properties are derived from core states [124–127]. The luminescent property of PS nanospheres formed by pulsed ultra violet laser radiation in air and vacuum, revealed the production of carbonyl groups on the surface of PS by photochemical oxidation is what causes the white luminescence [128].

Elemental mapping EDS image of PS film irradiated at 15 mC/cm^2 under 1 mbar water vapor (Figure 3.10a) and high vacuum (Figure 3.10b) revealed no signs of film oxidation. This means the origin of PL from the irradiated patterns likely results from the core states of the CD's or PAH's that are formed. The absence of carbonyl groups is also confirmed later in section 3.3.2 from the infrared spectrum obtained for the irradiated patterns using FTIR spectroscopy.

3.3.2 PL enhancement with different gases on N-BK7 and soda lime glass substrates:

In section 3.3.1, we demonstrated that the differences in the PL intensity on different substrates with or without the ambient gas in the chamber arises from the differences in the thermal and electrical properties of the substrate. In an environmental scanning electron microscope (ESEM) [43], the right selection of the ambient gas, gas pressure, working distance, and electron beam energy allows the imaging of electrically insulating material [129].

Here we expand our choice of ambient gas to include N_2, Ar, and He to understand how electron scattering in gases affects the PL intensity. Forward scattering of electrons in gases affects the amount of absorbed dose by the resist and the beam skirt radius from scattering in a gas can be approximated by [43]

$$R_s = 364 \left(\frac{Z}{E}\right) \left(\frac{P}{T}\right)^{1/2} L^{3/2}, \tag{3.1}$$

where a circle of radius R_S, in meters, encompasses 90% of the scattered electrons, Z is the effective atomic number of the scatterer, E is the primary electron energy in eV, P is the pressure in pascals, T is the temperature in Kelvin, and L is the gas path length in meters. Skirt radius, hence electron scattering in gas, is directly proportional to the effective atomic number of the scatterer gas when the gas pressure, gas path length, temperature and beam energy of the incident electrons are kept constant.

Table 3.1: Total gas scattering cross-section at 20 keV

Gas	Total gas scattering cross-section (cm^2)
Argon	2.14 x 10^{-17} [130]
Nitrogen	1.62 x 10^{-17} [131]
Water	1.18 x 10^{-17} [131]
Helium	1.73 x 10^{-18} [130]

Fluorescence microscopy image of of patterns irradiated on soda lime glass substrate under different gases is shown in Figure 3.11. Patterns were exposed at a beam current of 950 pA under 1 mbar of gas pressure. We see that the emission color of the patterns vary with electron dose and ambient gas, no significant scattering is observed for patterns exposed under gaseous environments; for patterns exposed under high vacuum conditions the formation of strong electrostatic fields at the sample surface resulting from substrate charging leads to poor shape fidelity [132]. Comparison of
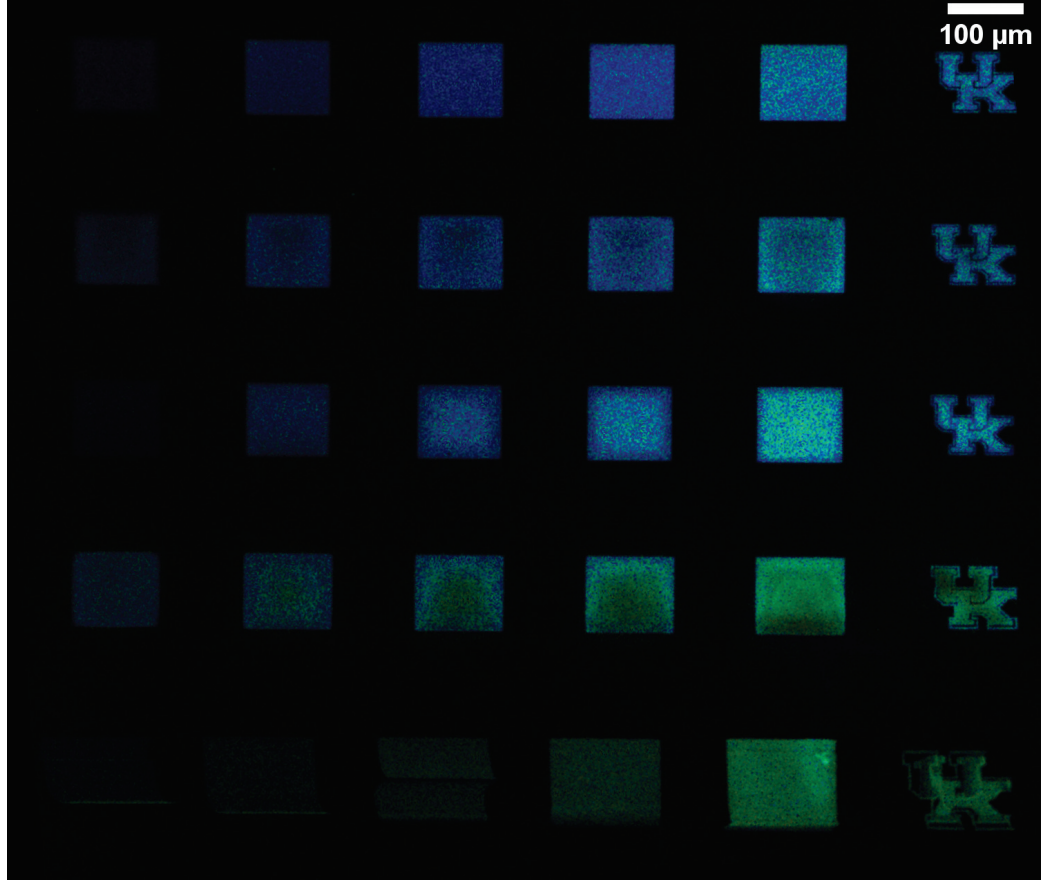
Figure 3.11: Fluorescence microscopy image of irradiated patterns on soda lime glass substrate. Dose ranged from $1.8 - 15 \, \mathrm{mC \, cm^{-2}}$. 100 μm square patterns were exposed, with a minimum of 100 μm spacing between each neighboring square, exposed at 950 pA under 1 mbar of gas pressure. The patterns from the top row to the bottom row were exposed under water, nitrogen, argon, helium and high vacuum respectively.

integrated PL intensity for patterns exposed under high vacuum and different gases at 1 mbar as a function of electron dose on N-BK7 (Figure 3.12a) and soda lime glass substrate (Figure 3.12b) revealed

- at low doses, gas with lowest scattering cross section yields the highest PL intensity; whereas at high doses the trend reverses, total gas scattering cross-section of the gases used in this investigation at 20 keV is listed in Table 3.1.
- integrated PL intensity peaks at lower doses for exposure under helium on N-BK7 substrate.
- on N-BK7 substrate exposure under water vapor is more conducive for fluorophore formation while on soda lime glass substrate argon is more effective.
- electron scattering in gas alone is not the dominant mechanism for enhanced PL as trend switches depending on dose and the choice of substrate.
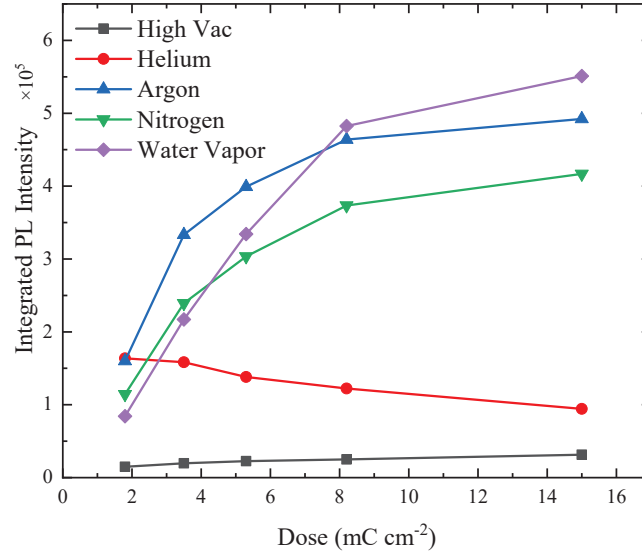
(a) N-BK7
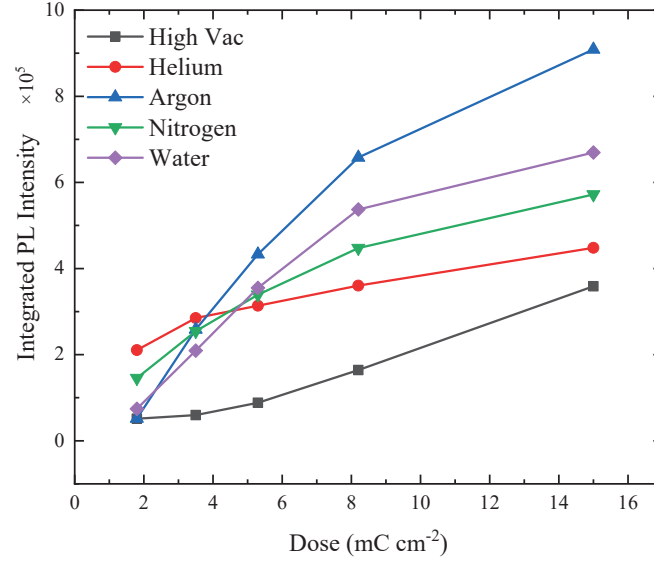
(b) Soda lime glass

Figure 3.12: Integrated PL intensity as a function of electron dose under 1 mbar gas pressure on (a) N-BK7 substrate at a beam current of 764 pA (b) soda lime glass substrate at a beam current of 950 pA.

47

It was also found that the emission peak blue-shifts with increasing gas pressure under all gases as observed for exposure under water vapor and the position of the emission peak is dictated by the gas pressure. The highest PL yield for exposures on N-BK7 and soda lime glass substrate was observed for exposure on soda lime glass substrate under argon gas. Therefore, more extensive characterization were performed only for patterns irradiated on soda lime glass substrate in order to understand how different gases affects the composition of the irradiated patterns.

Fourier-transform infrared spectroscopy for patterns exposed on soda lime glass substrates:

Important vibration bands in PS, listed in Table 2.3, lies at: 1453 which represents the —CH_2 bend of the carbon backbone; aromatic sp^2 carbon stretches lie at 1602; the symmetric and asymmetric C—H stretches on the backbone lies at 2851 and 2925; and the aromatic C—H stretches lies at 1492, 3029, 3061 and 3083.

Table 3.2: Important vibrational mode assignments for PS from FTIR reflection data

Wavenumber (cm^{-1})	Modes	
1453	—CH_2	bending
1492	C—H	aromatic stretches
1602	C=C	aromatic stretches
2851 and 2925	C—H	symmetric & asymmetric stretches (backbone)
3029, 3061 and 3083	C—H	aromatic stretches

Under high vacuum as well as for exposure under gases, Figure 3.13 and 3.14, the aromatic sp^2 carbon are preserved which suggests the PL observed upon irradiation originates from the aromaticity of the phenyl group. Under high vacuum the —CH_2 of the backbone, the C—H stretches of the backbone as well as the aromatic ring dissociate more rapidly compared to exposure under gases. We are preserving hydrogen both on the backbone and the aromatic ring as well as slowing down the breaking of C—C backbone under gases. Thus under gaseous environment the decay of aromatic and aliphatic C–H stretches is reduced compared to high vacuum exposure; in all cases (under high vacuum as well as gases), features associated with the phenyl rings are preserved, resulting in enhanced PL from PS irradiated under gases.
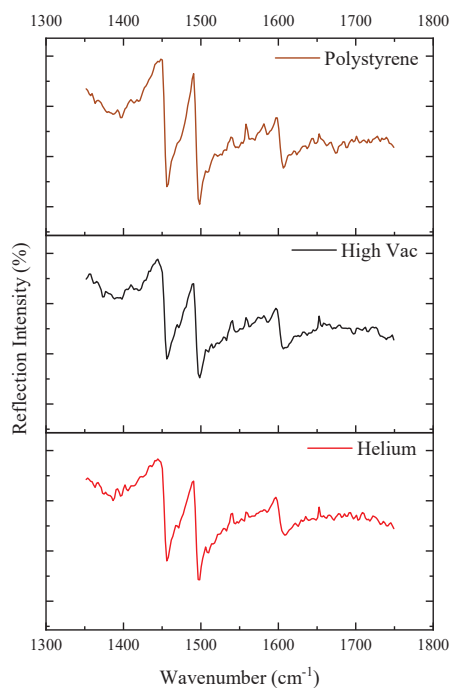
(a) PS, High Vacuum and Helium
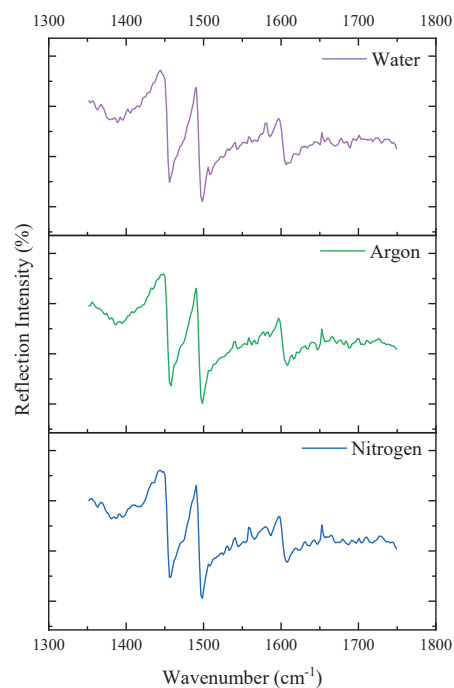
(b) Water, Argon and Nitrogen
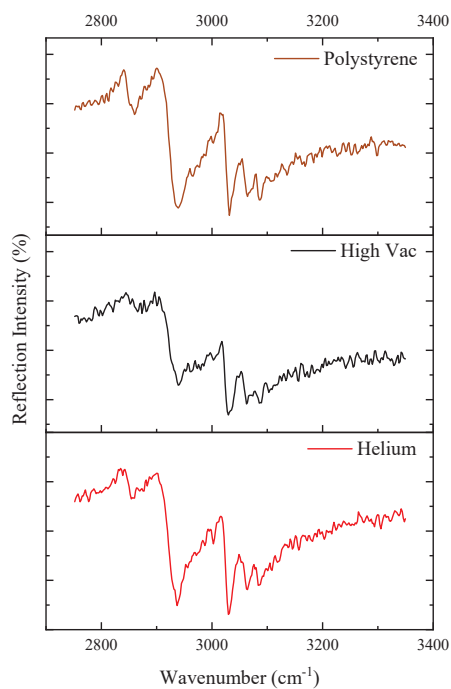
(c) PS, High Vacuum and Helium
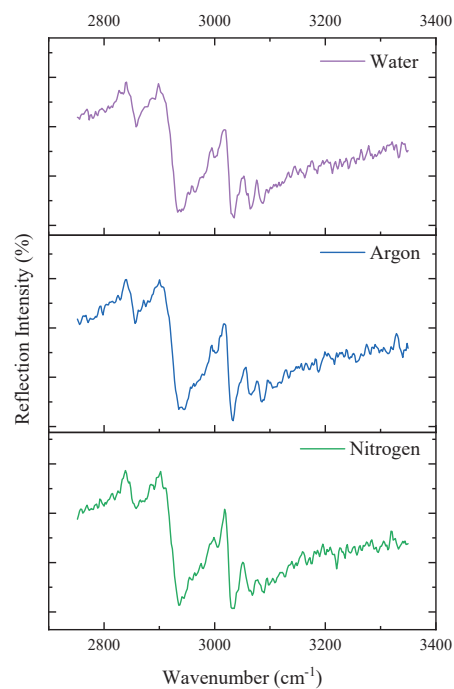
(d) Water, Argon and Nitrogen

Figure 3.13: Exposure under high vacuum and 1 mbar gas pressure at 1.8 mC cm^{-2}
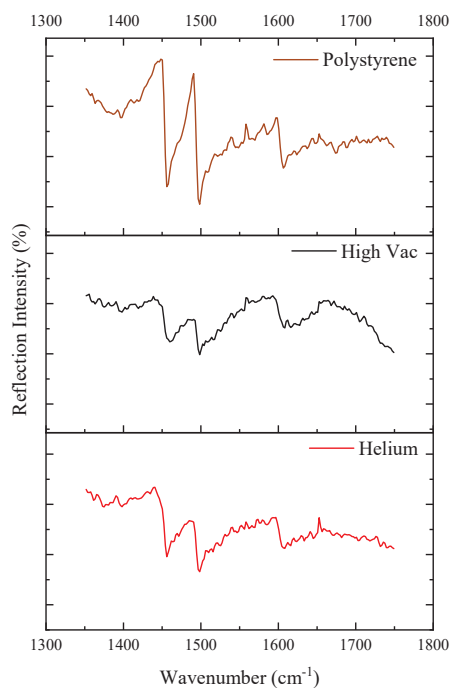
(a) PS, High Vacuum and Helium
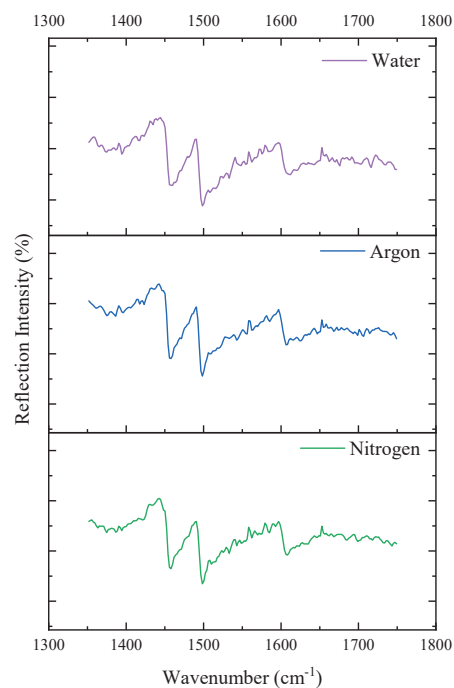
(b) Water, Argon and Nitrogen
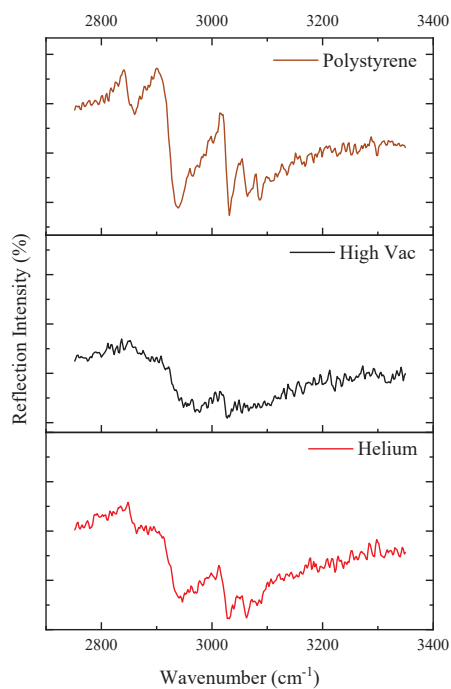
(c) PS, High Vacuum and Helium
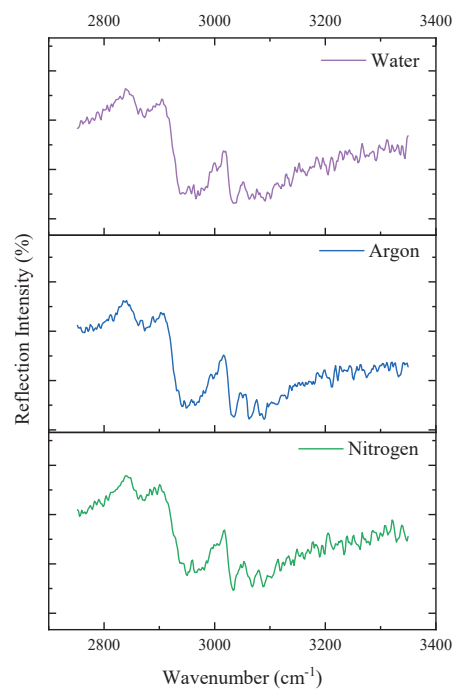
(d) Water, Argon and Nitrogen

Figure 3.14: Exposure under high vacuum and 1 mbar gas pressure at 15 mC cm^{-2}

3.3.3 PL enhancement on other insulating, conducting and semi-conducting substrates under ambient gases:

The presence of a benzene ring in a material's molecular structure also has a significant impact on its charging properties [133, 134]. The benzene rings in the sample acts as deep traps to stop the injection of extra charge into the bulk of the sample. High-energy electrons are attracted to the benzene rings, where their kinetic energy is lost energy by the resonance effect of the benzene rings. As a result, the chain scission of the polymer backbone is prevented. Benzene ring-containing polymers avoid an excessive buildup of electrons in their bulk, charge builds up over time and eventually saturates after a few minutes.

Silicon and ITO coated glass mitigates charge completely and the integrated PL intensity is proportional to the electron dose and is almost independent of the gas (Figure 3.15). Thus, on conductive substrates PL is not influenced by the presence of a gas. Photon-yield on conductive substrates is significantly smaller than that yield from insulating substrates. On sapphire the integrated PL intensity is factor of 2 or more higher than on Si (sapphire and silicon have similar thermal conductivity, Table 3.3 lists the thermal conductivity of substrates at room temperature), and PL shows a gas dependence. Integrated PL intensity varies inversely with the thermal conductivity of substrates; soda lime glass being least thermally conductive yields the highest PL yield.

Table 3.3: Thermal conductivity of substrates at room temperature

Substrate	Thermal conductivity ($Wm^{-1}K^{-1}$)
Silicon	69-157
ITO	4
Soda lime glass	0.7
N-BK7	1.11
Fused Silica	1.38
Sapphire	40

On electrically insulating substrates the PL is influenced by the presence of a gas (Figure 3.16), this could possibly result from the differences in the charge dissipation with different gases. The degree of charge dissipation depends on the ionization coefficient of gases as well as the experimental conditions used such as working distance and the gas pressure. With fixed working distance and gas pressure the degree of charge dissipation is a function of ionization coefficient of gases. Gases mitigate charging to different degrees and does not eliminate it completely and contribute to the enhancement in PL. Thus, on substrates with similar thermal conductivity, substrate charging affects the process of fluorophores formation and significantly influences the PL.

Gas influences the charging of substrates affecting the formation of fluorophores resulting in an enhanced integrated PL intensity on soda lime glass where the 5x enhancement compared to Si is seen. Highest integrated PL intensity is observed on soda lime glass substrate, which is least thermally conductive of the substrates used
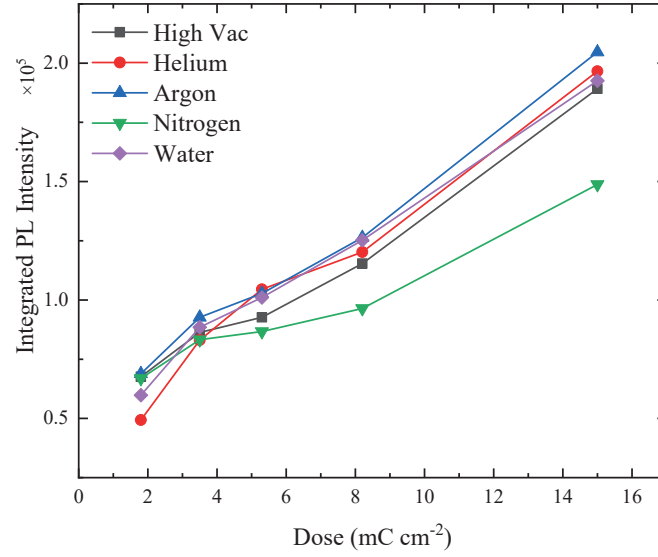
(a) Silicon
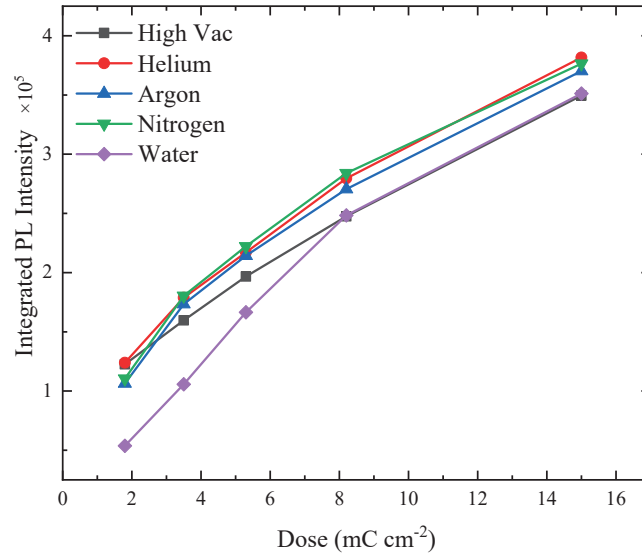
(b) ITO coated soda lime glass

Figure 3.15: Integrated PL intensity on conducting substrates as a function of electron dose under 1 mbar gas pressure exposed at a beam current of 950 pA on (a) Silicon and (b) ITO coated soda lime glass.
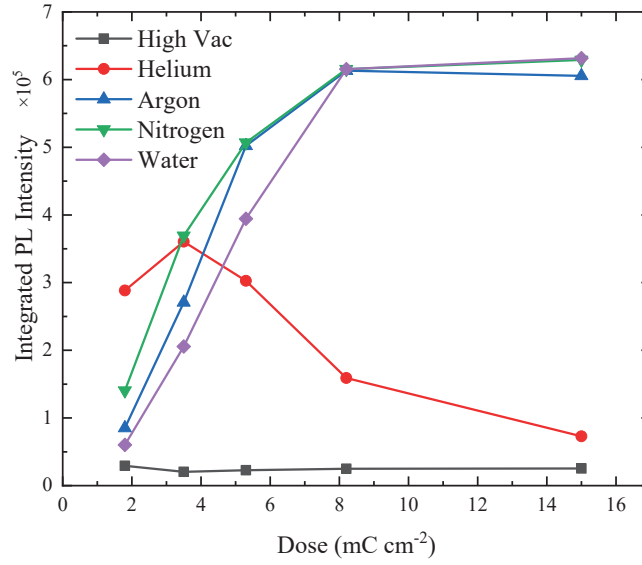
(a) Fused Silica
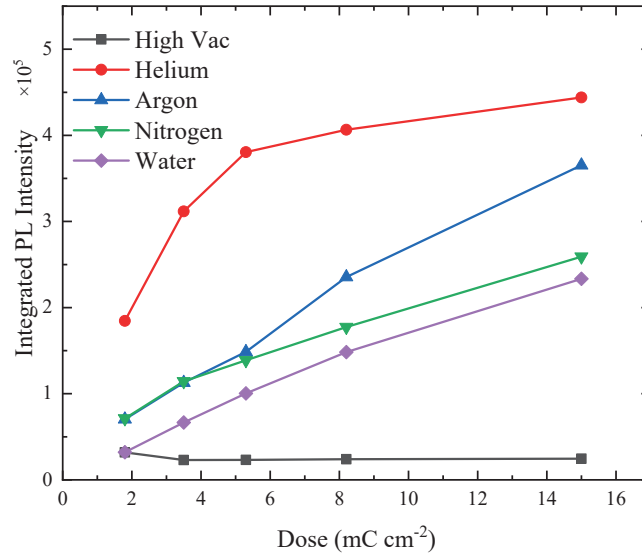
(b) Sapphire

Figure 3.16: Integrated PL intensity on insulating substrates as a function of electron dose under 1 mbar gas pressure exposed at a beam current of 950 pA on (a) Fused Silica and (b) Sapphire.

Table 3.4: Thermal conductivity of gases at room temperature

Gas	Thermal conductivity ($Wm^{-1}K^{-1}$)
Argon	17.7 x 10^{-3} [135]
Nitrogen	25.9 x 10^{-3} [135]
Water	18.6 x 10^{-3} [135]
Helium	155.7 x 10^{-3} [135]

Table 3.5: Gross ionization cross-section at 20 keV

Gas	Gross ionization cross-section (cm^2)
Argon	7.8 x 10^{-18} [136]
Nitrogen	7.0 x 10^{-18} [136]
Water	5.4 x 10^{-18} [137]
Helium	9.5 x 10^{-19} [136]

in this study. As we have seen earlier electron scattering in gas does not significantly affect the PL and slight differences in thermal conductivity's of substrates results in different PL characteristics as described in Section 3.3.1, the difference in integrated PL intensity on soda lime glass and Si can be attributed to the differences in thermal conductivity's of substrates as well as the gas. Helium is much more thermally conductive, and we see a lower integrated PL intensity on soda lime glass under helium. Argon and water have similar thermal conductivity's, see Table 3.4 where the thermal conductivity of gases at room temperature is tabulated, but their scattering cross-section and ionization cross-section (Table 3.5 provides the ionization cross-section of gases at 20 keV) are not similar which results in the differences in charging leading to the differences in PL. If we assume that all gases are mitigating charge well, then the PL increases as thermal conductivity of gas decreases. Thus on insulating substrates, substrate charging, thermal conductivity of substrates as well as the gases influences the process of fluorophore formation, significantly influencing the PL.

3.4 Summary and conclusions

We provide a novel way to tune the emission wavelength and enhance the fluorescence intensity simultaneously. PL intensity of the patterns exposed under high vacuum, indicates a red-shift in the emission wavelength and an increase in the PL intensity as the electron dose is increased, which is consistent with prior work on electron irradiated PS. The novelty of this work is to tune the emission wavelength and photon yield simultaneously by varying both dose and gas pressure. For exposure under gaseous environment, with increasing electron dose the PL yield peaks and gradually decreases after a critical threshold electron dose is reached.

Water vapor significantly increased the photon yield on N-BK7 substrate with a maximum occurring at 1 mbar pressure, a result which cannot be explained by simple electron scattering in the gas; the emission peak is found to blue-shift with increasing gas pressure. Peak emission wavelength can be tuned over a wide wavelength range by varying gas pressure. Comparison of integrated PL intensity on N-BK7 and soda lime glass substrate revealed that slight differences in electrical and thermal properties of substrates leads to different PL characteristics for exposures under otherwise identical conditions.

On N-BK7 substrate exposure under water vapor is more conducive for fluorophore formation while on soda lime glass substrate argon is more effective. For exposure on soda lime glass substrate under water vapor, high-resolution transmission electron microscope image revealed e-beam irradiated PS are amorphous in nature and elemental mapping EDS revealed no signs of oxidation of the film. FTIR spectroscopy revealed that under gaseous environment the decay of aromatic and aliphatic C–H stretches is reduced compared to the high vacuum exposure; in all cases, features associated with the phenyl rings are preserved.

Up to 18x enhancement in fluorescence yield can be achieved on Sapphire substrate for exposure under helium. Overall, the highest PL yield is observed on soda lime glass substrate under argon environment. Photon-yield on conductive substrates is significantly smaller than that yield from insulating substrates. Substrate charging, thermal conductivity of substrates as well as the gases influences the process of fluorophore formation, significantly influencing the PL. The differences in the PL characteristics could arise from factors such as higher thermal conductivity of or fluorescence quenching by conductive substrates.

While understanding the possible physical mechanisms lead to the following conclusions that

- Electron scattering in gas is not responsible for the enhanced PL.
- Insulating substrates exhibits gas dependent PL.
- PL is further affected by the thermal conductivity of the gas.

Thus, localized e-beam synthesis of fluorophores in PS can be controlled by both dose and by ambient gas pressure. This technique could enable new approaches to photonics where fluorophores with tunable emission properties can be locally introduced by e-beam patterning.

Chapter 4 Enhanced contrast and high-resolution patterning of PMMA on insulating substrates under ambient gases

4.1 Introduction

Lithography is the process of transferring a pattern to a material from either a physical template or a digital design. Electron beam lithography (e-beam lithography or EBL) which first emerged in the late 1960s, uses nanometer sized focused electron beam for pattern transfer by irradiating substrates that have been coated with organic/ inorganic thin film resist that is sensitive to electrons. The solubility of the resist changes upon exposure to the electron beam, allowing for the selective removal of either the exposed region (positive-tone resist) or unexposed region (negative-tone resist) of the resist in a suitable developer solution. The pattern is finally transferred either by etching or lift-off.

The primary advantage of electron beam lithography over other lithographic techniques is that it provides (i) maskless patterning process; (ii) high resolution transfer of complex patterns (with dimensions down to a few nanometers and not diffraction limited); and (iii) highly automated and precisely controlled operation. Nanometer feature sizes can be fabricated using e-beam lithography due to its short wavelength. Electron beam lithography is a low throughput process which limits it's usage to photomask fabrication in industry, small volume production of semiconductor devices, and research purposes. However, there are few alternatives for defining structures at the few nm length scale (Figure 4.1).

A number of different applications, including micromechanical fabrication, fabrication of semiconductor devices, direct write organic lasers, diffractive optic elements such as photonic–crystal enhanced lasers, sub-wavelength waveguides, split-ring resonators etc., requires electrically insulating substrates. However, using electron-beam lithography to pattern on electrically insulating substrates is often challenging because of charging effects. Considering the high beam energies employed (typically 30-100 kV) during electron beam lithography, most of the electrons are deposited in the substrate. When the substrate is electrically insulating strong electrostatic fields are created at the sample surface which leads to deflection of the incident electron beam resulting in poor shape fidelity, severe pattern placement error [139], and even dielectric breakdown of the resist.

Several methods have been developed to mitigate substrate charging while performing electron beam lithography exposure process on insulating substrates. Current existing methods makes use of:
1. Critical Energy Electron Beam Lithography (CE-EBL) [140]
2. Conductive polymers [141]
3. Deposition of thin metal layers either on top or underneath the resist [142, 143]
4. Variable pressure electron beam lithography (VP-eBL) [7]

CE-EBL takes advantage of the crossover energies to minimize pattern distortion from surface charging. However, there are several limitations for CE-EBL [140]:
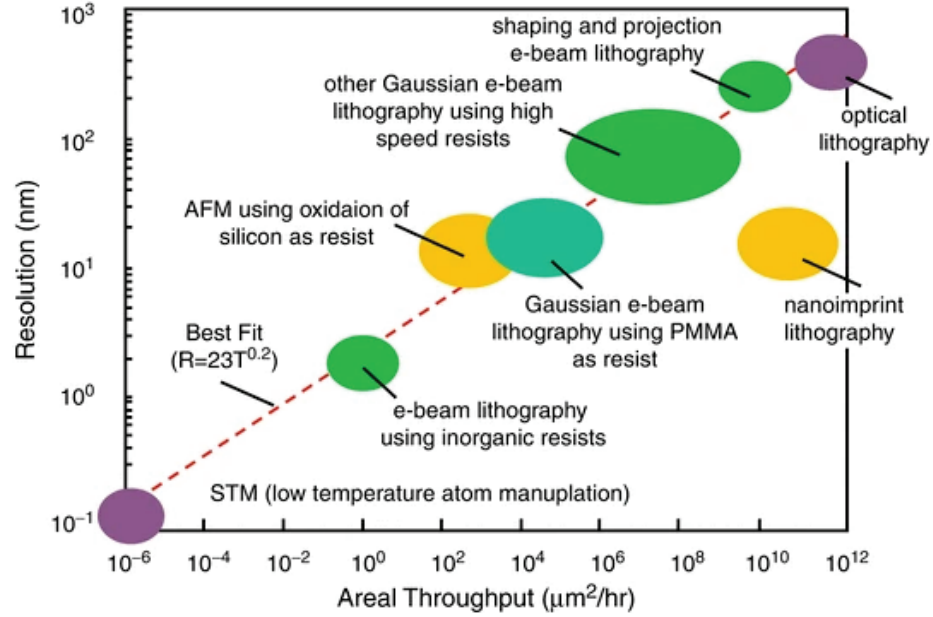
Figure 4.1: Resolution of different lithographic techniques as a function of throughput [138], figure reproduced from Pala N and Karabiyik M. Electron Beam Lithography (EBL). en. Encyclopedia of Nanotechnology. Ed. by Bhushan B. Dordrecht: Springer Netherlands, 2012 :718–40. Reproduced with permission from Springer Nature.

(i) the resist thickness cannot be more than the penetration depth of the electron beam and (ii) the resist's crossover voltage depends on the substrate and the resist's thickness as well as material properties. Owing to these limitations CE-EBL may not be practical to reduce charging effects. Conductive polymers used for charge dissipation also may not be a viable alternative as conducting polymers are prone to a shorter shelf life and more likely to experience pH drift, with conductivity decreasing when the pH moves outside of the optimum range, increasing the risk of contamination upon precipitation of the polymers [144].

The most common method used for charge dissipation purpose in electron beam lithography involves coating thin metal layers either on top of or underneath of the electron-beam resist [142, 143]. Cumming et al. coated PMMA plate with a 30 nm metal film prior to exposure to find that the charging problem was dependent on beam current and independent of the dose, which places an upper limit on the beam current that can be used in any desired range of doses, hence limiting the write speed [142]. Characterization of contrast and resolution of a metal coated (aluminum, chromium, or copper) electron-beam resist revealed that lower atomic number metal coatings altered clearing dose and contrast but did not degrade resolution at the 40 nm scale [143].

However, the drawbacks of using coatings of thin metal layers to reduce charging is that it requires film deposition prior to exposure and film removal prior to development which can extend the process time, thus, severely impacting the throughput. Another important aspect that must be considered is the method used to deposit

the metal layer. When compared to a thermally deposited aluminum layer, electron beam evaporation technique results in edge roughness that is more than three times higher and also increases the sensitivity of the resist to small dose variations [145]. X-rays and electrons generated in the electron beam evaporator while deposition can also expose the resist [146].

Finally, Variable-pressure electron-beam lithography (VP-EBL) which employs an ambient gas at subatmospheric pressures to reduce charging during electron-beam lithography on electrically insulating substrates has been found to be an efficient method which doesn't impact the throughput of the process. Paul & Klimkiewicz [147] introduced the idea of employing an environmental scanning electron microscope (ESEM) as a tool for electron beam lithography. Previous works demonstrated that low pressure electron beam lithography can eliminate distortion and improve resolution when patterning PMMA on conducting [148] and insulating substrates [7]; there is a decrease in linewidth variability as chamber pressure increases. When using low-pressure electron beam lithography, there exists a trade-off between resist charging and decreasing linewidth dimensions [148]. However, no data is available on how the ambient gas affects the contrast of the process and the resolution of highly dense patterns.

In this work, VP-EBL was conducted to study the effect of ambient gases on contrast, clearing dose and resolution of PMMA on insulating substrates. To our knowledge, these are the first studies of molecules other than water for EBL in gaseous environments. From contrast curves of PMMA on fused silica exposed under 1 mbar of helium, water, nitrogen and argon yielded contrast values of 13.6, 8.6, 7.7 and 9.7, respectively. Once charging is mitigated effectively by an ambient gas, the contrast of the process on insulating substrates is significantly higher than on silicon. The clearing dose increases with the gases' molecular weight and proton number, consistent with the increase in scattering cross-section. resolution testing indicated that despite the lower clearing dose, helium still exhibited the best resolution with 25-nm half-pitch dense lines and spaces clearly resolved on soda lime glass. To our knowledge, this is the highest resolution demonstrated to date for EBL in a gaseous environment.

4.2 Experimental details

4.2.1 PMMA spin coating

PMMA (950 K molecular weight, MicroChem Corp.) was diluted using anisole (MicroChem Corp.) to make 4 wt. % and 1 wt. % solution for contrast and resolution experiments respectively. The PMMA solution thus prepared was spin coated onto a n-type $\langle 100 \rangle$ silicon, fused silica and soda lime glass substrate at 500 rpm for 5 s to give a uniform layer and then spun at 4000 rpm for 1 min to set the desired thickness. Next, the spin-coated substrates were heated on a hot plate at 180°C for 120 s to remove any residual solvent. Ellipsometry (M-2000, J. A. Woollam Co. Inc.) was used to measure the final film thickness of the spin-coated PMMA film. The final resist thickness for the contrast and resolution experiments were measured to be 284 nm and 39 nm, respectively.

4.2.2 Variable-pressure electron-beam lithography process

An ELPHY Plus pattern generator (Raith GmbH) coupled with a FEI environmental scanning electron microscope (Quantum FEG 250) with a fast beam blanker was used for the VP-EBL process. An analytical working distance of 10 mm and a beam energy of 30 keV were used for all lithographic processes. A faraday cup and a pico-ammeter (Keathley 6487) were used for the beam current measurements under high vacuum conditions prior to each ithographic exposure. Gold nanoparticles deposited onto PMMA were used for focusing and as marker during patterning.

First set of experiments relate to obtaining contrast curves of the resit exposed under different ambient gases on different substrates. For the contrast experiments, 20×100 μm^2 rectangular structures were exposed under high vacuum and 1 mbar of ambient gases (water vapor, helium, nitrogen and argon) with areal exposure dose ranging from $10 - 300$ μC cm^{-2} with a step size of 12.8 nm and a beam current of 89 pA. An electron-beam energy of 30 keV was chosen to reduce beam scattering in both water vapor and the resist, as well as to distribute backscattering to the largest range possible [37]. Each adjacent rectangle was given a 20 μm spacing to minimize proximity effects from backscattering. To minimize any variations between the exposures, patterns exposed under high vacuum and gases were placed on the same sample 400 μm apart from each other. The exposed film was developed in 1:3 MiBK: IPA for 60 s at room temperature followed by 30 s IPA rinse. Thickness measurements of the resulting resist surface after development were conducted using a Dektak 6 M (Veeco, Inc.) surface profiler.

Second set of experiments was related to finding the resolution limits for exposure under gaseous environment. For the resolution experiments, "nested-L" structures, 10, 15, 20, 25, 50, 100 and 200 nm half-pitch were exposed under high vacuum and 1 mbar of ambient gases (water vapor, helium, nitrogen and argon) with line dose ranging from $50 - 700$ pC cm^{-1} in the increments of 50 pC cm^{-1} with a step size of 3.2 nm and a beam current of 68 pA. Each adjacent "nested-L" pattern was given a 4 μm spacing. The exposed film was developed in 4:1 ethanol: water for 45 s at 3 °C followed by 10 s IPA rinse, cold development has been demonstrated to provide improved resolution with reduced line edge roughness [149]. After exposure and development the samples were sputter coated with 5 nm of gold. An FEI environmental scanning electron microscope (Quantum FEG 250) and imageJ were used for the line-width measurements.

4.3 Results and discussions

4.3.1 Effect of ambient gases on contrast and sensitivity of PMMA on insulating substrates

Sensitivity

Sensitivity is the inherent property of the resist and is defined as the minimum dose at which the exposed resist is soluble in the developer solution. Sensitivity, S, (referred here as dose to clear (D_C)) is often expressed in micro coulombs per square centimeter as:

$$S = \frac{e.N_e}{A}(\mu C/cm^2) \tag{4.1}$$

where e is the electron charge, N_e is the number of electrons and A is the area of the resist exposed. Resist sensitivity depends on a large number of parameters including: resist material, resist thickness, developer, development time and temperature as well as the beam energy used for the exposure. These parameters are manipulated to maximize yield and reproducibility by achieving high resolution and high throughput result with large process window. High sensitivity of a resist is critical for a number of reasons (i) during e-beam exposure most of the deposited energy is converted to heat, causing temperature rise in the resist. Localized heating can lead to dynamic wafer distortion causing significant overlay error [150] and pattern distortion [151]; (ii) the resolution, which is linked to the beam current [152], can be improved by reducing the beam current for a given throughput. Thus, high sensitivity resists are needed to increase the throughput.

Contrast

The resist contrast, which measures how non-linearly the development process responds to the chemical contrast created in the material after exposure, is crucial in figuring out the minimum image modulation that can be effectively transformed into a developed resist image. Contrast indicates how abruptly the thickness changes with dose, which affects resolution as well [138]. Combining contrast and sensitivity, the contrast curve of a resist can be obtained by plotting the residual resist thickness as a function of increasing electron dose (Figure 4.2) Higher contrast values result in steeper sidewall angles. Reducing the polydispersivity of the starting polymer enhances both the contrast and sensitivity. Higher contrast value is essential for conventional IC manufacture, however, low contrast values are desired for producing quasi-3D structures such as diffractive optics. [153].

The nature of the development process after the exposure determines the contrast value and is dependent on a number of elements including temperature, development time, developer solvents, and resist properties. Significant enhancement in contrast, at the cost of reduced sensitivity, is obtained for thick PMMA films developed at lower temperatures [154]. Where as, for thin resist films decreasing the development temperature has no discernible impact on contrast while reducing the sensitivity
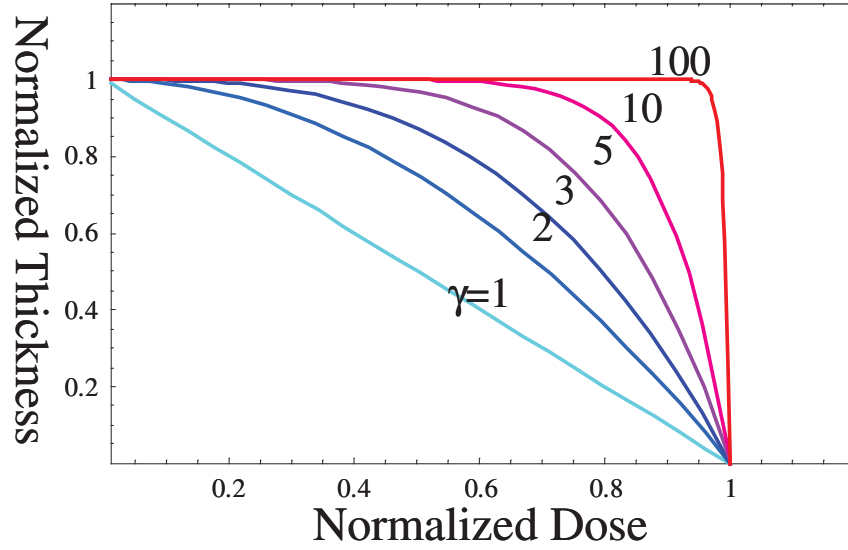
Figure 4.2: Normalized resist thickness versus normalized dose for a positive-tone resist with different dissolution rates [153]. Figure reproduced from Liddle JA, Gallatin GM, and Ocola LE. Resist requirements and limitations for nanoscale electron-beam patterning. MRS Online Proceedings Library (OPL) 2002; 739:H1–5. Reproduced with permission from Springer Nature.

Table 4.1: Contrast (γ) and dose to clear (D_C in μC cm^{-2}) of PMMA on silicon substrate under high vacuum and 1 mbar pressure of ambient gases.

	High vacuum	He	H$_2$O	N$_2$	Ar
Contrast (γ)	10.3±0.5	10.7±0.7	12.6±0.5	8.4±0.4	8.4±0.5
Dose to clear (D_C)	138±1	138±1	134±0	147±1	155±1

Table 4.2: Contrast (γ) and dose to clear (D_C in μC cm^{-2}) of PMMA on fused silica substrate under high vacuum and 1 mbar pressure of ambient gases.

	High vacuum	He	H$_2$O	N$_2$	Ar
Contrast (γ)	–	13.6±1.4	8.6±0.9	7.7±0.4	9.7±0.3
Dose to clear (D_C)	–	104±1	147±2	141±1	148±0

Table 4.3: Contrast (γ) and dose to clear (D_C in μC cm^{-2}) of PMMA on soda lime glass substrate under high vacuum and 1 mbar pressure of ambient gases.

	High vacuum	He	H$_2$O	N$_2$	Ar
Contrast (γ)	9.5±0.6	11.7±0.8	9.4±0.3	8.8±0.6	8.8±0.3
Dose to clear (D_C)	114±1	117±1	122±0	128±1	133±0

of PMMA to the developer[155]. The dose to clear is also greatly influenced by the choice of developer solvents and rinse solution. For PMMA, ethanol/water at a 4:1 volume ratio offers a non-toxic viable alternative with superior contrast and resolution over other developers [42]. Other method to improve the resist contrast uses ultrasonically-assisted development, 3:7 water:IPA composition was found to be optimum for sensitivity and contrast [156]. 200 keV EBL exposures lead to higher contrast than 30 keV exposures [30].

The results from the first set of experiments that relate to the contrast and sensitivity measurements of PMMA exposed under high vacuum conditions and gaseous environments, the experimental data for contrast curves on different substrates is presented in Figure 4.3; and the fitted contrast and dose to clear values are presented in Table 4.1, 4.2 and 4.3. The fitted contrast curves for exposure of PMMA on silicon, fused silica and soda lime glass are shown in Figure 4.4, 4.5 and 4.6 respectively. Data points used for the fit are indicated by a ∘, while data points excluded from the fit are indicated by an ×. Dose to clear, D_C, and contrast for each data set are shown in the inset. Uncertainties represent the standard error of the fitted parameter. The patterns on fused silica exposed under vacuum conditions were quite distorted to infer any meaningful data for contrast value, hence, have not been presented here.

The dose to clear and contrast value of PMMA on silicon for exposure under vacuum conditions in Table 4.1 is higher than that presented in Chapter 2 Table 2.2. The differences in the dose to clear and contrast values for exposure in otherwise identical conditions is because of the differences in the thickness of PMMA and the development temperature. The thickness of PMMA on silicon presented in Chapter 2 was 171 nm vs 284 nm thick PMMA for the data presented here in Chapter 4. Despite the differences the water vapor yields similar or higher contrast values on soda lime glass and silicon substrates without a significant change in the dose to clear when compared to exposure under vacuum conditions, there results are consistent with our previous work.

On insulating substrates exposure under gaseous environment yields improved or degraded contrast values compared to vacuum exposure. Especially, exposure under nitrogen and argon results in comparable or degraded contrast values with an increase in the clearing dose compared to vacuum exposure irrespective of the substrate. The clearing dose was found to increase with the gases' molecular weight and proton number, consistent with the increase in scattering cross-section. The dose to clear and the contrast value for exposure under helium environment of PMMA on silicon is similar to that of the vacuum exposures. However, the contrast value for exposure under helium of PMMA on fused silica and soda lime glass is significantly higher, without a significant impact on the dose to clear.

The use of VP-EBL to pattern under gaseous environment involves the interactions of incident electrons in the gas and the subsequent formation of positive ion by-products that makes many interdependent parameters impacting the exposure process in several ways (i) scattering of electrons in the gas could lead to a reduced effective absorbed dose in the resist, and (ii) the incident primary electrons slows down under the applied detector voltage, resulting in a decreased landing energy which affects the beam penetration as well as the interaction volume, electron emis-

sion, and charging [157]. Forward scattering in gas significantly affects the exposure process, Danilatos [43] showed that the beam skirt radius from plural scattering in a gas can be approximated by

$$R_s = 364 \left(\frac{Z}{E}\right) \left(\frac{P}{T}\right)^{1/2} L^{3/2},$$
(4.2)

where a circle of radius R_s, in meters, encompasses 90% of the scattered electrons, Z is the effective atomic number of the scatterer, E is the primary electron energy in eV, P is the pressure in pascals, T is the temperature in Kelvin, and L is the gas path length in meters. The effective atomic number for helium, water, nitrogen and argon are 2, 7.42, 7 and 18 [43], respectively. For the conditions considered here, the skirt radius for helium, water, nitrogen and argon are 14 μm, 52 μm, 49 μm and 126 μm, respectively.

In an environmental SEM, secondary electrons emitted from the sample are accelerated toward a positively biased detector and multiplied as they ionize the ambient gas. The secondary electron cascade is collected by the detector, and the resulting ions are accelerated toward the grounded or negatively charged substrate. As discussed by Thiel, the multiplication factor, g, and thus the approximate number of ions per secondary electron, is given by

$$g = e^{\alpha d}$$
(4.3)

where α is the first Townsend ionization coefficient and d is the detector-sample distance. The ionization coefficient is given by

$$\alpha = A \cdot P e^{-B \cdot P \cdot d \cdot V_0}$$
(4.4)

where A and B depend on the gas, and P is the pressure.

Table 4.4: Values of A and B in first Townsend ionization coefficient for gases

Gas	$A(mm^{-1}Torr^{-1})$	$B(Vmm^{-1}Torr^{-1})$
Helium [158]	4.08×10^{-3}	3.55×10^{-1}
Water [159]	1.00	21.6
Nitrogen [158]	2.13×10^{-1}	15.7
Argon [160]	2.80×10^{-1}	6.06

The working distance, applied detector voltage and the gas pressure were kept constant during our experiments. For a fixed working distance, applied detector voltage and the gas pressure, it is evident from equation 4.3 and Table 4.4 that the effectiveness of charge dissipation for different gases would be different. The above was also evident from the imaging of the gold nanoparticles that were used for focusing during the experiments, helium was found to be more effective than water for charge dissipation as can be seen in Figure 4.7. Therefore, effective charge dissipation and reduced electron scattering in gas correlates with the high contrast values obtained for exposure under helium environment, but establishing detailed mechanism requires more research.
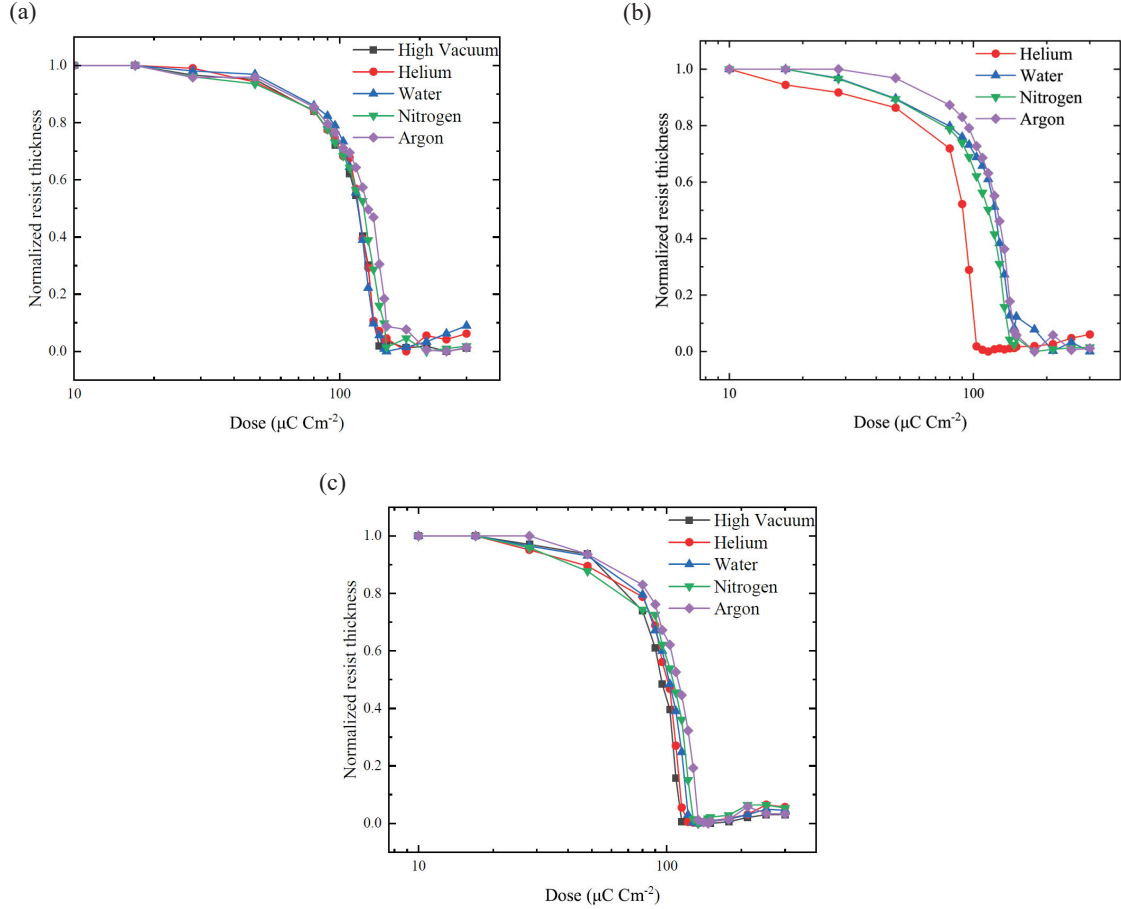
Figure 4.3: Experimental data showing normalized resist thickness vs exposure dose for resist (PMMA) exposure under different ambient gases on (a) silicon, (b) fused silica, and (c) soda lime glass substrates.

4.3.2 Effect of ambient gases on high-resolution patterning of PMMA on insulating substrates

Proximity Effect

For high-resolution highly dense patterns electron scattering in resist and substrate leads to the unintended exposure of adjacent features causing the adjacent features to receive higher than originally intended total electron dose, this effect is well known as the proximity effect. Proximity effect is the most severe factor that limits the ultimate achievable resolution by electron beam lithography process. There are numerous studies investigating the proximity effect theoretically and experimentally providing correction methods to minimize it's effect [161–175]. Backscattered electrons contribute severely to proximity effect [161, 167]. For a given electron beam lithography tool and material, proximity effect is mostly influenced by the mask design and process parameters. Proximity effect if significantly influenced by the shape [163], size

(a) High Vacuum

$D_C = 138 \pm 1\ \mu C/cm^2$

contrast $= 10.3 \pm 0.5$

(b) Helium

$D_C = 138 \pm 1\ \mu C/cm^2$

contrast $= 10.7 \pm 0.7$

(c) Water Vapor

$D_C = 134 \pm 0\ \mu C/cm^2$

contrast $= 12.6 \pm 0.5$

(d) Nitrogen

$D_C = 147 \pm 1\ \mu C/cm^2$

contrast $= 8.4 \pm 0.4$

(e) Argon

$D_C = 155 \pm 1\ \mu C/cm^2$

contrast $= 8.4 \pm 0.5$
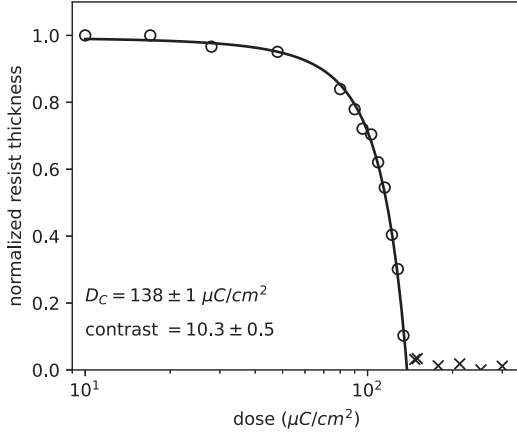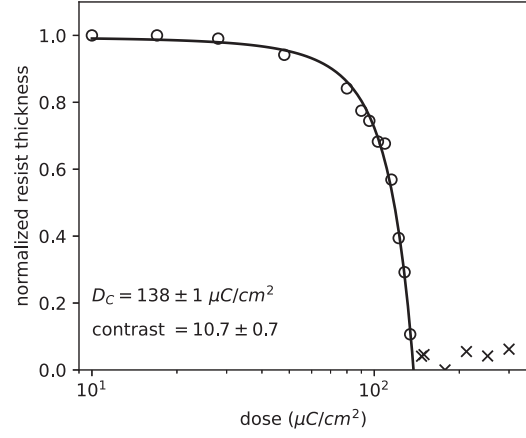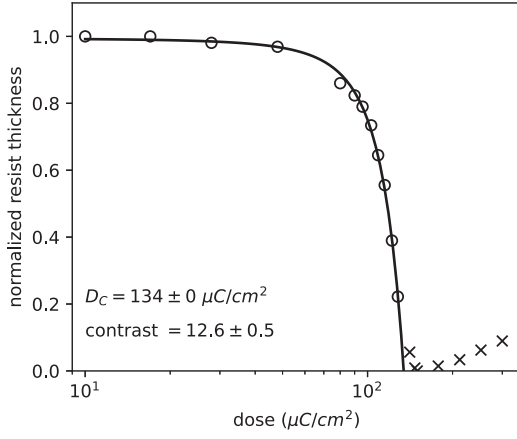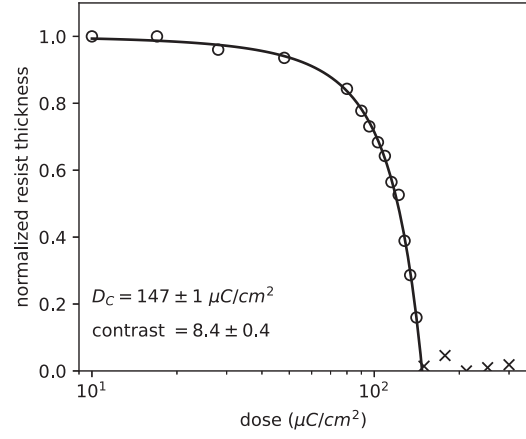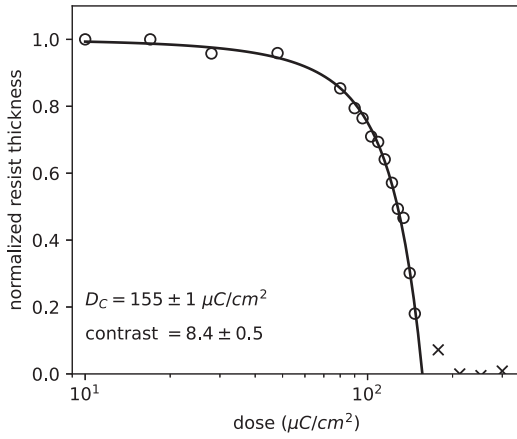
Figure 4.4: Fitted contrast curve (PMMA on silicon) for exposure under (a) High vacuum; 1 mbar of (b) Helium, (c) Water Vapor, (d) Nitrogen, and (e) Argon.
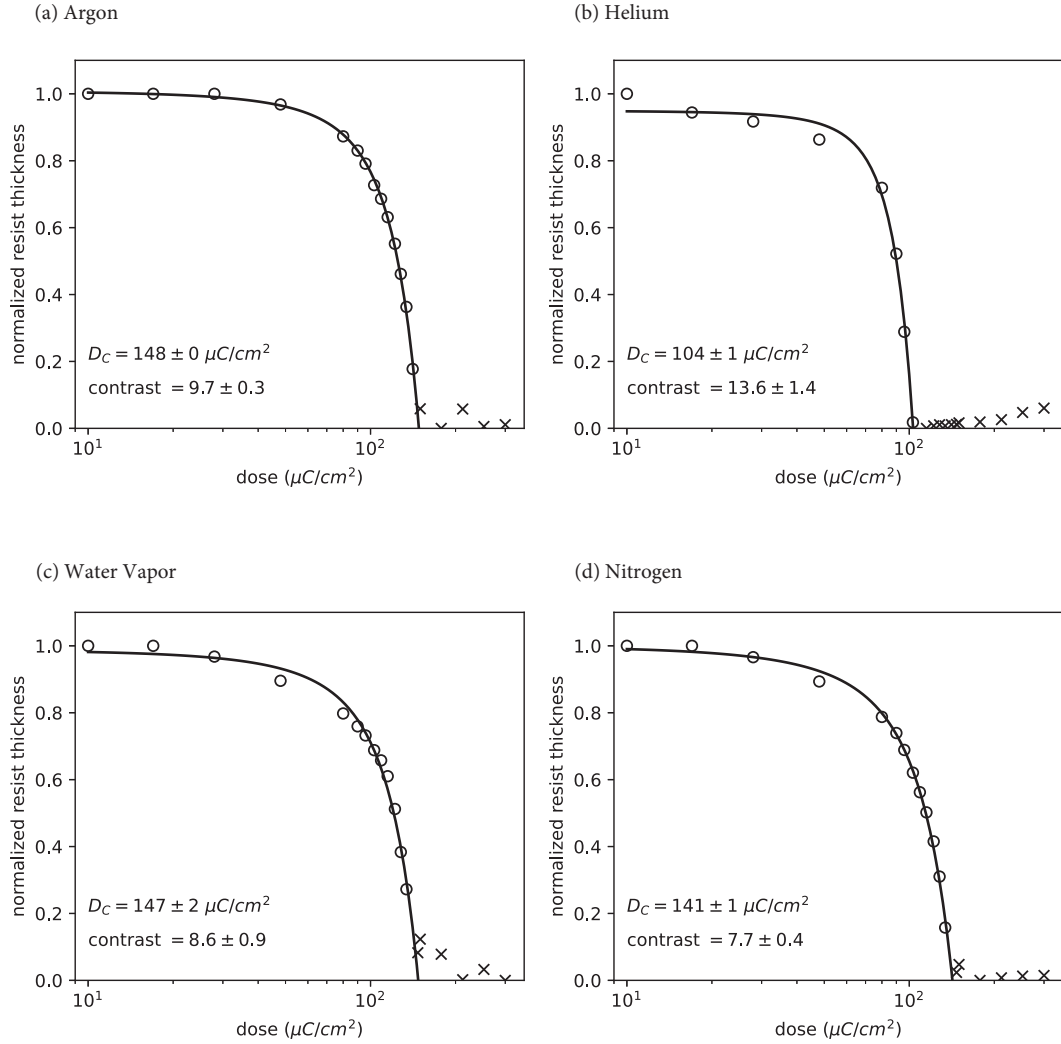
Figure 4.5: Fitted contrast curve (PMMA on fused silica) for exposure under (a) High vacuum; 1 mbar of (b) Helium, (c) Water Vapor, (d) Nitrogen, and (e) Argon, respectively.

(a) High Vacuum

$D_C = 114 \pm 1\ \mu C/cm^2$

contrast $= 9.5 \pm 0.6$

(b) Helium

$D_C = 117 \pm 1\ \mu C/cm^2$

contrast $= 11.7 \pm 0.8$

(c) Water Vapor

$D_C = 122 \pm 0\ \mu C/cm^2$

contrast $= 9.4 \pm 0.3$

(d) Nitrogen

$D_C = 128 \pm 1\ \mu C/cm^2$

contrast $= 8.8 \pm 0.6$

(e) Argon

$D_C = 133 \pm 0\ \mu C/cm^2$

contrast $= 8.8 \pm 0.3$
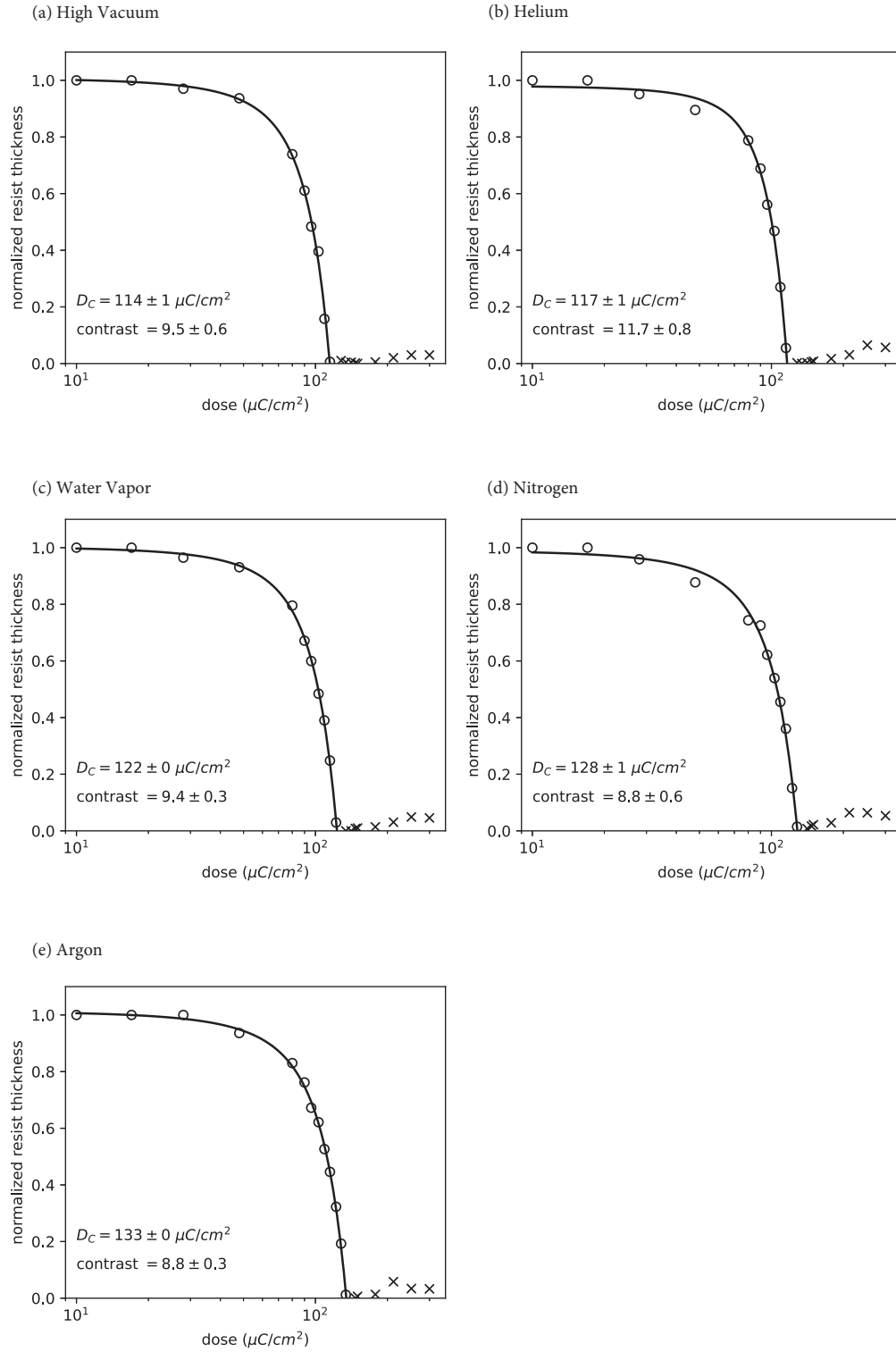
Figure 4.6: Fitted contrast curve (PMMA on soda lime glass) for exposure under (a) High vacuum; 1 mbar of (b) Helium, (c) Water Vapor, (d) Nitrogen, and (e) Argon.
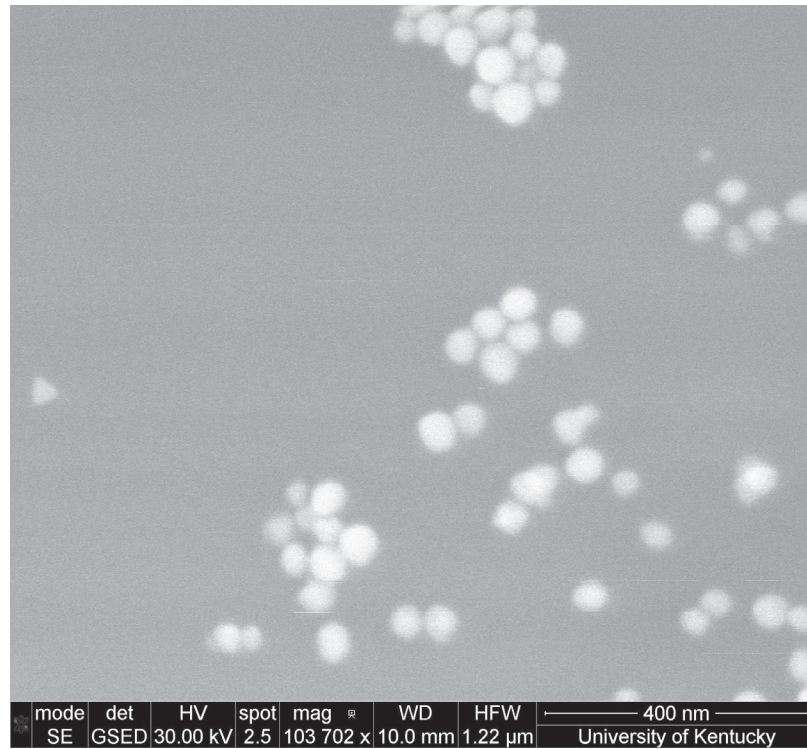
(a)
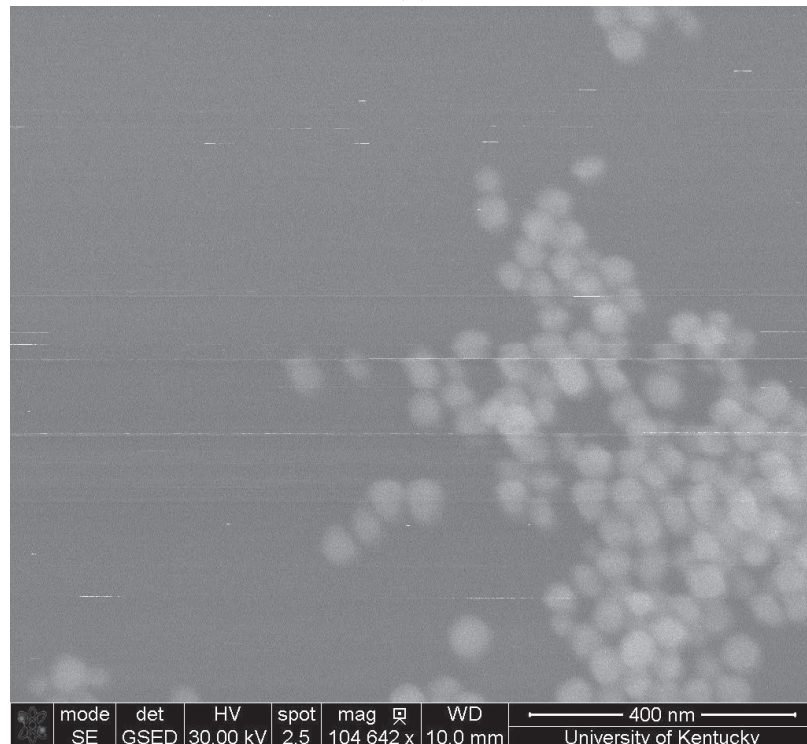
(b)

Figure 4.7: SEM image of the gold nanoparticles on fused silica used for focusing before exposure under (a) Helium, and (b) Water; It's evident that helium dissipates charge more effectively than water.

and density of the patterns, atomic weight of the substrate, exposure dose [164], development conditions as well as the beam energy of the primary electrons used for exposure. Inherently proximity effect is unavoidable but it's effect can be minimized by employing proximity effect compensation techniques as well as using proximity effect correction (PEC) tools. The aim of our present work was to investigate the effect of ambient gas on the contrast, sensitivity and resolution during exposure and no efforts were made to minimize proximity effect except for employing cold development for the highly dense patterns, therefore the result presented in this paper is only for qualitative analysis.

Resolution

Resolution is defined by the minimum feature size of isolated structures or the smallest half-pitch of dense structures that can be patterned. Forward scattering of the beam in the resist and substrate adversely impacts the resolution. Resolution is very closely related to both the sensitivity and contrast. It also becomes necessary to consider other factors including exposure charge density, beam accelerating voltage, resist thickness and resist development process. Fabricating sub-10 nm half-pitch features was found to be limited by the resist-development process [30]. Resist collapse upon development tends to limit resist film thicknesses to no more than three times the minimum feature size for a typical resist.

Feature size (L) can be expressed as a function of exposure dose (D) and the number of electrons used for exposure (N_e) by the following equation:

$$L = \left(\frac{eN_e}{D}\right)^{1/2} \qquad (4.5)$$

High resolution "nested-L" structures, 25 nm half-pitch; PMMA on soda lime glass exposed at 300 pC cm^{-1} and 30 keV beam energy under (a) high Vacuum; and (b) 1 mbar helium, is shown in Figure 4.8. Despite the lower clearing dose, helium still exhibited the best resolution with 25-nm half-pitch dense lines and spaces clearly resolved on soda lime glass. To our knowledge, this is the highest resolution demonstrated to date for EBL in a gaseous environment. From the experiments it is also found that the process window for high resolution patterns gets smaller with increasing atomic number of the scatterer gas.
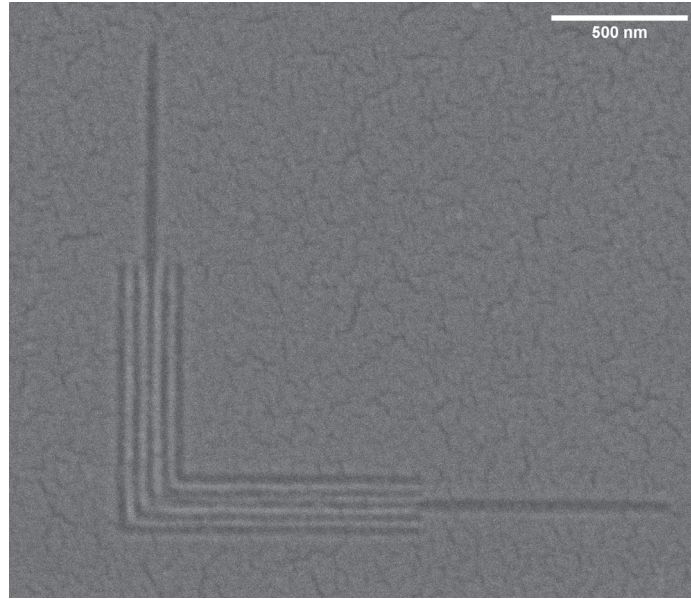
(a)
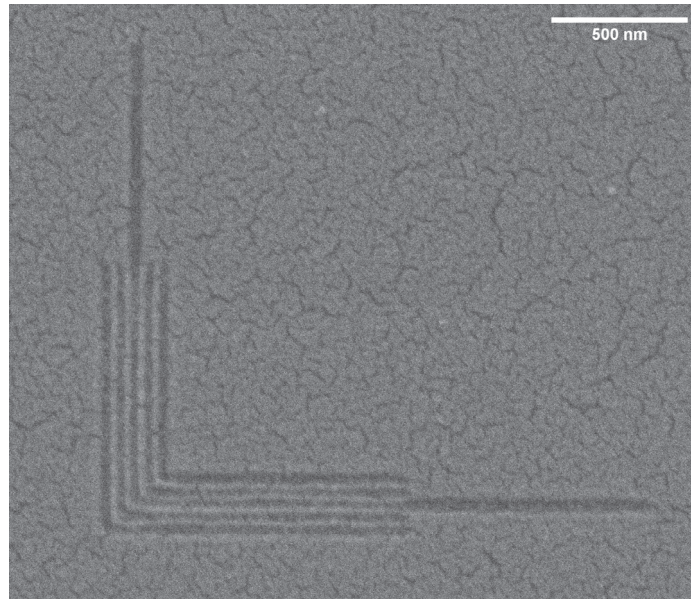
(b)

Figure 4.8: High resolution "nested-L" structures, 25 nm half-pitch; PMMA on soda lime glass exposed at 300 pC cm^{-1} and 30 keV beam energy under (a) high Vacuum; and (b) 1 mbar helium.

4.4 Summary and conclusions

In this work, VP-EBL was conducted to study the effect of ambient gases on contrast and resolution of PMMA on insulating substrates. To our knowledge, these are the first studies of molecules other than water for EBL in gaseous environments. E-beam exposures were conducted under various gases to study their effect of on contrast of PMMA on insulating substrates, the contrast curves for PMMA on fused silica exposed under 1 mbar of helium, water and argon yielded contrast values of 13.6, 8.6 and 9.7, respectively. The clearing dose increases with the gases' molecular weight and proton number, consistent with the increase in scattering cross-section. Our results for PMMA on silicon exposed under 1 mbar water vapor pressure yielded a contrast of 12.6, however, the contrast degrades on insulating substrates and yields distinct values on fused silica and soda lime glass. The degree to which the charge is dissipated under gaseous environment on different substrates is different, resulting in degraded contrast. Helium exhibits improved contrast in all cases. The improved contrast and sensitivity of PMMA exposed under helium motivated us to study the resolution under various gases. Resolution testing indicated that despite the lower clearing dose, helium still exhibited the best resolution with 25-nm half-pitch dense lines and spaces clearly resolved on soda lime glass. To our knowledge, this is the highest resolution demonstrated to date for EBL in a gaseous environment. Thus, VP-EBL of PMMA under helium yields higher sensitivity and contrast on insulating substrates without sacrificing resolution.

Chapter 5 Summary and Future work

5.1 Effect of water vapor pressure on positive and negative tone electron-beam patterning of poly(methyl methacrylate)

In this part of the dissertation, we proved that water vapor pressure affects the contrast and sensitivity during the positive- and negative-tone electron-beam patterning of PMMA on silicon. The results of this study suggest that water vapor did not dramatically affect the sensitivity of PMMA for the positive-tone patterning at vapor pressures up to 3 mbar. In contrast, water vapor dramatically increased the onset dose for negative-tone patterning. However, the contrast of the positive- and the negative-tone process improved in the presence of water vapor. Scattering in water vapor can control the size of the cleared region around negative-tone patterns providing an alternative to large area positive-tone writing to achieve the same end. This effect could be useful for increasing the range of the developed region around cross-linked PMMA far beyond the backscattered electron range. Moreover, the range can be easily tuned by varying the water vapor pressure. All of these results emphasize the dramatic expansion of the lithographic parameter space when conducting electron-beam lithography under reactive gases.

For future work, experiments can be performed to establish the radiation-chemical mechanisms with variable-pressure electron beam lithography that leads to improved contrast under water vapor during the positive- and negative-tone electron-beam patterning of PMMA.

5.2 Enhanced fluorescence from Polystyrene using gas assisted electron-beam patterning

In this part of the dissertation, we reported on a novel method for tuning and enhancing fluorescence properties from polystyrene through electron-beam irradiation under gaseous environments. The results proved that the emission wavelength and photon yield of the irradiated film can be tuned by both dose and gas pressure, significant enhancements in the photoluminescence intensity – up to about 18 times on Sapphire substrate under helium environment compared to high-vacuum exposure – were observed. Overall, the highest photoluminescence yield is observed on soda lime glass substrate under argon environment. Also, the photon-yield on conductive substrates is significantly smaller than that yield from insulating substrates. The peak emission wavelength blue-shifts with increasing gas pressure and could be tuned in the 451 – 544 nm range by varying dose and gas pressure. Thus, localized e-beam synthesis of fluorophores in polystyrene can be controlled by both dose and by ambient gas pressure. This technique could enable new approaches to photonics where fluorophores with tunable emission properties can be locally introduced by e-beam patterning.

For future work, localized e-beam synthesis of fluorophores with higher PL yield and tunable emission properties presented here can be applied to wide range of research fields including directly writing organic solid state lasers, optical markers for anti-counterfeit applications and optical imaging for biomedical applications.

5.3 Enhanced contrast and high-resolution patterning of PMMA on insulating substrates under ambient gases

In this part of the dissertation, we studied the effect of ambient gases on contrast and resolution of PMMA on conducting and insulating substrates. E-beam exposures were conducted under vacuum conditions and 1 mbar of water vapor, helium, nitrogen and argon to study their effect on contrast and resolution of PMMA on silicon, fused silica and soda lime glass substrates. On silicon, exposure under water vapor yielded contrast values significantly higher than vacuum exposure, consistent with our previous work. However, exposure under helium yielded slightly improved contrast compared to vacuum exposure. On insulating substrates exposure under helium environment yielded contrast values significantly higher compared to vacuum exposure. The clearing dose was found to increase with the gases' molecular weight and proton number, consistent with the increase in scattering cross-section. The improved contrast and sensitivity (dose to clear) of PMMA under helium motivated us to study the resolution under various gases. Resolution testing indicated that despite the lower clearing dose, helium still exhibited the best resolution with 25-nm half-pitch dense lines and spaces clearly resolved on soda lime glass. Thus, VP-EBL of PMMA under helium yields higher sensitivity and contrast on insulating substrates without sacrificing resolution.

For future work, electron beam lithography process could be modeled for exposure under gaseous environment to calculate the energy loss in a resist and determine the dissolution rate of the resist to accurately predict the resist profile.

Appendix

Effect of water vapor on contrast and sensitivity during electron beam patterning of ZEP-520A on Silicon substrate

ZEP-520A, a chloromethacrylate-methylstyrene copolymer, is a commonly used alternative to PMMA when higher sensitivity and better etch resistance is required. Thus, we studied the positive tone exposure of ZEP-520A as a function of water vapor pressure as shown in Figures A1, A2 and A3. Unlike PMMA, ZEP showed improved contrast (from 6.9 up to 8.6) under water-vapor for all pressures considered. Regarding dose-to-clear, ZEP and PMMA behaved similarly under water-vapor with only an 9% increase in dose to clear at 3 mbar compared to high-vacuum exposure. Thus, for ZEP-520A, any choice of water-vapor pressure up to 3 mbar will yield improved contrast with little loss in sensitivity.

Figure A1: Contrast curves for positive-tone ZEP-520A exposed at high vacuum and under various water vapor pressures. No dramatic changes in the shape of the contrast curves were observed, but changes in contrast and dose-to-clear, D_C, were present.
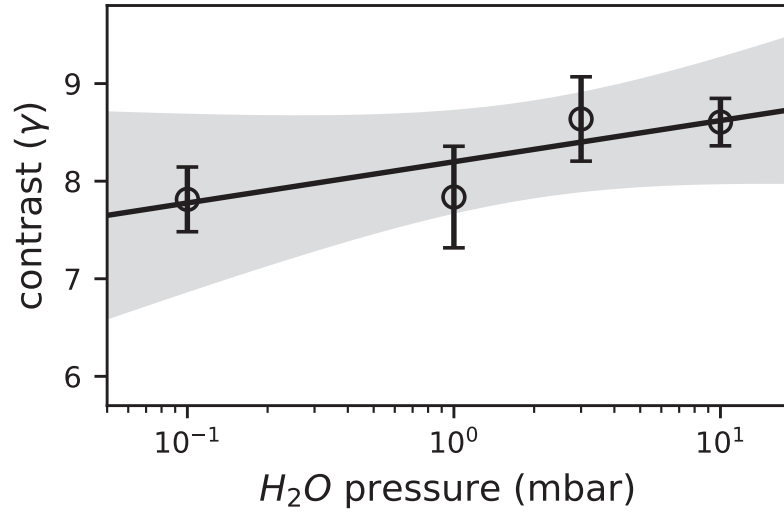
(a) ZEP-520A contrast as a function of water-vapor pressure. Contrast improves slightly as pressure increases and is always higher than that observed for high vacuum exposure. Shaded region represents the 95% confidence interval for the fit.
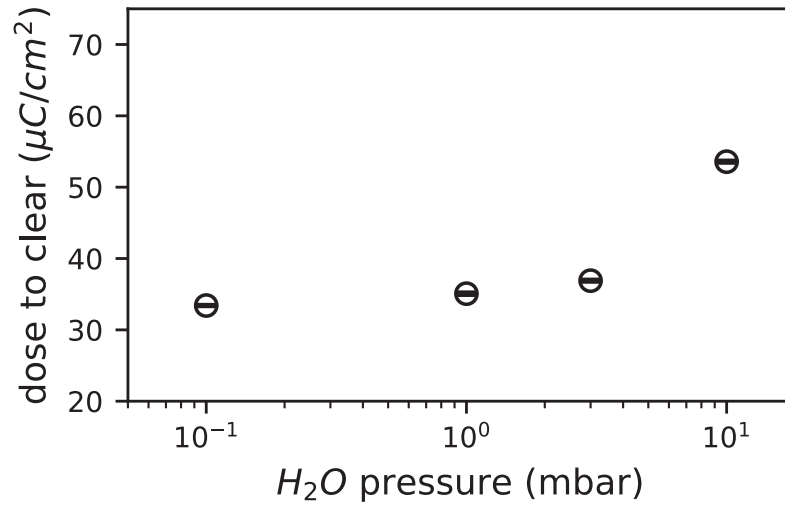
(b) ZEP-520A dose-to-clear vs. water vapor pressure.

Figure A2: ZEP-520A (a) Contrast and (b) dose-to-clear vs. water vapor pressure. Water vapor has only a small effect until the pressure approaches 10 mbar.
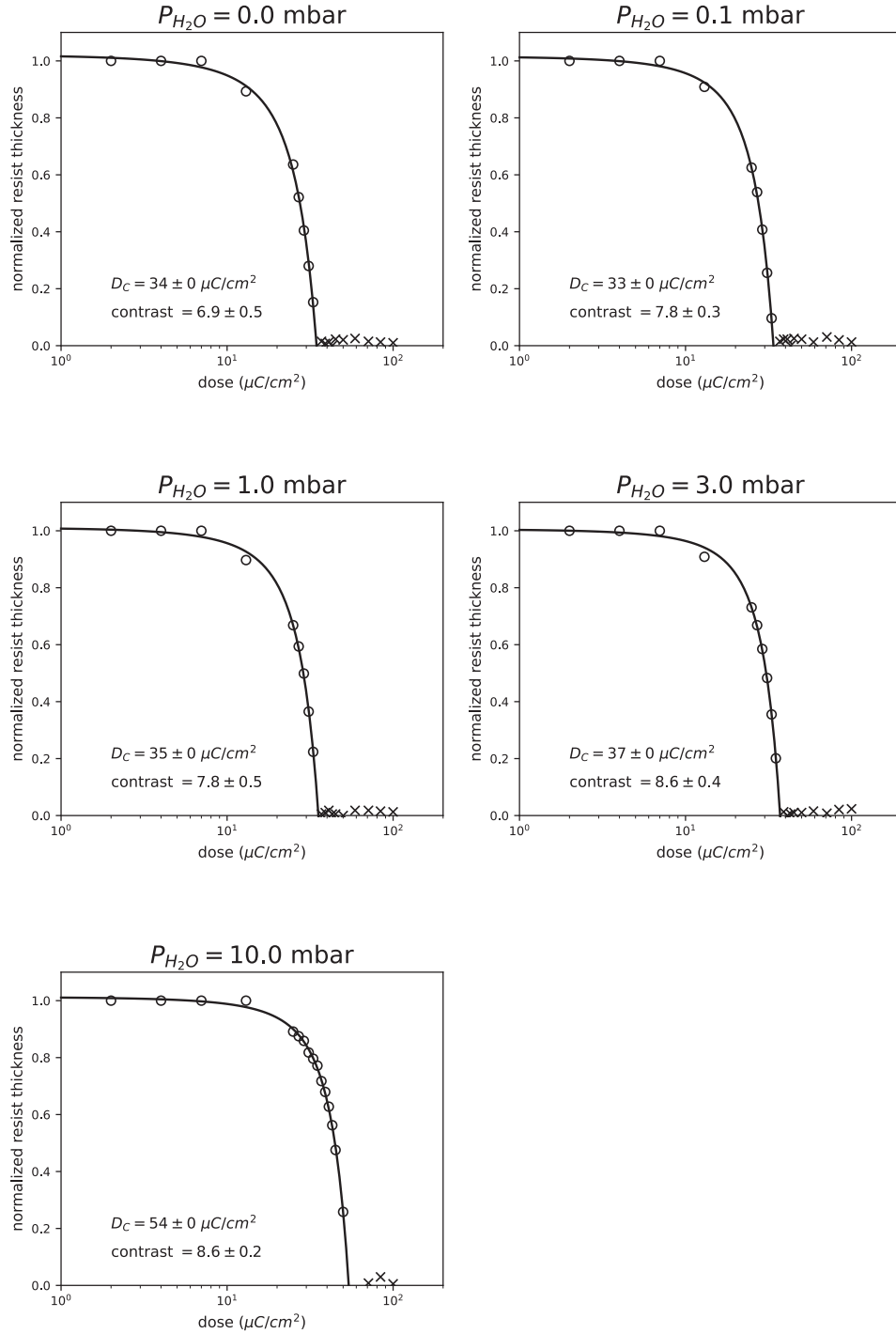
Figure A3: Fitted normalized resist thickness vs exposure dose (ZEP-520A) for each water vapor pressure used during resist exposure. (a) High vacuum; (b) 0.1; (c) 1; (d) 3; and (e) 10 mbar. Data points used for the fit are indicated by a ∘, while data points excluded from the fit are indicated by an ×. Dose to clear, D_C, and contrast for each data set are shown in the inset. Uncertainties represent the standard error of the fitted parameter.

Table A1: Contrast (γ) and dose to clear (D_C) as a function of vapor pressure for ZEP-520A.

Chamber pressure	High vacuum	0.1 mbar H_2O	1 mbar H_2O	3 mbar H_2O	10 mbar H_2O
Contrast	6.9± 0.5	7.8 ± 0.3	7.8 ± 0.5	8.6 ± 0.4	8.6 ± 0.2
Dose to clear (μC cm^{-2})	34 ± 0	33 ± 0	35 ± 0	37 ± 0	54 ± 0

Effect of water vapor on contrast and sensitivity during electron beam patterning of HSQ on Silicon substrate

Hydrogen silsesquioxane (HSQ), a commonly used negative tone resist for high-resolution EBL, spontaneously, but slowly, cross-links in the presence of water-vapor. As a result, its reaction with water-vapor under irradiation was of particular interest. However, the effect of water vapor on the contrast and sensitivity of HSQ was found to be minimal as shown in Figure A4. Contrast varied between 3.4 and 3.7 from high vacuum to 3 mbar water-vapor pressure, but with no significant trend. Increasing the water-vapor pressure to 10 mbar reduced the contrast. Onset dose did not change significantly from high vacuum to 3 mbar, but increased markedly at 10 mbar. Thus, we concluded that water-vapor had little effect on HSQ exposure at pressures commonly used for charge dissipation, and that higher vapor pressures degraded performance.
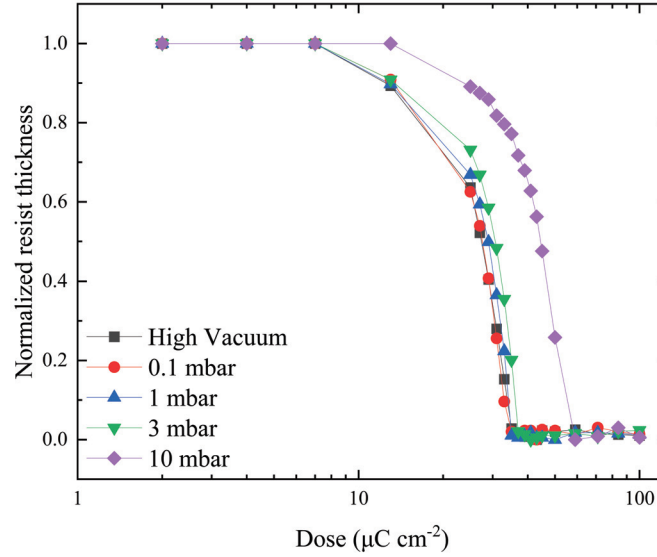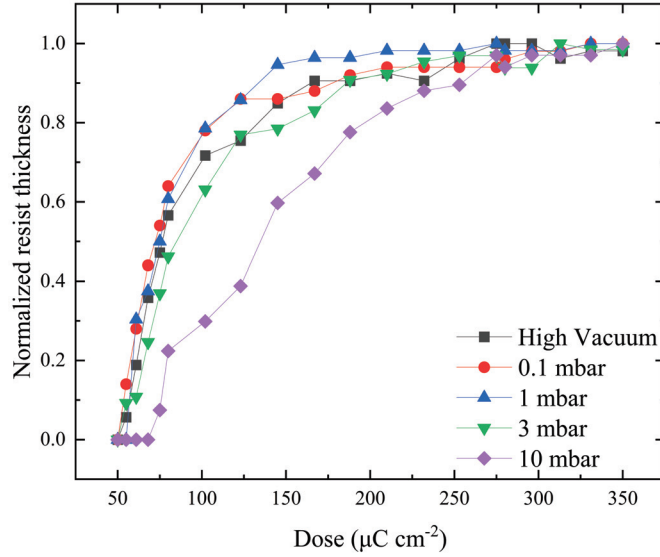

Figure A4: Contrast curves for HSQ exposed at high vacuum and under various water vapor pressures. No dramatic changes in the shape of the contrast curves were observed up to pressures of 3 mbar. Slight changes in the dose-to-clear and contrast can be seen, but overall the affect of water vapor was small. Performance was notably degraded at 10 mbar.

Bibliography

1. Hovington P, Drouin D, and Gauvin R. CASINO: A new Monte Carlo code in C language for electron beam interaction—Part I: Description of the program. Scanning 1997; 19:1–14

2. Kohlmann-von Platen KT and Bruenger WH. Electron-beam induced etching of resist with water vapor as the etching medium. en. Journal of Vacuum Science & Technology B: Microelectronics and Nanometer Structures Processing, Measurement, and Phenomena 1996 Nov; 14:4262–6

3. Jahan M, Ermer D, and Cooke D. Effect of X irradiation on optical properties of Teflon-AF. Radiation Physics and Chemistry 1993; 41:481–6

4. Forsythe JS, Hill DJ, Logothetis AL, and Whittaker AK. The radiation chemistry of the copolymer of tetrafluoroethylene with 2, 2-bis (trifluoromethyl)-4, 5-difluoro-1, 3-dioxole. Polymer degradation and stability 1999; 63:95–101

5. Meyerhofer D. Characteristics of resist films produced by spinning. en. Journal of Applied Physics 1978 Jul; 49:3993–7

6. Emslie AG, Bonner FT, and Peck LG. Flow of a Viscous Liquid on a Rotating Disk. en. Journal of Applied Physics 1958 May; 29:858–62

7. Myers BD and Dravid VP. Variable Pressure Electron Beam Lithography (VP-eBL): A New Tool for Direct Patterning of Nanometer-Scale Features on Substrates with Low Electrical Conductivity. Nano Letters 2006 May; 6. Publisher: American Chemical Society:963–8

8. Griffiths PR. Fourier transform infrared spectrometry. Science 1983; 222:297–302

9. Tseng A, Kuan Chen, Chen C, and Ma K. Electron beam lithography in nanoscale fabrication: recent development. en. IEEE Transactions on Electronics Packaging Manufacturing 2003 Apr; 26:141–9

10. Lee HM, Kim YN, Kim BH, Kim SO, and Cho SO. Fabrication of Luminescent Nanoarchitectures by Electron Irradiation of Polystyrene. Advanced Materials 2008; 20:2094–8

11. Barrios CA, Carrasco S, Canalejas-Tejero V, López-Romero D, Navarro Villoslada F, Moreno-Bondi MC, Fierro JLG, and Capel-Sánchez MC. Fabrication of luminescent nanostructures by electron-beam direct writing of PMMA resist. Materials Letters 2012 Dec; 88:93–6

12. Tatara AM, Shah SR, Sotoudeh M, Henslee AM, Wong ME, Ratcliffe A, Kurtis Kasper F, and Mikos AG. Effects of Electron Beam Sterilization on Mechanical Properties of a Porous Polymethylmethacrylate Space Maintenance Device. Journal of Medical Devices 2015 Jun; 9

13. Zheng N, Min H, Jiang Y, and Cheng X. Polycarbonate as a negative-tone resist for electron-beam lithography. Journal of Vacuum Science & Technology B 2018 Mar; 36:021603

14. Zheng F, Zhang Y, Xia J, Xiao C, and An Z. Charge transportation and permittivity in electron beam irradiated polymethyl methacrylate. Journal of Applied Physics 2009 Sep; 106:064105

15. Gangnaik A, Georgiev YM, McCarthy B, Petkov N, Djara V, and Holmes JD. Characterisation of a novel electron beam lithography resist, SML and its comparison to PMMA and ZEP resists. Microelectronic Engineering. Nano Lithography 2013 2014 Jul; 123:126–30

16. Chung TY, Nest D, Graves DB, Weilnboeck F, Bruce RL, Oehrlein GS, Wang D, Li M, and Hudson EA. Electron, ion and vacuum ultraviolet photon effects in 193 nm photoresist surface roughening. en. Journal of Physics D: Applied Physics 2010 Jun; 43:272001

17. P. Ennis C and I. Kaiser R. Mechanistical studies on the electron-induced degradation of polymethylmethacrylate and Kapton. en. Physical Chemistry Chemical Physics 2010; 12:14902–15

18. Ritsko JJ, Brillson LJ, Bigelow RW, and Fabish TJ. Electron energy loss spectroscopy and the optical properties of polymethylmethacrylate from 1 to 300 eV. The Journal of Chemical Physics 2008 Aug; 69:3931–9

19. Mathakari NL, Bhoraskar VN, and Dhole SD. 6MeV pulsed electron beam induced surface and structural changes in polyimide. Materials Science and Engineering: B. Science and Technologies of Specialty Advanced Materials and Polymers for Aerospace and Defense and Applications : The Proceedings of SAMPADA-2008 Conference 2010 Apr; 168:122–6

20. Sasuga T, Hayakawa N, Yoshida K, and Hagiwara M. Degradation in tensile properties of aromatic polymers by electron beam irradiation. Polymer 1985 Jul; 26:1039–45

21. Cho SO and Jun HY. Surface hardening of poly(methyl methacrylate) by electron irradiation. Nuclear Instruments and Methods in Physics Research Section B: Beam Interactions with Materials and Atoms 2005 Aug; 237:525–32

22. Sabet M, Hassan A, and Ratnam CT. Mechanical, electrical, and thermal properties of irradiated low-density polyethylene by electron beam. en. Polymer Bulletin 2012 May; 68:2323–39

23. Hong YK, Park DH, Park SK, Song H, Kim DC, Kim J, Han YH, Park OK, Lee BC, and Joo J. Tuning and Enhancing Photoluminescence of Light-Emitting Polymer Nanotubes through Electron-Beam Irradiation. en. Advanced Functional Materials 2009; 19:567–72

24. Oleksak RP, Ruther RE, Luo F, Fairley KC, Decker SR, Stickle WF, Johnson DW, Garfunkel EL, Herman GS, and Keszler DA. Chemical and Structural Investigation of High-Resolution Patterning with HafSOx. ACS Applied Materials & Interfaces 2014 Feb; 6. Publisher: American Chemical Society:2917–21

25. Bita B, Stancu E, Stroe D, Dumitrache M, Ciobanu SC, Iconaru SL, Predoi D, and Groza A. The Effects of Electron Beam Irradiation on the Morphological and Physicochemical Properties of Magnesium-Doped Hydroxyapatite/Chitosan Composite Coatings. en. Polymers 2022 Jan; 14. Number: 3 Publisher: Multidisciplinary Digital Publishing Institute:582

26. Lu BR, Lanniel M, Alexandar M, Liu R, Chen Y, and Huq E. Surface stiffness modification by e-beam irradiation for stem cell growth controla). Journal of Vacuum Science & Technology B 2011 Apr; 29:030604

27. Maeno T, Futami T, Kushibe H, and Takada T. Measurements and simulation of the spatial charge distribution in electron-beam-irradiated polymers. en. Journal of Applied Physics 1989 Feb; 65:1147–51

28. Hatzakis M. Electron Resists for Microcircuit and Mask Production. en. Journal of The Electrochemical Society 1969 Jul; 116. Publisher: IOP Publishing:1033

29. Zailer I, Frost J, Chabasseur-Molyneux V, Ford C, and Pepper M. Crosslinked PMMA as a high-resolution negative resist for electron beam lithography and applications for physics of low-dimensional structures. Semiconductor science and technology 1996; 11:1235

30. Duan H, Winston D, Yang JKW, Cord BM, Manfrinato VR, and Berggren KK. Sub-10-nm half-pitch electron-beam lithography by using poly(methyl methacrylate) as a negative resist. Journal of Vacuum Science & Technology B 2010 Dec; 28:C6C58–C6C62

31. Hall TM, Wagner A, and Thompson LF. Ion beam exposure characteristics of resists: Experimental results. en. Journal of Applied Physics 1982 Jun; 53:3997–4010

32. Broers AN, Harper JME, and Molzen WW. 250-Å linewidths with PMMA electron resist. en. Applied Physics Letters 1978 Sep; 33:392–4

33. Hoole ACF, Welland ME, and Broers AN. Negative PMMA as a high-resolution resist - the limits and possibilities. en. Semiconductor Science and Technology 1997 Sep; 12:1166

34. Sultan MA, Lami SK, Ansary A, Strachan DR, Brill JW, and Hastings JT. Altering the radiation chemistry of electron-beam lithography with a reactive gas: a study of Teflon AF patterning under water vapor. en. Nanotechnology 2019 May; 30. Publisher: IOP Publishing:305301

35. Zoukel A, Khouchaf L, Martino JD, and Ruch D. Skirting effects in the variable pressure scanning electron microscope: Limitations and improvements. Micron 2013 Jan; 44:107–14

36. Parker NW, Brodie AD, and McCoy JH. High-throughput NGL electron-beam direct-write lithography system. *Emerging Lithographic Technologies IV*. Vol. 3997. SPIE. 2000 :713–20

37. Newbury DE. X-Ray Microanalysis in the Variable Pressure (Environmental) Scanning Electron Microscope. Journal of Research of the National Institute of Standards and Technology 2002; 107:567–603

38. Newville M, Otten R, Nelson A, Ingargiola A, Stensitzki T, Allan D, Fox A, Carter F, Micha-l, Osborn R, Pustakhod D, lneuhaus, Weigand S, Glenn, Deil C, Mark, Hansen ALR, Pasquevich G, Foks L, Zobrist N, Frost O, Beelen A, Stuermer, azelcer, Hannum A, Polloreno A, Nielsen JH, Caldwell S, Almarza A, and Persaud A. lmfit/lmfit-py: 1.0.3. 2021 Oct

39. Choi JO, Moore JA, Corelli JC, Silverman JP, and Bakhru H. Degradation of poly(methylmethacrylate) by deep ultraviolet, x-ray, electron beam, and proton beam irradiations. en. Journal of Vacuum Science & Technology B: Microelectronics Processing and Phenomena 1988 Nov; 6:2286–9

40. Hiraoka H. Radiation Chemistry of Poly(methacrylates). IBM Journal of Research and Development 1977 Mar; 21. Conference Name: IBM Journal of Research and Development:121–30

41. Bermudez VM. Low-energy electron-beam effects on poly(methyl methacry-late) resist films. en. Journal of Vacuum Science & Technology B: Microelec-tronics and Nanometer Structures Processing, Measurement, and Phenomena 1999 Nov; 17:2512–8

42. Ocola LE, Costales M, and Gosztola DJ. Development characteristics of poly-methyl methacrylate in alcohol/water mixtures: a lithography and Raman spec-troscopy study. en. Nanotechnology 2015 Dec; 27. Publisher: IOP Publish-ing:035302

43. Danilatos GD. Foundations of Environmental Scanning Electron Microscopy. en. *Advances in Electronics and Electron Physics*. Ed. by Hawkes PW. Vol. 71. Academic Press, 1988 Jan :109–250

44. Myers B, Pan Z, and Dravid V. Beam skirting effects on energy deposition profile in VP-SEM. en. Microscopy and Microanalysis 2008 Aug; 14:1208–9

45. Willis HA, Zichy VJI, and Hendra PJ. The laser-Raman and infra-red spectra of poly(methyl methacrylate). Polymer 1969 Jan; 10:737–46

46. Dirlikov S and Koenig JL. Infrared Spectra of Poly(Methyl Methacrylate) La-beled with Oxygen-18. en. Applied Spectroscopy 1979 Nov; 33:551–5

47. Royall CP, Thiel BL, and Donald AM. Radiation damage of water in environ-mental scanning electron microscopy. en. Journal of Microscopy 2001; 204:185–95

48. Kitching and Donald. Beam damage of polypropylene in the environmental scanning electron microscope: an FTIR study. en. Journal of Microscopy 1998; 190:357–65

49. Jenkins LM and Donald AM. Use of the environmental scanning electron microscope for the observation of the swelling behaviour of cellulosic fibres. en. Scanning 1997; 19:92–7

50. Spinney PS, Howitt DG, Collins SD, and Smith RL. Electron beam stimulated oxidation of carbon. en. Nanotechnology 2009 Oct; 20:465301

51. Stark TJ, Shedd GM, Vitarelli J, Griffis DP, and Russell PE. H2O enhanced focused ion beam micromachining. en. Journal of Vacuum Science & Technology B: Microelectronics and Nanometer Structures Processing, Measurement, and Phenomena 1995 Nov; 13:2565–9

52. Stark TJ, Griffis DP, and Russell PE. Characterization of resist profiles using water enhanced focused ion beam micromachining. en. Journal of Vacuum Science & Technology B: Microelectronics and Nanometer Structures Processing, Measurement, and Phenomena 1996 Nov; 14:3990–5

53. Utke I, Hoffmann P, and Melngailis J. Gas-assisted focused electron beam and ion beam processing and fabrication. Journal of Vacuum Science & Technology B: Microelectronics and Nanometer Structures Processing, Measurement, and Phenomena 2008 Aug; 26:1197–276

54. Makarov OP, Ajello JM, Vattipalle P, Kanik I, Festou MC, and Bhardwaj A. Kinetic energy distributions and line profile measurements of dissociation products of water upon electron impact. en. Journal of Geophysical Research: Space Physics 2004 Sep; 109:2002JA009353

55. Monckton R. Low-energy Electron Interactions with Water. en

56. Ogawa T, Yonekura N, Tsukada M, Ihara S, Yasuda T, Tomura H, Nakashima K, and Kawazumi H. Electron-impact dissociation of water as studied by the angular difference Doppler profiles of the excited hydrogen atom. The Journal of Physical Chemistry 1991 Apr; 95. Publisher: American Chemical Society:2788–92

57. Lehockey EM, Reid I, and Hill I. The radiation chemistry of poly(methyl methacrylate) polymer resists. en. Journal of Vacuum Science & Technology A: Vacuum, Surfaces, and Films 1988 Jul; 6:2221–5

58. Hong W, Woo HJ, Choi HW, Kim YS, and Kim Gd. Optical property modification of PMMA by ion-beam implantation. Applied Surface Science 2001 Jan; 169-170:428–32

59. Erasmus SJ. Damage to resist structures during scanning electron microscope inspection. en. Journal of Vacuum Science & Technology B: Microelectronics Processing and Phenomena 1987 Jan; 5:409–13

60. Borzenko B, Vyatkin AF, Gonchakova NN, and Kudryashov VA. The effect of ion implantation on polymer mask resistance to ion beam etching. en. 1988

61. Shaw JC, Rishton SA, Jackson RR, and O'Boyle MP. Latent image measurements in electron beam exposed polymethylmethacrylate. Applied Physics Letters 1991 Jan; 58:310–2

62. Woodward JT, Choi KW, Prabhu VM, Kang S, Lavery KA, Wu Wl, Leeson M, De Silva A, Felix NM, and Ober CK. Characterization of the latent image to developed image in model EUV photoresists. en. Ed. by Henderson CL. San Jose, California, USA, 2008 Mar :69232B

63. Dobisz EA, Brandow SL, Snow E, and Bass R. Atomic force microscope studies of nanolithographic exposure and development of polymethylmethacrylate. en. Journal of Vacuum Science & Technology B: Microelectronics and Nanometer Structures Processing, Measurement, and Phenomena 1997 Nov; 15:2318–22

64. Dobisz EA, Brandow SL, Bass R, and Shirey LM. Nanolithography in poly-methylmethacrylate: An atomic force microscope study. en. Journal of Vacuum Science & Technology B: Microelectronics and Nanometer Structures Processing, Measurement, and Phenomena 1998 Nov; 16:3695–700

65. Doehne E and Bower NW. Empirical evaluation of the electron skirt in the environmental SEM: Implications for energy dispersive X-ray analysis. en. 1993

66. Leontowich AFG, Hitchcock AP, Tyliszczak T, Weigand M, Wang J, and Karunakaran C. Accurate dosimetry in scanning transmission X-ray micro-scopes *via* the cross-linking threshold dose of poly(methyl methacrylate). en. Journal of Synchrotron Radiation 2012 Nov; 19:976–87

67. Pavia DL, Lampman GM, Kriz GS, and Vyvyan JR. Introduction to spectroscopy. eng. Fifth edition. OCLC: 864087517. Stamford, CT: Cengage Learning, 2015

68. Pijpers AP and Donners WaB. Quantitative determination of the surface composition of acrylate copolymer latex films by XPS (ESCA). en. Journal of Polymer Science: Polymer Chemistry Edition 1985; 23:453–62

69. Pijpers AP and Donners WaB. Reply to Gardella et al.'s "comments on 'quantitative determination of the surface composition of acrylate copolymer latex films by XPS (ESCA)'". en. Journal of Polymer Science Part C: Polymer Letters 1986; 24:653–5

70. Naves de Brito A, Keane MP, Correia N, Svensson S, Gelius U, and Lindberg BJ. Experimental and theoretical XPS study of model molecules for poly(methyl methacrylate). en. Surface and Interface Analysis 1991; 17:94–104

71. Beamson G, Bunn A, and Briggs D. High-resolution monochromated XPS of poly(methyl methacrylate) thin films on a conducting substrate. en. Surface and Interface Analysis 1991; 17:105–15

72. Louette P, Bodino F, and Pireaux JJ. Poly(methyl methacrylate) (PMMA) XPS Reference Core Level and Energy Loss Spectra. Surface Science Spectra 2005 Dec; 12. Publisher: American Vacuum Society:69–73

73. Girardeaux C and Pireaux JJ. Analysis of Poly(methyl methacrylate) (PMMA) by XPS. Surface Science Spectra 1996 Apr; 4. Publisher: American Vacuum Society:134–7

74. Linford MR. The Gaussian-Lorentzian sum, product, and convolution (Voigt) functions used in peak fitting XPS narrow scans, and an introduction to the impulse function. Vacuum Technology & Coating 2014 :2–9

75. Gengenbach TR, Major GH, Linford MR, and Easton CD. Practical guides for x-ray photoelectron spectroscopy (XPS): Interpreting the carbon 1s spectrum. Journal of Vacuum Science & Technology A 2021 Jan; 39. Publisher: American Vacuum Society:013204

76. Toyoda N and Yamada I. XPS study of effects of water vapor during Ar-GCIB irradiations on PMMA. en. Applied Surface Science. Selected manuscripts arising from the 18th International Conference on Surface Modification of Materials by Ion Beams (SMMIB-2013) 2014 Aug; 310:112–4

77. Qiao ZA, Wang Y, Gao Y, Li H, Dai T, Liu Y, and Huo Q. Commercially activated carbon as the source for producing multicolor photoluminescent carbon dots by chemical oxidation. en. Chemical Communications 2009 Nov; 46. Publisher: The Royal Society of Chemistry:8812–4

78. Sun YP, Zhou B, Lin Y, Wang W, Fernando KAS, Pathak P, Meziani MJ, Harruff BA, Wang X, Wang H, Luo PG, Yang H, Kose ME, Chen B, Veca LM, and Xie SY. Quantum-Sized Carbon Dots for Bright and Colorful Photoluminescence. Journal of the American Chemical Society 2006 Jun; 128. Publisher: American Chemical Society:7756–7

79. Zhou J, Booker C, Li R, Zhou X, Sham TK, Sun X, and Ding Z. An Electrochemical Avenue to Blue Luminescent Nanocrystals from Multiwalled Carbon Nanotubes (MWCNTs). Journal of the American Chemical Society 2007 Jan; 129. Publisher: American Chemical Society:744–5

80. Ma Z, Ming H, Huang H, Liu Y, and Kang Z. One-step ultrasonic synthesis of fluorescent N-doped carbon dots from glucose and their visible-light sensitive photocatalytic ability. en. New Journal of Chemistry 2012; 36. Publisher: Royal Society of Chemistry:861–4

81. Sun D, Ban R, Zhang PH, Wu GH, Zhang JR, and Zhu JJ. Hair fiber as a precursor for synthesizing of sulfur-and nitrogen-co-doped carbon dots with tunable luminescence properties. Carbon 2013; 64:424–34

82. Zhai X, Zhang P, Liu C, Bai T, Li W, Dai L, and Liu W. Highly luminescent carbon nanodots by microwave-assisted pyrolysis. en. Chemical Communications 2012; 48:7955

83. Prasannan A and Imae T. One-Pot Synthesis of Fluorescent Carbon Dots from Orange Waste Peels. en. Industrial & Engineering Chemistry Research 2013 Nov; 52:15673–8

84. Zhu S, Meng Q, Wang L, Zhang J, Song Y, Jin H, Zhang K, Sun H, Wang H, and Yang B. Highly photoluminescent carbon dots for multicolor patterning, sensors, and bioimaging. Angewandte Chemie International Edition 2013; 52:3953–7

85. Song Y, Zhu S, Zhang S, Fu Y, Wang L, Zhao X, and Yang B. Investigation from chemical structure to photoluminescent mechanism: a type of carbon dots from the pyrolysis of citric acid and an amine. Journal of Materials Chemistry C 2015; 3:5976–84

86. Dong Y, Wang R, Li H, Shao J, Chi Y, Lin X, and Chen G. Polyamine-functionalized carbon quantum dots for chemical sensing. Carbon 2012 Jul; 50:2810–5

87. Bindl DJ, Wu MY, Prehn FC, and Arnold MS. Efficiently harvesting excitons from electronic type-controlled semiconducting carbon nanotube films. Nano Letters 2011; 11:455–60

88. Cao L, Wang X, Meziani MJ, Lu F, Wang H, Luo PG, Lin Y, Harruff BA, Veca LM, Murray D, Xie SY, and Sun YP. Carbon Dots for Multiphoton Bioimaging. Journal of the American Chemical Society 2007 Sep; 129. Publisher: American Chemical Society:11318–9

89. Zhang W, Zhu H, Yu SF, and Yang H. Observation of lasing emission from carbon nanodots in organic solvents. Advanced Materials 2012; 24:2263–7

90. Lai JH and Shepherd LT. Experimental Observations of Nearly Monodisperse Polystyrene as Negative Electron Resists. en. Journal of The Electrochemical Society 1979 Apr; 126. Publisher: IOP Publishing:696

91. Itaya K, Shibayama K, and Fujimoto T. High Resolution Electron Beam Negative Resist with Very Narrow Molecular Weight Distributions. en. Journal of The Electrochemical Society 1982 Mar; 129. Publisher: IOP Publishing:663

92. Manako S, Fujita Ji, Ochiai Y, Eiichi Nomura EN, and Shinji Matsui SM. Nanometer-Scale Patterning of Polystyrene Resists in Low-Voltage Electron Beam Lithography. Japanese Journal of Applied Physics 1997 Dec; 36:7773

93. Manako S, Fujita Ji, Ochiai Y, Eiichi Nomura EN, and Shinji Matsui SM. Resolution-Limit Study of Chain-Structure Negative Resist by Electron Beam Lithography. Japanese Journal of Applied Physics 1997 Jun; 36:L724

94. Ma S, Con C, Yavuz M, and Cui B. Polystyrene negative resist for high-resolution electron beam lithography. Nanoscale Research Letters 2011 Jul; 6:446

95. Con C, Dey R, Ferguson M, Zhang J, Mansour R, Yavuz M, and Cui B. High molecular weight polystyrene as very sensitive electron beam resist. en. Microelectronic Engineering. Special issue MNE 2011 - Part II 2012 Oct; 98:254–7

96. Con C, Abbas AS, Yavuz M, and Cui B. Dry thermal development of negative electron beam resist polystyrene. en. Advances in Nano Research 2013 Jun; 1. Number: 2:105–9

97. Dey RK and Cui B. Effect of molecular weight distribution on e-beam exposure properties of polystyrene. en. Nanotechnology 2013 May; 24. Publisher: IOP Publishing:245302

98. Gupta MC, Gupta A, Horwitz J, and Kliger D. Time-resolved fluorescence and emission depolarization studies on polystyrene: photochemical processes in polymeric systems. 9. Macromolecules 1982 Sep; 15. Publisher: American Chemical Society:1372–6

99. Lee HM and Cho SO. Photoluminescence of the electron irradiated Polystyrene. INIS Reference Number: 37098942. Korea, Republic of: KNS, 2006 :1CD–ROM

100. Lee HM and Cho SOC. Liquid and Solid-State NMR study of the electron irradiated Polystyrene. INIS Reference Number: 38113625. Korea, Republic of: KNS, 2007

101. Kamura Y and Imura K. Fabrication method of two-photon luminescent organic nano-architectures using electron-beam irradiation. Applied Physics Letters 2018 Jun; 112. Publisher: American Institute of Physics:243104

102. Kamura Y and Imura K. Space-Selective Fabrication of Light-Emitting Carbon Dots in Polymer Films Using Electron-Beam-Induced Chemical Reactions. English. Acs Omega 2019 Feb; 4. Place: Washington Publisher: Amer Chemical Soc WOS:000460237300097:3380–4

103. Kumar D, Chaudhuri K, Brill JW, Pham JT, and Hastings JT. Effect of water vapor pressure on positive and negative tone electron-beam patterning of poly(methyl methacrylate). Journal of Vacuum Science & Technology B 2023 Jan; 41:012604

104. Alexander P, Charlesby A, and Freeth FA. Radiation protection in copolymers of isobutylene and styrene. Proceedings of the Royal Society of London. Series A. Mathematical and Physical Sciences 1997 Jan; 230. Publisher: Royal Society:136–45

105. Charlesby A. Swelling properties of polystyrene crosslinked by high energy radiation. en. Journal of Polymer Science 1953; 11:521–9

106. Koike M and Danno A. Radiation Effects on Dimethyl-diphenyl Siloxane Copolymer. I. Protective Effect of Phenyl Radical on the Cross-linking. Journal of the Physical Society of Japan 1960 Aug; 15. Publisher: The Physical Society of Japan:1501–8

107. Burlant W, Neerman J, and Serment V. γ-radiation of p-substituted polystyrenes. Journal of Polymer Science 1962; 58:491–500

108. Delides CG. The protective effect of phenyl group on the crosslinking of irradiated dimethyldiphenylsiloxane. Radiation Physics and Chemistry (1977) 1980 Jan; 16:345–52

109. Pankratova LN, Bugaenko LT, and Revina AA. Effect of aromatic protectors on the radiolysis of polyorganosiloxanes. en. High Energy Chemistry 2000 Jan; 34:16–22

110. Randall JC, Zoepfl FJ, and Silverman J. A 13C NMR study of radiation-induced long-chain branching in polyethylene. en. Die Makromolekulare Chemie, Rapid Communications 1983; 4:149–57

111. Horii F, Zhu Q, Kitamaru R, and Yamaoka H. Carbon-13 NMR study of radiation-induced crosslinking of linear polyethylene. Macromolecules 1990 Feb; 23. Publisher: American Chemical Society:977–81

112. Radiation Damage to Organic Materials in Nuclear Reactors and Radiation Environments (Proceedings of a Final Research Co-ordination Meeting, Takasaki, Japan, 17-20 July 1989). TECDOC Series 551. Vienna: INTERNATIONAL ATOMIC ENERGY AGENCY, 1990

113. Pivin JC, Sendova-Vassileva M, Colombo P, and Martucci A. Photoluminescence of composite ceramics derived from polysiloxanes and polycarbosilanes by ion irradiation. Materials Science and Engineering: B 2000 Jan; 69-70:574–7

114. Huth M, Porrati F, Schwalb C, Winhold M, Sachser R, Dukic M, Adams J, and Fantner G. Focused electron beam induced deposition: A perspective. Beilstein journal of nanotechnology 2012; 3:597–619

115. Krysmann MJ, Kelarakis A, Dallas P, and Giannelis EP. Formation mechanism of carbogenic nanoparticles with dual photoluminescence emission. Journal of the American Chemical Society 2012; 134:747–50

116. Zhang Y, Wang Y, Feng X, Zhang F, Yang Y, and Liu X. Effect of reaction temperature on structure and fluorescence properties of nitrogen-doped carbon dots. Applied Surface Science 2016; 387:1236–46

117. Gedeon O, Jurek K, and Hulıénskỳ V. Fast migration of alkali ions in glass irradiated by electrons. Journal of non-crystalline solids 1999; 246:1–8

118. Gedeon O, Hulínskỳ V, and Jurek K. Microanalysis of glass containing alkali ions. Microchimica Acta 2000; 132:505–10

119. Wang J, Wang CF, and Chen S. Amphiphilic egg-derived carbon dots: rapid plasma fabrication, pyrolysis process, and multicolor printing patterns. Angewandte Chemie-International Edition 2012; 51:9297

120. Tang L, Ji R, Li X, Teng KS, and Lau SP. Size-dependent structural and optical characteristics of glucose-derived graphene quantum dots. Particle & Particle Systems Characterization 2013; 30:523–31

121. Peng H, Li Y, Jiang C, Luo C, Qi R, Huang R, Duan CG, and Travas-Sejdic J. Tuning the properties of luminescent nitrogen-doped carbon dots by reaction precursors. Carbon 2016; 100:386–94

122. Ghosh S, Chizhik AM, Karedla N, Dekaliuk MO, Gregor I, Schuhmann H, Seibt M, Bodensiek K, Schaap IAT, Schulz O, Demchenko AP, Enderlein J, and Chizhik AI. Photoluminescence of Carbon Nanodots: Dipole Emission Centers and Electron–Phonon Coupling. Nano Letters 2014 Oct; 14. Publisher: American Chemical Society:5656–61

123. Dong Y, Pang H, Yang HB, Guo C, Shao J, Chi Y, Li CM, and Yu T. Carbon-Based Dots Co-doped with Nitrogen and Sulfur for High Quantum Yield and Excitation-Independent Emission. Angewandte Chemie 2013; 125:7954–8

124. Nie H, Li M, Li Q, Liang S, Tan Y, Sheng L, Shi W, and Zhang SXA. Carbon Dots with Continuously Tunable Full-Color Emission and Their Application in Ratiometric pH Sensing. Chemistry of Materials 2014 May; 26. Publisher: American Chemical Society:3104–12

125. Wen X, Yu P, Toh YR, Hao X, and Tang J. Intrinsic and Extrinsic Fluorescence in Carbon Nanodots: Ultrafast Time-Resolved Fluorescence and Carrier Dynamics. en. Advanced Optical Materials 2013; 1:173–8

126. Yu P, Wen X, Toh YR, and Tang J. Temperature-Dependent Fluorescence in Carbon Dots. The Journal of Physical Chemistry C 2012 Dec; 116. Publisher: American Chemical Society:25552–7

127. Das SK, Liu Y, Yeom S, Kim DY, and Richards CI. Single-Particle Fluorescence Intensity Fluctuations of Carbon Nanodots. Nano Letters 2014 Feb; 14. Publisher: American Chemical Society:620–5

128. Kim E, Kyhm J, Kim JH, Lee GY, Ko DH, Han IK, and Ko H. White light emission from polystyrene under pulsed ultra violet laser irradiation. en. Scientific Reports 2013 Nov; 3. Number: 1 Publisher: Nature Publishing Group:3253

129. Toth M and Phillips MR. The effects of space charge on contrast in images obtained using the environmental scanning electron microscope. en. Scanning 2000; 22:319–25

130. He J and Joy DC. Measurement of total gas scattering cross-section. en. Scanning 2003; 25:285–90

131. Rattenberger J, Wagner J, Schröttner H, Mitsche S, and Zankel A. A method to measure the total scattering cross section and effective beam gas path length in a low-vacuum SEM. en. Scanning 2009; 31:107–13

132. Cummings K and Kiersh M. Charging effects from electron beam lithography. Journal of Vacuum Science & Technology B: Microelectronics Processing and Phenomena 1989; 7:1536–9

133. Nagasawa K, Watanabe R, Tanaka Y, and Takada T. Charge accumulation in election beam irradiated various polymers. en. *2008 International Symposium on Electrical Insulating Materials (ISEIM 2008)*. Yokkaichi: IEEE, 2008 Sep :147–50

134. Nagasawa K, Honjoh M, Miyake H, Watanabe R, Tanaka Y, and Takada T. Charge Accumulation in Various Electron-Beam-Irradiated Polymers. en. IEEJ Transactions on Electrical and Electronic Engineering 2010; 5:410–5

135. Huber ML and Harvey AH. Thermal Conductivity of Gases. en. NIST 2011 Jun; 92nd Ed. Last Modified: 2017-02-19T20:02-05:00 Publisher: Marcia L. Huber, Allan H. Harvey:240–1

136. Schram B, De Heer F, Van Der Wiel M, and Kistemaker J. Ionization cross sections for electrons (0.6–20 keV) in noble and diatomic gases. en. Physica 1965 Jan; 31:94–112

137. Schutten J, Heer FJ de, Moustafa HR, Boerboom AJH, and Kistemaker J. Gross- and Partial-Ionization Cross Sections for Electrons on Water Vapor in the Energy Range 0.1–20 keV. The Journal of Chemical Physics 1966 May; 44. Publisher: American Institute of Physics:3924–8

138. Pala N and Karabiyik M. Electron Beam Lithography (EBL). en. *Encyclopedia of Nanotechnology*. Ed. by Bhushan B. Dordrecht: Springer Netherlands, 2012 :718–40

139. Cummings KD and Kiersh M. Charging effects from electron beam lithography. en. Journal of Vacuum Science & Technology B: Microelectronics Processing and Phenomena 1989 Nov; 7:1536–9

140. Joo J, Chow BY, and Jacobson JM. Nanoscale Patterning on Insulating Substrates by Critical Energy Electron Beam Lithography. en. Nano Letters 2006 Sep; 6:2021–5

141. Angelopoulos M, Patel N, Shaw JM, Labianca NC, and Rishton SA. Water soluble conducting polyanilines: applications in lithography. Journal of Vacuum Science & Technology B: Microelectronics and Nanometer Structures Processing, Measurement, and Phenomena 1993; 11:2794–7

142. Cumming DRS, Khandaker II, Thoms S, and Casey BG. Efficient diffractive optics made by single-step electron beam lithography in solid PMMA. en. Journal of Vacuum Science & Technology B: Microelectronics and Nanometer Structures Processing, Measurement, and Phenomena 1997 Nov; 15:2859–63

143. Samantaray CB and Hastings JT. The effect of thin metal overlayers on the electron beam exposure of polymethyl methacrylate. Journal of Vacuum Science & Technology B: Microelectronics and Nanometer Structures Processing, Measurement, and Phenomena 2008 Dec; 26:2300–5

144. Lopez G, Villafranca Gd, Shao G, Zhang M, and Thompson A. Charge dissipation by use of a novel aqueous based quaternary ammonium compound for use in electron beam lithography on non-conductive substrates. *Advances in Patterning Materials and Processes XXXVI*. Vol. 10960. SPIE, 2019 Mar :283–90

145. Hambitzer A, Olziersky A, Saranovac T, and Bolognesi CR. Comparison of Charge Dissipation Layers and Dose Sensitivity of PMMA Electron Beam Lithography on Transparent Insulating Substrates such as GaN. *International Conference on Compound Semiconductor Manufacturing Technology (CS ManTech 2017), Indian Wells, CA, US*. 2017

146. McCord M and Michael R. Electron beam lithography, Handbook of Microlithography, Micromachining and Microfabrication, vol. 1. 1997

147. Paul B and Klimkiewicz M. Application of an environmental scanning electron microscope to micromechanical fabrication. Scanning: The Journal of Scanning Microscopies 1996; 18:490–6

148. Paul B. Effects of gas pressure on low-pressure electron-beam lithography. Scanning 1997; 19:466–8

149. Ocola LE and Stein A. Effect of cold development on improvement in electron-beam nanopatterning resolution and line roughness. Journal of Vacuum Science & Technology B: Microelectronics and Nanometer Structures Processing, Measurement, and Phenomena 2006 Nov; 24. Publisher: American Institute of Physics:3061–5

150. Fares N, Stanton S, Liddle J, and Gallatin G. Analytical-based solutions for SCALPEL wafer heating. Journal of Vacuum Science & Technology B: Microelectronics and Nanometer Structures Processing, Measurement, and Phenomena 2000; 18:3115–21

151. Yasuda M, Kawata H, Murata K, Hashimoto K, Hirai Y, and Nomura N. Resist heating effect in electron beam lithography. Journal of Vacuum Science & Technology B: Microelectronics and Nanometer Structures Processing, Measurement, and Phenomena 1994; 12:1362–6

152. Mkrtchyan M, Munro E, Liddle J, Stanton S, Waskiewicz W, Farrow R, and Katsap V. Global space charge effect in SCALPEL. Microelectronic engineering 2000; 53:299–302

153. Liddle JA, Gallatin GM, and Ocola LE. Resist requirements and limitations for nanoscale electron-beam patterning. MRS Online Proceedings Library (OPL) 2002; 739:H1–5

154. Rooks M, Kratschmer E, Viswanathan R, Katine J, Fontana Jr R, and MacDonald S. Low stress development of poly (methylmethacrylate) for high aspect ratio structures. Journal of Vacuum Science & Technology B: Microelectronics and Nanometer Structures Processing, Measurement, and Phenomena 2002; 20:2937–41

155. Hu W, Sarveswaran K, Lieberman M, and Bernstein GH. Sub-10 nm electron beam lithography using cold development of poly (methylmethacrylate). Journal of Vacuum Science & Technology B: Microelectronics and Nanometer Structures Processing, Measurement, and Phenomena 2004; 22:1711–6

156. Yasin S, Hasko D, and Ahmed H. Fabrication of¡ 5 nm width lines in poly (methylmethacrylate) resist using a water: isopropyl alcohol developer and ultrasonically-assisted development. Applied Physics Letters 2001; 78:2760–2

157. Stokes D. Principles and practice of variable pressure/environmental scanning electron microscopy (VP-ESEM). John Wiley & Sons, 2008

158. Ran J, Luo H, Yue Y, and Wang X. Measurement of the first Townsend's ionization coefficients in helium, air, and nitrogen at atmospheric pressure. Journal of the Physical Society of Japan 2014; 83:074503

159. Thiel BL. Master curves for gas amplification in low vacuum and environmental scanning electron microscopy. Ultramicroscopy 2004; 99:35–47

160. Sharma A and Sauli F. First Townsend coefficient measured in argon based mixtures at high fields. Nuclear Instruments and Methods in Physics Research Section A: Accelerators, Spectrometers, Detectors and Associated Equipment 1993; 334:420–4

161. Hawryluk R, Hawryluk AM, and Smith HI. Energy dissipation in a thin polymer film by electron beam scattering. Journal of Applied Physics 1974; 45:2551–66

162. Chang T. Proximity effect in electron-beam lithography. Journal of vacuum science and technology 1975; 12:1271–5

163. Wittels N and Youngman C. Proximity effect correction in electron-beam lithography. *JOURNAL OF THE ELECTROCHEMICAL SOCIETY*. Vol. 125. 3. ELECTROCHEMICAL SOC INC 10 SOUTH MAIN STREET, PENNINGTON, NJ 08534. 1978 :C158–C158

164. Parikh M. Corrections to proximity effects in electron beam lithography. I. Theory. Journal of Applied Physics 1979; 50:4371–7

165. Kruger J, Rissman P, and Chang M. Silicon transfer layer for multilayer resist systems. Journal of Vacuum Science and Technology 1981; 19:1320–4

166. Kratschmer E. Verification of a proximity effect correction program in electron-beam lithography. Journal of Vacuum Science and Technology 1981; 19:1264–8

167. Owen G and Rissman P. Proximity effect correction for electron beam lithography by equalization of background dose. Journal of Applied Physics 1983; 54:3573–81

168. Dix C, Flavin P, Hendy P, and Jones M. 0.1 μ scale lithography using a conventional electron beam system. Journal of Vacuum Science & Technology B: Microelectronics Processing and Phenomena 1985; 3:131–5

169. Otto O and Griffith A. Proximity correction on the AEBLE-150. Journal of Vacuum Science & Technology B: Microelectronics Processing and Phenomena 1988; 6:443–7

170. Vermeulen P, Jonckheere R, and Van Den Hove L. Proximity-effect correction in electron-beam lithography. Journal of Vacuum Science & Technology B: Microelectronics Processing and Phenomena 1989; 7:1556–60

171. Lee SY, Jacob JC, Chen CM, McMillan JA, and MacDonald NC. Proximity effect correction in electron-beam lithography: A hierarchical rule-based scheme—PYRAMID. Journal of Vacuum Science & Technology B: Microelectronics and Nanometer Structures Processing, Measurement, and Phenomena 1991; 9:3048–53

172. Jacob JC, Lee SY, McMillan JA, and MacDonald NC. Fast proximity effect correction: An extension of PYRAMID for circuit patterns of arbitrary size. Journal of Vacuum Science & Technology B: Microelectronics and Nanometer Structures Processing, Measurement, and Phenomena 1992; 10:3077–82

173. Rau R, McClellan JH, and Drabik TJ. Proximity effect correction for nanolithography. Journal of Vacuum Science & Technology B: Microelectronics and Nanometer Structures Processing, Measurement, and Phenomena 1996; 14:2445–55

174. Ren L and Chen B. Proximity effect in electron beam lithography. *Proceedings. 7th International Conference on Solid-State and Integrated Circuits Technology, 2004.* Vol. 1. IEEE. 2004 :579–82

175. Ocola LE, Gosztola DJ, Rosenmann D, and Lopez G. Automated geometry assisted proximity effect correction for electron beam direct write nanolithography. Journal of Vacuum Science & Technology B 2015; 33

Vita

Deepak Kumar

Place of birth:

- Jamshedpur, Jharkhand, India

Education:

- University of Kentucky, Lexington, Kentucky, USA
  PhD in Electrical Engineering, **in progress**, Advisor: Dr. J. Todd Hastings.
- University of Kentucky, Lexington, Kentucky, USA
  M.Sc. in Electrical Engineering, May 2020, Advisor: Dr. Vijay Singh.
- Birsa Institute of Technology, Sindri, India
  Bachelor of Technology in Electrical Engineering, May 2013.

Professional Positions:

- Graduate Research and Teaching Assistant, University of Kentucky Fall 2017 – Spring 2024

Conference Presentations:

NNCI Nano + Additive Manufacturing Summit	July 2023
Louisville, Kentucky	
66th Electron, Ion and Photon Beam Technology and Nanofabrication	June 2023
San Francisco, California	
NNCI Nano + Additive Manufacturing Summit	Aug 2022
Louisville, Kentucky	
65th Electron, Ion and Photon Beam Technology and Nanofabrication	May 2022
New Orleans, Louisiana	

Publications:

- Deepak Kumar, Krishnaroop Chaudhuri, Joseph W. Brill, Jonathan T. Pham, J. Todd Hastings; Effect of water vapor pressure on positive and negative tone electron-beam patterning of poly(methyl methacrylate). J. Vac. Sci. Technol. B 1 January 2023; 41 (1): 012604.